A Study of Leading Neutrons
in γp Collisions at HERA

by

M. Brkić

A Study of Leading Neutrons in γp Collisions at HERA

by

Miloš Brkić ✓

Abstract

High energy ($E > 400$ GeV) leading neutrons were observed for the first time in electron-proton (ep) collisions, in the data collected in 1993 with the ZEUS detector at the HERA collider. This was done using the test Forward Neutron Calorimeter (FNC). In this thesis, first, the ZEUS detector setup is described, including a detailed description of the FNC, its in-situ calibration and the determination of its acceptance.

At an ep collider photon-proton physics (photoproduction) can also be studied using the almost real photons emitted by the electron beam. With the FNC, leading neutron physics was studied using the ZEUS photoproduction data sample, at an average γp center of mass energy of 180 GeV. The first results are presented here, including the inclusive neutron spectrum. The characteristics of events containing such leading neutrons in photoproduction are discussed and compared to the overall photoproduction sample. The One Pion Exchange model from hadron-hadron collisions was found to be consistent with the presented data. The total photon-pion cross section was measured using the FNC to tag an almost real pion beam. It was found to be $\sigma_{\gamma\pi}$ (90 GeV) = 92 ± 5 (*stat.*) ± 28 (*syst.*) μb.

The inclusive transverse momentum (p_T) distributions of charged particles in photoproduction are also presented for non-diffractive events, the diffractive events in two bins of the diffracting mass, as well as for the non-diffractive leading neutron tagged events. The results are discussed and compared to the previous photoproduction and hadron-hadron data.

Graduate Department of Physics
University of Toronto

Contents

List of Figures

List of Tables

1 Introduction

In physics, the process of observing, recording, and measuring the simple phenomena plays an important role in bettering our description and understanding of the subject. It is no different in particle physics. The measurements of the interactions of the elementary particles have significantly aided the development of the best existing description of matter and its interactions — the "Standard Model".

A large amount of the present day experimental results in this field come from the detectors at particle colliders. This thesis describes the addition of a test device to the ZEUS detector at HERA in order to determine feasibility of studying leading neutron[1] production in electron-proton (ep) collisions. The first physics results and their implications are presented.

In Chapter 2 an overview of the theoretical background is given, with the intention of putting into context the results presented in the later chapters.

The HERA electron-proton collider, described in Chapter 3, provides the physicists with a unique look at collisions of two elementary particles at a very high center of mass energy of almost 300 GeV. Its design and operating parameters are presented.

The tools used for exploring the world of the smallest known particles have evolved from a person's naked eye to the present day international collaborations numbering hundreds of physicists, using thousands of tons of complex machinery and millions of electronic signals. The ZEUS detector is a good example of such a machine. Chapter 4 describes the ZEUS detector, focusing on the calorimetry and a few other components used later in the analysis.

Chapter 5 discusses the design, construction, calibration, and acceptance of the test Forward Neutron Calorimeter (FNC). The single cell iron-scintillator calorimeter and its in-situ calibration using the proton beam-gas collisions are described. The data selection criteria for the FNC sample from the ep physics runs at HERA are given in Chapter 6. The physics results presented in this chapter are restricted to the photoproduction events in which an almost real photon, emitted by the incoming electron, interacts with a proton from the beam. The results include some of the char-

acteristic distributions for this sample, such as the inclusive neutron spectrum, and their implications. Other physics from leading neutron tagged events is also presented, including the first measurement of the photon-pion total cross section $\sigma_{\gamma\pi}$ (at 90 GeV) and the observation of the double inclusive reaction $\gamma p \to pnX$.

Finally, in Chapter 7 the inclusive transverse momentum spectra in photoproduction are discussed and compared to previous experiments. A comparison is also made between the overall photoproduction sample and the subsample tagged with leading neutrons by the FNC.

---

1. a high energy neutron produced close to the proton beam direction

2   Electron-proton physics

According to the Standard Model [1], which is our best present description of the physics of elementary particles, there are four types of interactions: electromagnetic, weak, strong and gravitational. With each of these interactions a set of mediating particles "gauge bosons" is associated. The gauge bosons in the Standard Model are: the photon for electromagnetic interactions, W^+, W^-, and Z bosons for weak interactions, a set of eight gluons for strong interactions and the graviton for gravitational interactions. The interactions are described as proceeding through the exchange of these gauge bosons between the interacting particles. The exchanged particle is said to be "virtual" since it does not fulfill the energy-momentum relationship for "real" particles (i.e., $m^2 = E^2 - p^2$). Since the electromagnetic interactions are very well understood [2], and the energy scale at which the gravitational interactions become important is out of the present reach of particle accelerators, the experimental particle physicists at today's accelerators are predominantly occupied with understanding the weak and the strong interactions. In particular, testing the many aspects of Quantum Chromodynamics (QCD) [3], which describes the strong interactions, has been a focus of many recent studies. For example, measuring properties of "hard" (parton[1] level) interactions, which could be predicted from the theory using perturbative calculations, subjects the theory to experimental tests. This was made possible with the increasing energies available in the new accelerators and the corresponding rise in the characteristic scale of the interaction μ^2 (e.g., Q^2, p_T^2), away from the region where perturbative methods fail due to the increase in the strength of the strong coupling (i.e., α_s becomes large as $\mu^2 \to \Lambda^2_{QCD}$, where $\Lambda_{QCD} \leq 1$ GeV is the characteristic scale parameter for QCD).

According to the Standard Model there are two families of elementary, point-like, particles: quarks (q) and leptons (l). Leptons interact electromagnetically and weakly, and can exist as free particles. Quarks, on the other hand, can also interact strongly, and are thought to be confined by the strong colour field in hadrons (baryons and mesons). This difference leads to distinction between hadron-hadron, lepton-lepton, and lepton-hadron interactions. The first, although dominated by the strong force, is an interaction of two composite objects, which adds an extra degree of complexity to the studies; in the second (usually l^+l^- collisions) the quarks are pair produced, and mainly their decay and hadronization can be studied. The third, for example electron-proton (ep)

---

1. elementary, point like constituents of hadrons

interactions, provide a way of studying the structure of the hadrons, with a point-like probe. In this case the interaction mostly proceeds through the exchange of a virtual photon (γ) between the electron and a constituent of the proton. It is customary to subclassify these interactions into those involving a highly virtual photon ($E^2 - p^2 \ll 0$), referred to as Deep Inelastic Scattering (DIS, often defined by observation of the scattered electron at a substantial angle), and those involving an almost real photon ($E^2 - p^2 \approx 0$), termed photoproduction, due to the similarity to the γp interactions using a real photon beam.

2.1   Deep Inelastic Scattering (DIS)

DIS experiments have yielded a large fraction of our present knowledge about the substructure of nucleons, in particular the proton. It was in DIS experiments that the existence of partons was first inferred [4] by studying the angular dependence of the electron scattered from stationary protons. The virtuality of the exchanged photon (see Figure 2-1) defines the scale of the probing
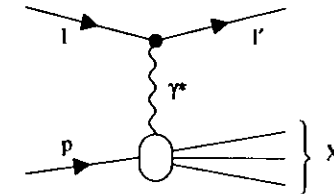
Figure 2-1 A general schematic of ep scattering
The electron-proton interactions proceed through the exchange of a virtual photon γ^*.

distance. Hence for highly virtual photons, the substructure of the nucleon becomes observable. The virtuality is quantified by the square of the magnitude of the exchanged photon's four vector q, which is the four momentum transferred between the lepton and the proton vertex. It is given by:

$$Q^2 = -q^2 = -(l - l')^2 \tag{2-1}$$

Other variables often used in describing the DIS kinematics are the Lorentz invariant scalars:

$$x = \frac{Q^2}{2(p \cdot q)} \text{ and } y = \frac{p \cdot q}{p \cdot l}. \tag{2-2}$$

In the simple parton model x is interpreted as the momentum fraction of the proton carried by the struck parton, and y is the fractional energy transferred from the electron to the proton in the proton's rest frame.

In inclusive DIS studies with longitudinally unpolarized[1] beams two independent variables are all that is needed to completely describe the process. The above three kinematic variables are related to the center of mass energy s through the following relation:

$$s = (l+p)^2 = \frac{Q^2}{xy}. \qquad (2\text{-}3)$$

There is a variety of physics topics that can be explored by studying DIS. Some of them are listed below, together with a reference to a related study done with the ZEUS experiment. For an overview of ep physics at HERA and for explanation of the concepts mentioned here see for example [5]:

- measurement of the structure function of the proton [6];

- low x QCD studies, yielding for example the gluonic content of the proton [7];

- high Q^2 diffraction leading to the structure of the pomeron [8];

- jet production and general characteristics of the hadronic final states (tests of perturbative QCD and hadronization) [9].

2.2   γp physics

Electron-proton collisions in which an almost real photon is exchanged are a very close approximation of real γp collisions, and can be used to obtain measurements on such interactions. The final state electron in these events is scattered through a very small angle, yielding, at ZEUS, $10^{-7} < Q^2 < 2\times10^{-2}$ GeV^2. If a sample of such events can be recognized and the scattered electron measured, then the energy of the photon is also known, and it can be used to study γp interactions with a varying but known photon energy.

The rest of this chapter discusses γp collisions, with emphasis on the aspects relevant to the results presented in Chapter 6 and Chapter 7. In this section the nature of the photon and its interactions with hadrons is reviewed, and its connection to hadron-hadron collisions is established. For a more detailed account of high energy photoproduction see [10]. An overview of the phenomenological description of the hadronic interactions at low momentum transfers is given in the next section.

2.2.1   γp interactions

The photon is the gauge boson for the electromagnetic interactions. As such, it couples only to particles that carry electromagnetic charge. At the elementary particle level this includes charged leptons (electron, muon and tau) as well as all the quarks (u, d, s, c, b and t), and the electro-weak charged boson W and their anti-particles. Photon interactions where the whole photon is absorbed

---

1. meaning that the helicity of the incoming particles is randomly oriented

5

by a charged particle are called direct interactions (see Figure 2-2 a-b). There is, however, another
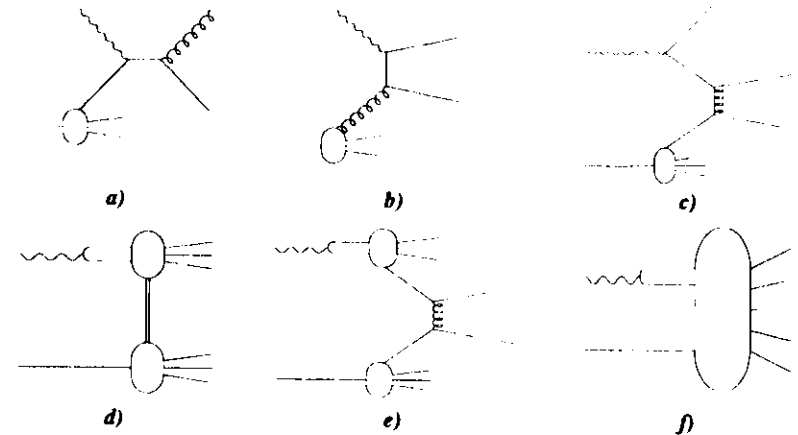
Figure 2-2 Diagrams for photon interactions
Diagrams a) and b) show the two types of direct processes (QCD Compton scattering (a) and photon-gluon fusion (b)). Diagram c) shows an example of the anomalous component, with one of the highly virtual quarks interacting with a quark from the proton through gluon exchange. The bottom row of diagrams shows examples of different VMD processes, where the photon fluctuates into a vector meson: diffractive scattering (d), hard scattering (e) and soft scattering (f).

way for the photon to interact, apart from such direct electromagnetic coupling to a parton within the target particle. A free photon can also couple to a virtual particle-antiparticle pair from the vacuum, thus effectively resolving itself into a parton pair. In this way a photon can also interact strongly (with the quarks and gluons from the proton in the case of γp collisions). It has been shown that such strong interactions of the photon dominate in high energy photon-hadron collisions, and that photon-hadron interactions bear remarkable similarity to other hadron-hadron collisions [11][12]. Equivalently, the direct coupling contribution has been shown to exist [13], but its contribution to the total γp interaction cross section is small.

Most often the photon fluctuates into a parton pair with small virtuality (characterized by low p_T between the partons). Such a fluctuation can exist for long enough time to further resolve into a cloud of virtual quarks and gluons thus yielding the structure of the photon, similar to that of hadrons with the same quantum numbers as itself. The family of hadrons with $J^{PC} = 1^{--}$, like the photon, are called the vector mesons, and include the ρ, φ, ω, J/ψ, Y mesons. The principle of Vector Meson Dominance [14] says that the photon-hadron interactions are fairly well described by considering the photon structure to be a superposition of the vector mesons. The interactions of this type have all the characteristics of hadron-hadron interactions, and can likewise be further subdivided into diffractive and non-diffractive. (Diagrams in Figure 2-2 d-f)

6

Diffractive collisions are those in which no quantum numbers are exchanged between the two interacting particles (in this case the photon and the proton). The simplest diffractive process is elastic scattering, in which the vector meson fluctuation of the photon is made real through the interaction with the proton, and the final state consists of the outgoing proton and vector meson (most of the time a ρ meson). A slightly more complicated case is when, through the interaction, the colliding particle changes to an excited state which then decays into a multiparticle final state. There are three possibilities:

1. **photon diffractive** — the proton stays intact, the vector meson breaks up into a multiparticle state with invariant mass M_x (referred to as the "diffractive mass");
2. **proton diffractive** — the vector meson stays intact, the proton breaks up;
3. **double diffractive** — both the proton and the vector meson break up.

The diffractive processes are described well by phenomenological models, based mainly on the optical analogy of hadron scattering. The hadrons are considered to be "black disks" and the scattering is described as diffraction of the particle wave from this "obstacle". This simple model does very well in a qualitative description of this type of scattering, but fails to yield good quantitative results. More discussion of the models that describe this type of event is presented in the next section.

The non-diffractive collisions can be classified into hard and soft. Hard collisions are those that can be interpreted as direct partonic collisions between the constituents of the two colliding particles. They are characterized by particles produced at higher transverse momentum and the formation of jets of particles (due to parton hadronization[1]) [15]. This class of event is calculable in perturbative QCD, using the parton density functions of the interacting particles. Another characteristic of these events is the presence of the remnant jets, formed around the beam pipe due to the hadronization of the remaining partons in the proton, and/or the photon after the collision.

Soft collisions are a class of collisions governed by the long-distance, confining behavior of the strong interaction. They are characterized by very low transverse momentum of the particles in the final state. The typical scale involved in soft collisions is too small to use perturbative QCD. Presently there is no calculable theory describing this type of interactions. The models describing them are mainly based on parametrization of the previous measurements.

A smaller fraction of the time the photon can fluctuate into a pair of highly virtual partons which normally recombine before they are able to resolve further. During such a fluctuation one of these partons can interact with a parton in the proton (see Figure 2-2 c). This is often referred to as the "anomalous photon" component. This type of interactions, involves partons and is character-

---

1. the process of forming colourless hadrons from the struck quarks and/or gluons — due to the confining nature of the strong interaction free quarks cannot exist.

ized by the large p_T scale of the virtual parton pair, and hence contributes to the hard scattering only. As such it is also calculable using perturbative QCD.

All these processes contribute to the total γp cross section. The energy dependence of the total cross section for γp interactions is similar to that of hadron-hadron interactions, except that it is much smaller ($\sigma_{\gamma p} \approx 4 \times 10^{-3} \sigma_{\pi p}$) since the photon has no valence quarks.

2.3   Hadron-hadron interactions

A lot of early work in hadron-hadron collisions has been concentrated on studying the general characteristics of the collisions, such as the behavior of the total cross section and particle production and distributions. In this section an overview of some of these non-perturbative studies and methods is given, and their relevance to the analysis presented in the later chapters is indicated [16][17][18].

Hadron-hadron collisions have been studied extensively with a variety of interacting particles. Meson-baryon, as well as baryon-baryon interactions studied include π and K meson beams on p and n targets, pp, p$\bar{\text{p}}$ and np collisions.

In general it was found that the behavior of the cross sections for these collisions is, at least qualitatively, well described by the simple optical model [18], where the target particle is considered as a potential obstacle for the incoming wave train of the beam particles. This model predicts the steep drop in the differential cross section as a function of the momentum transfer squared t for the elastic reaction, as well as the existence (but not the position of) the secondary maxima (diffraction "ripples"). The next model in complexity is the one particle exchange model, which assumes that two to two body interactions proceed through the exchange of a single particle. The exchanged particle, either a baryon or a meson, must satisfy all the required conservation laws (charge, strangeness, isospin, baryon number etc.). This model successfully predicts the relative sizes of the cross sections for different reactions depending on whether there exists an appropriate particle to be exchanged. Regge theory [19][20] builds on the ideas of these two simple models and is the basis for much of the phenomenological description of the data. It will be described in some detail in the next sections.

Another result coming from the numerous hadron-hadron studies is the principle of forward dominance, or the leading particle effect. Regardless of the incoming beams it is found that, especially in low multiplicity reactions, there tends to be a leading particle produced, carrying a large fraction of the momentum of the beam particle and moving at a small angle to the beam direction. The final state leading particle can (e.g., in the case of elastic scattering) be the same type as the incoming one, but it can also be different (e.g., pp → nX). The simple one particle exchange model can be used to predict whether there will be a peak in the differential cross section in the forward

or backward direction and the Regge model can predict some quantitative characteristics of these peaks.

2.3.1 Kinematics of two body scattering

The diagrams for the types of reactions that will be mentioned below in the context of Regge theory are shown in Figure 2-3. In this section some of the variables used in describing these
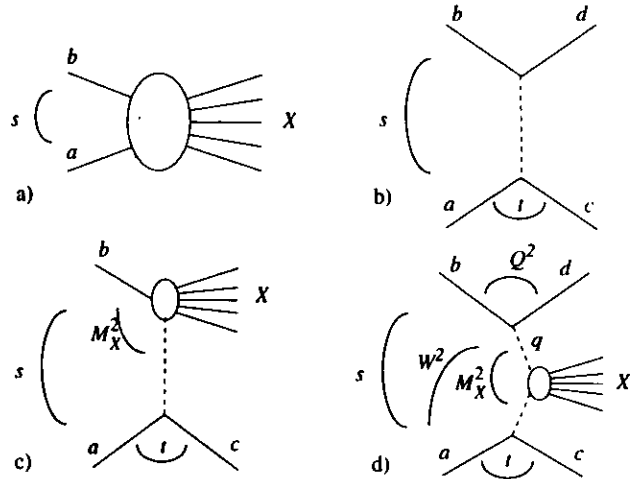
Figure 2-3 Diagrams for two body scattering
Given the center of mass energy squared s, inclusive scattering (a) is fully described with no free parameters. For two to two body scattering (b) two variables are needed to fully describe the process while one particle inclusive scattering (c) requires one more independent quantity for the extra degree of freedom gained by the unconstrained mass of the inclusive system. The number of variables grows to 6 in the case of two particle inclusive reactions (d).

interactions and their relations are given. The energy-momentum four vectors are denoted by the letter corresponding to the particle: $a = (E_a, \mathbf{p}_a)$. The bold faced symbols denote three vectors. The transverse momentum of a particle p_T, its rapidity y, and pseudorapidity η are often used in describing particle production. They are defined as follows:

$$p_T = \sqrt{p_x^2 + p_y^2},$$ (2-4)

$$y = \frac{1}{2}\ln\left(\frac{E + p_z}{E - p_z}\right), \text{ and } \cdot$$ (2-5)

$$\eta = -\ln\tan(\theta/2).$$ (2-6)

The rapidity is related to the longitudinal momentum of the particle. The pseudorapidity is a good approximation to rapidity for $p \gg m$ and away from $\theta = 0$ and is easily measurable since it depends only on the polar angle θ.

The number of independent variables n_v needed to fully describe a given process is given by counting the total number of variables and subtracting the number of constraints on them:

$$n_v = 3 \cdot n - 10,$$ (2-7)

where n is the number of particles involved in the reaction. When inclusive reactions are considered one extra quantity that is treated independently is the mass of the inclusive state X, since the constraint on p_X^2 is lifted.

For the inclusive reaction no free parameters are necessary. The reaction kinematics are determined by specifying the center of mass energy squared:

$$s = (a + b)^2 = m_a^2 + m_b^2 + 2a \cdot b \approx 4E_a E_b.$$ (2-8)

The last step assumes collinear colliding beams with energies much larger than the particle masses.

In the one particle inclusive reactions there are two independent variables, plus the mass of the inclusive system.

The variable often used is the square of the four momentum transfer t:

$$t = (a - c)^2 \approx m_a^2 + m_c^2 - E_a E_c\left(\theta^2 + \frac{m_a^2}{E_a} + \frac{m_c^2}{E_c}\right),$$ (2-9)

where θ is the scattered polar angle of particle c. The approximations made are that the mass is much smaller than the energy for both particles a and c and that the scattering angle $\theta \approx 0$. For two to two body scattering the same variable t is often used.

For case of two body inclusive scattering, as will be applied to forward neutron production in ep collisions later (see Section 2.5.1) another three variables must be added. One possible choice are the variables Q^2 and y defined in Section 2.1 and the fraction of the initial proton energy carried by the exchanged particle:

$$z = \frac{b \cdot (c - a)}{a \cdot b} \approx -\frac{E_a - E_c}{E_a}.$$ (2-10)

Another invariant variable useful in describing the photoproduction data is the center of mass energy of the γp system W. In the notation of Figure 2-3:

$$W^2 = s_{qa} = (b - d + a)^2 \approx ys.$$ (2-11)

The last approximation assumes Q^2, $M_a^2 \ll W^2$. Similarly, assuming t, $Q^2 \ll M_X^2$ Eqn. (2-10) can be written:

$$z \approx \frac{M_x^2}{W^2}.$$ (2-12)

2.3.2 Overview of the scattering theory and partial waves

The main general approach to the phenomenological studies of hadron-hadron interactions is to describe the particles with their quantum mechanical wave function and to treat the scattering problem in a way analogous to wave scattering from a given potential. If the potential is localized, or its strength falls off fast (so it can be considered localized), then far enough from the influence of the potential the wave function can be represented as the superposition of the incoming plane wave and an outgoing elastically scattered wave:

$$\Psi(x) = e^{ik \cdot x} + f(\theta, \phi)\frac{e^{ikr}}{r}.$$ (2-13)

Here $k = |k|$ is the momentum of the incoming particle, x is the space position and $r = |x|$ is the radial distance from the origin where the localized potential (in our case the target particle) is situated. The function $f(\theta, \phi)$ is called the scattering amplitude. It can be shown that the differential scattering cross section for elastic scattering depends directly on the scattering amplitude:

$$\frac{d\sigma}{d\Omega} = |f(\theta, \phi)|^2.$$ (2-14)

Usually the potential depends on r only and not on the angular variables in which case there is no ϕ dependence in the outgoing wave function and the scattering amplitude becomes $f(\theta)$. In this case the rotational symmetry can be exploited by expanding the scattering amplitude in terms of the angular momentum eigenfunctions, Legendre polynomials $P_l(\cos \theta)$:

$$f(k^2, \theta) = \sum_{l=0}^{\infty} (2l+1) a_l(k^2)P_l(\cos\theta) .$$ (2-15)

The functions $a_l(k^2)$ are called partial wave amplitudes.

Studying the analyticity of the amplitude it is found that the poles in the scattering amplitude on the real axis correspond to the bound states (or stable particles), while the complex poles close to the physical region lead to the resonances. Furthermore, the amplitude is often dominated by a single pole, leading to the one particle exchange picture. The amplitude is, however, not directly computable with these methods. Arbitrary functions must be introduced to eliminate certain divergences. This means that the predictive power of this theory is rather limited.

2.3.3 Regge poles and trajectories

What Regge has done is consider l as a complex parameter. By assuming that the scattering amplitude is an analytic function of l with only a countable number of singularities he obtained characteristics of the physical amplitude in the asymptotic limit of high center of mass energy. The poles in the partial wave amplitudes when l is considered as a complex parameter are called Regge poles, and the paths in the complex l plane that are traced by these Regge poles as k^2 changes are described by functions:

$$l = \alpha_n(k^2)$$ (2-16)

called the Regge trajectories. Here n is just an index to distinguish between the trajectories due to the different poles.

Often the real part of the trajectory is plotted as a function of s. Then the Regge trajectories are lines that connect the particles (bound states) and resonances with the same set of internal quantum numbers. Such states are situated at the integer values of $\mathrm{Re}\{l\}$. Trajectories are often named after the member with the lowest value of l. For example the rho trajectory contains ρ, A_2, g mesons while π, B, A_3 all lie on the pion trajectory. The exchange particles with the same internal quantum numbers that lie on a Regge trajectory are collectively named Reggeons. The Regge trajectories are all straight lines with a universal slope around 1 GeV^{-1}.

Instead of the interaction proceeding through the exchange of a single particle, in Regge theory it is considered as proceeding through the exchange of one or more Reggeons with the appropriate internal quantum numbers. Often, however, a single trajectory dominates the expression for the scattering amplitude, leading to the picture similar to the one particle exchange model, as will be seen in the case of one pion exchange model later.

There is one special case of a trajectory that was introduced phenomenologically to account for the approximate energy independence of the total cross section at high energies [22]. A trajectory was postulated with an intercept $\alpha(0) = 1$ which is necessary to explain the data. The same trajectory is used to explain the diffractive scattering in the case of which no quantum numbers are exchanged between the two vertices. This new trajectory was named the Pomeron trajectory. It is consistent with the prediction that Pomeranchuk made that in the high energy limit the total cross section for a particle and its antiparticle with the same target should be the same [23]. The Pomeron trajectory is different from the Reggeon trajectories in two aspects: its slope is ~0.25 GeV^{-1} and there are no known hadrons that lie on it. The nature of this phenomenological object that is exchanged in diffractive interactions (often termed the Pomeron) is still under scrutiny by both theorists and experimentalists. There are several models describing the Pomeron mostly as a collection of gluons forming a colourless state [24].

2.3.4 Regge theory

In Regge theory then, by considering l as a continuous complex parameter the sum over the integer values of l in equations such as Eqn. (2-15) is replaced by a Cauchy integral in the complex l plane, over a contour encircling the positive real axis. This contour can be deformed continuously to a sum of contours encircling all the existing Regge poles.

In the relativistic case the invariant amplitude used is a function of the invariant variables s and t and is given by:

$$A(s, t) = \sqrt{s} f(k^2, \theta). \qquad (2\text{-}17)$$

Using the Regge poles then yields in the asymptotic limit (i.e., as $s \to \infty$) an expression for the dependence of the amplitude, and hence the cross section, on s:

$$A(s, t) \equiv \sum_n \frac{1 + \xi_n e^{i\pi\alpha_n(t)}}{\sin\pi\alpha_n(t)} \gamma_n(t) \left(\frac{s}{s_0}\right)^{\alpha_n(t)}, \text{ as } s \to \infty. \qquad (2\text{-}18)$$

The signature of a trajectory ξ, is a simple sign factor either $+1$ or -1 due to the exchange symmetry in the relativistic case. It is needed to obtain satisfactory analytic continuation of the amplitude. The function $\gamma(t)$ contains the residue of the Regge pole, as well as the asymptotic behavior of the Legendre functions and some constant factors. Finally s_0 is an arbitrarily introduced scale parameter.

In the case of processes for which the exchange of one Regge trajectory dominates the expression for the amplitude (Eqn. (2-18)) the s dependence of the differential cross section at a given value of t in the high energy limit is given by:

$$\frac{d\sigma}{dt} \cong F(t) \left(\frac{s}{s_0}\right)^{2\alpha(t) - 2}, \qquad (2\text{-}19)$$

where $F(t)$ is a function absorbing all the constants and t dependent factors.

2.3.5 Optical theorem

An important result, often used in the phenomenological studies of hadron-hadron interactions is the optical theorem. It relates the total cross section σ_T for a two body scattering process (ab $\to$ X) to the forward elastic scattering amplitude $A^{el}(s, 0)$ for the process ab $\to$ ab:

$$\sigma_T = \frac{4\pi Im\{A^{el}(s, 0)\}}{s/2}, \qquad (2\text{-}20)$$

Figure 2-4 shows the diagrammatic representation of the optical theorem. When the amplitude for the total cross section is squared and summed over all the intermediate states, it is connected to the
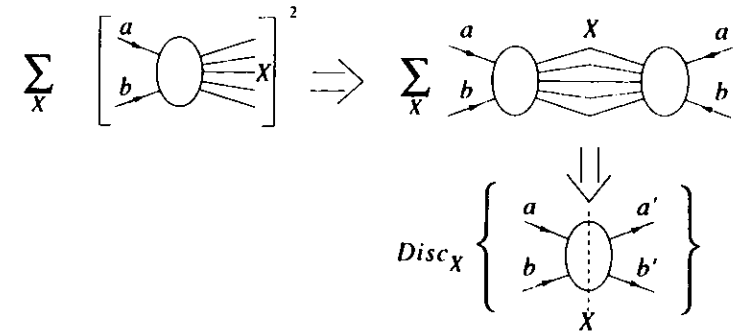
Figure 2-4 The optical theorem
The sum of the squares of the amplitudes for inclusive scattering over all the possible states X is related to the discontinuity of the elastic scattering amplitude.

discontinuity of the amplitude for the $2 \to 2$ elastic reaction by a unitarity relation. Since the amplitude is real analytic, the discontinuity of A across the real axis is equal to the imaginary part of A. For a derivation, see [20].

Together with the Regge theory approach for evaluating the amplitude, the optical theorem provides a way of predicting the high energy limiting behavior for the total cross section. This has lead to a successful description and parametrization of total hadron-hadron cross sections, as well as to the postulation of the existence of the Pomeron trajectory, as mentioned in Section 2.3.3.

2.3.6 Generalized optical theorem

In 1970 Mueller generalized this optical theorem to include one particle inclusive reactions [25]. Again, using unitarity relations, he related the total cross section for a one particle inclusive reaction to the discontinuity of the forward scattering amplitude for a three body elastic scattering process:

$$\frac{d^2\sigma}{dt dM^2} = \frac{1}{16\pi^2 s^2} Disc_X \{A(ab\bar{c})\}, \qquad (2\text{-}21)$$

where M^2 is the invariant mass of the final state excluding the observed particle, and $A(ab\bar{c})$ is the amplitude for the three body elastic scattering $a + b + \bar{c} \to a + b + \bar{c}$.

The generalized optical theorem is shown diagrammatically in Figure 2-5.

This new way of looking at the inclusive reactions has lead to a revival of the application of Regge theory to high energy physics data. Many reactions were successfully described (see [26] for an overview of the experimental results) using this extended Regge theory in different regions of phase space. The one relevant to the analysis presented in the later chapters is the Triple Regge
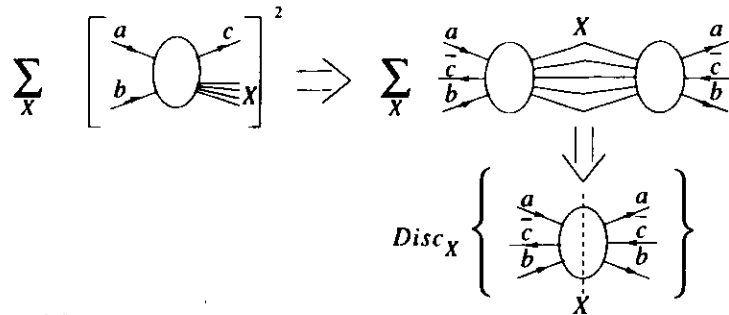
Figure 2-5 The generalized optical theorem
The sum of the squares of the amplitudes for one body inclusive process over all the intermediate states X is related to the discontinuity of the three body elastic scattering process.

limit where particle c is a fragment of particle a with small t. The diagram for the Triple Regge approximation is shown in Figure 2-6. Then as $s, M^2 \to \infty$, and if $s \gg M^2 \gg t$, the differential cross section can be written:

$$\frac{d^2\sigma}{dtdM^2} \to \frac{1}{16\pi^2 s^2} \sum_{i,j} \gamma^i_{ac}(t)\gamma^{j*}_{ac}(t)\xi_i(t)\xi^*_j(t)\left(\frac{s}{M^2}\right)^{\alpha_i(t)+\alpha_j(t)}$$

(2-22)

$$\times Disc_{M^2}\{A(ib \to jb; t, M^2, t_{bb'} = 0)\}$$

where M^2 is the invariant mass of the inclusive final state X, $\gamma(t)$ is the vertex function and $\xi(t)$ is the signature function.
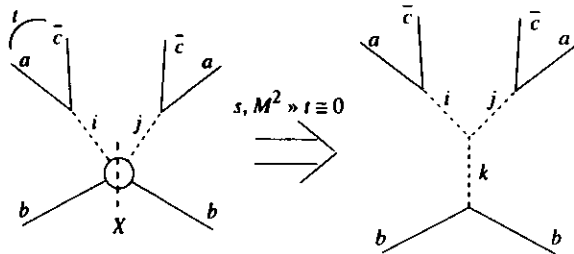
Figure 2-6 Triple Regge diagram
In the limit of high s and M^2, and small t the bottom vertex can also be treated in the Regge limit as proceeding through the exchange of a Regge trajectory.

In the case that the exchange of one Regge trajectory R dominates the sum over i and j only the term corresponding to both i and j being this dominant trajectory remains. Furthermore, the amplitude in the discontinuity function becomes the amplitude for the elastic process $Rb \to Rb$, which

is related by the regular optical theorem to the total cross section of the exchange particle R with particle b σ_T^{Rb}. Using Eqn. (2-11) and making these simplifications Eqn. (2-22) can be rewritten as:

$$\frac{d^2\sigma}{dtdz} = \frac{1}{8\pi}G^R(t)z^{1-2\alpha_R(t)}\sigma_T^{Rb} \equiv f_{R/a}(t, z)\sigma_T^{Rb},$$

(2-23)

where the function $G^R(t)$ is defined to contain all the t dependent terms from Eqn. (2-22).

Hence, in the Triple Regge limit, under the above assumptions, the differential cross section factorizes into a product of the flux factor $f_{R/a}(t, z)$ at one vertex and the total cross section at the other vertex. It is important to note that this result does not depend on what the other particle in the process (i.e., particle b) is.

2.4 One Pion Exchange (OPE)

In the case of one pion exchange on a proton target the flux factor of pions in the proton is given by [27]:

$$f_{\pi/p}(t, z) = \frac{1}{4\pi}\frac{G^2_{n\pi p}}{4\pi}\frac{t}{(m^2_\pi - t)^2}z^{1-2\alpha_\pi(t)}e^{b(t-m^2_\pi)}$$

(2-24)

where $G_{n\pi p}$ is the coupling at the $n\pi p$ vertex, $\alpha_\pi(t)$ is the pion Regge trajectory and the last exponential is a form factor accounting for both π and p being composite objects. From the data the factor b is determined to be consistent with being zero.

A class of events where this pion flux factor is relevant is a special class of peripheral collisions of the diagram in Figure 2-7, consisting of events in which a high energy leading baryon is
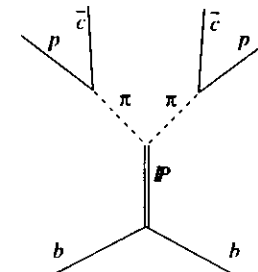
Figure 2-7 The triple Regge diagram for one pion exchange

produced. In such collisions the momentum transfer squared between the incoming and the outgoing baryon (particles a and $\bar{c}$ respectively in Figure 2-6) is small.

The idea that a single pion exchange mechanism is a dominant contribution to such peripheral nucleon-nucleon, as well as pion-nucleon scattering is quite old. For example, in 1958 Göbel suggested a method of determining the strength of $\pi\pi$ coupling by studying OPE in πN scattering [28], and in 1960 Bonsignori and Selleri reported estimates of $\sigma_{\pi p}$ and $\sigma_{\pi\pi}$ by considering reactions $pp \rightarrow pn\pi^+$ and $p\pi \rightarrow N\pi\pi$ and assuming OPE dominance [29]. Some other early studies utilizing OPE are listed in [30].

Later such peripheral processes have been extensively studied at FERMILAB and CERN, in hadron-hadron collisions at higher energies, mainly by detection of the leading baryon itself. A review of this data can be found in [31]. In the case of a proton target these studies have confirmed the OPE dominance in neutron and delta production. The validity of the factorization in Eqn. (2-23) is also confirmed in these experiments.

2.5   Leading neutrons in ep collisions

In the case of ep scattering the outgoing baryon can be one of many, including protons, neutrons, Δ's, and N^*'s. As shown in the diagram in Figure 2-8 such reactions are mediated either by
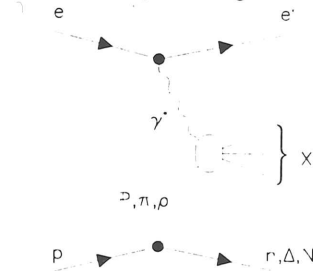
Figure 2-8 Peripheral processes in ep collisions

Pomeron exchange or by Reggeon exchange. In view of the Regge theory as well as the existing hadron-hadron data in case of the neutral exchange (e.g., elastic and diffractive proton scattering) the contribution from the Pomeron trajectory exchange dominates the cross section. In the case of charge exchange, however, the most important contribution is expected to be from a charged Regge trajectory. In the case of leading neutron production this would be the pion trajectory. This was confirmed in the hadron-hadron case by Engler et al. [32] by measuring the pion trajectory from the leading neutron data. Contribution from other charged Reggeon trajectories is expected to be small (~3% in case of the ρ trajectory [33]).

If the photon behaves similarly to a hadron, the production of direct leading neutrons in photoproduction should be well described by One Pion Exchange (OPE). Equivalently the process can be viewed as the photon interacting with a pion within the proton, leading to a decomposition of the cross section into a pion flux and gamma-pi cross section. In this case, leading neutron observation can be considered equivalent to tagging a virtual pion beam, and in ep collisions such events can be used to study high energy $e\pi$ interactions. Examples of quantities that can be measured this way are: $\sigma_{\gamma\pi}$, the total $\gamma\pi$ cross section, and in the higher Q^2 regime the pion structure function, if the measurement of the position of the neutron is also available.

In other words, if almost real pions are tagged by measuring leading neutrons, the ep machine can be used as an effective $e\pi$ collider with a pion beam of varying energy. Care must be taken to account for the background from diffractive leading neutron production, as well as non-direct neutrons resulting from decays of excited baryons. Furthermore at lower neutron energies there will be forward neutrons produced from non-peripheral ep collisions (termed centrally produced neutrons).

2.5.1   Measuring the $\gamma\pi$ total cross section

The $\gamma\pi$ cross section can be derived from the $ep \rightarrow enX$ cross section, where both the leading neutron and electron are detected. The assumption is made that the leading neutrons are produced predominantly through one pion exchange, so that detecting a leading neutron is equivalent to tagging an almost real pion, which collides with an almost real photon radiated by the electron, effectively producing $\gamma\pi$ collisions. It is further assumed that the cross section factorizes into a product of a flux factor and the cross section at both vertices:

$$\frac{d^4\sigma^{ep \rightarrow enX}}{dt\,dz\,dy\,dQ^2} = f_{\pi/p}(t,z) \cdot \frac{d^2\sigma^{e\pi \rightarrow eX}}{dy\,dQ^2}(y,Q^2) \quad \text{and} \tag{2-25}$$

$$\frac{d^2\sigma^{e\pi \rightarrow eX}}{dy\,dQ^2}(y,Q^2) = f_{\gamma/e}(y,Q^2) \cdot \sigma^{\gamma\pi \rightarrow X} \tag{2-26}$$

The photon flux is calculable from QED. Making the Equivalent Photon Approximation [34] (i.e., assuming that the very low Q^2 virtual photons behave like real photons, hence ignoring the longitudinal component of the cross section and assuming that the measurement is made at $Q^2 = 0$) the expression for the photon flux is:

$$f_{\gamma/e}(y,Q^2) = \frac{\alpha}{2\pi}\frac{1}{Q^2}\left(\frac{1+(1-y)^2}{y} - 2\frac{(1-y)}{y}\frac{Q_{min}^2}{Q^2}\right), \tag{2-27}$$

where Q_{min}^2 is given by:

$$Q_{min}^2 = -m_l^2 - m_{l'}^2 + 2\,(E_l E_{l'} - p_l p_{l'}) \tag{2-28}$$

and the indices l and l' refer to the incoming and the outgoing lepton (see Figure 2-1).

The gamma-pi cross section is obtained by measuring the cross section for ep → enX and dividing it by the integrated flux factors:

$$\sigma_{ep \to enX} = F_{\gamma/e} F_{\pi/p} \sigma_{\gamma\pi} \qquad (2\text{-}29)$$

where:

$$F_{\gamma/e} = \int\limits_{y, Q^2} dy dQ^2 f_{\gamma/e}(y, Q^2) \text{ and } F_{\pi/p} = \int\limits_{z, t} dz dt f_{\pi/p}(z, t). \qquad (2\text{-}30)$$

The integration is done over the range of the kinematic variables — Q^2, y, t, and z — observable in the experiment.

"There is nothing more worthy of study than nature."

Tesla

3   Hadron Electron Ring Anlage (HERA)

Traditionally, deep inelastic phenomena have been studied at fixed target experiments, with a lepton (electron, muon or neutrino) beam impinging on a stationary target (most often protons) [35]. The center of mass energy can be increased significantly by using colliding beams of electrons and protons, as in the well established single ring e^+e^- and $p\bar{p}$ colliders like LEP and TEVA-TRON. In the ep case, however, separate magnet rings and systems are necessary, mainly due to the large mass difference between electrons and protons. Two main factors resulting from this mass difference are:

- for electrons the energy loss by synchrotron radiation is larger by a factor of $(m_p/m_e)^4$ compared to that for protons, which implies that the electron beam needs much more power pumped into it to compensate these radiation losses; this limits the practical electron energy achievable;

- larger magnetic fields are needed to bend the higher energy protons than to bend the electrons around the same curve, leading to the use of superconducting magnets in the proton ring.

In the following sections the HERA machine and its basic characteristics are described.

3.1   The storage rings description

HERA is the first ever electron proton storage ring collider. It is located at the Deutsches Elektronen Synchrotron (DESY) laboratory in Hamburg, Germany. The tunnel in which the beamlines are located is 6.34 km long. In each of the four experimental areas the two beams are merged into a single beampipe, and brought to a head on collision. Older DESY machines (e.g., PETRA, DESYIII) have been rebuilt for use as the injection system for HERA. The layout of the HERA rings is shown in Figure 3-1, and a detail of the injection system in Figure 3-2.

At the four experimental halls the beams of 820 GeV protons and 30 GeV electrons collide yielding a center of mass energy of $\sqrt{s} = 314$ GeV. Both electron and proton beams are organized into 220 bunches equally distributed around the ring. This means that the consecutive bunches cross every 96 ns, equivalent to a crossing frequency of 10 MHz. Such a high rate imposes strict requirements on the triggering and data acquisition systems for the experiments, if they are to avoid a high percentage of dead time. A summary of the design and running parameters of the HERA storage rings is shown in Table 3-1.
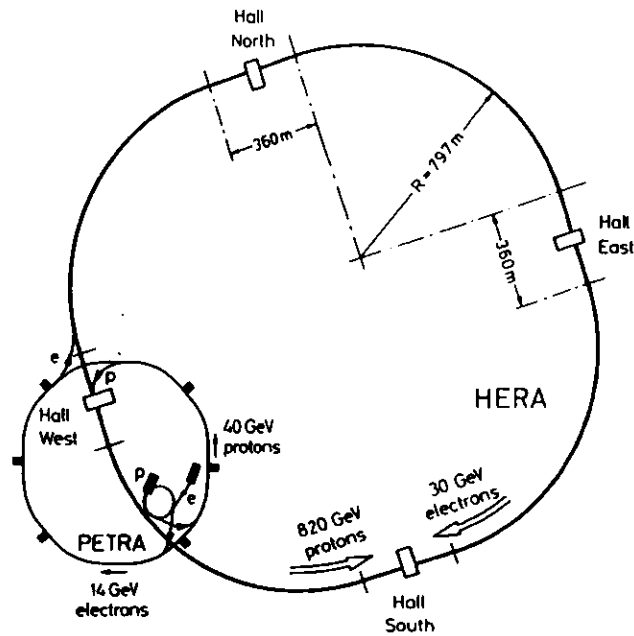
Figure 3-1 The layout of the HERA ring
The electrons and protons are brought into a single beampipe and interactions take place in the four straight sections of the ring. The ZEUS and H1 experiments are in the south and the north halls respectively.

3.2 Performance to date

The first ep collisions were observed at HERA in May 1992. For the first two years of operation the electron machine was run at 26.6 GeV rather than the design energy of 30 GeV. The bunch structure was also not as specified by design; during the '93 running period there were 86 ep bunch crossings, with 6 proton and 10 electron pilot bunches. The pilot bunch crossings have only one of the two beams occupied, so that proton-gas and electron-gas events can be collected for background studies and subtraction.

One of the important characteristics of any storage ring collider is the instantaneous luminosity, $\mathcal{L}$. It represents the number of expected events per unit of cross section per unit of time (i.e., the rate for a process with cross section σ is $R = \mathcal{L}\sigma$). It is determined by the numbers of particles circling in the rings, the frequency of beam crossings, and the common transverse size of the beams (i.e., $\mathcal{L} = n_1 n_2 f / A$). In 1993 at HERA the highest average luminosity in a single run was 1.5×10^{30} cm^{-2}s^{-1}, which is one order of magnitude less then the design value. The total integrated
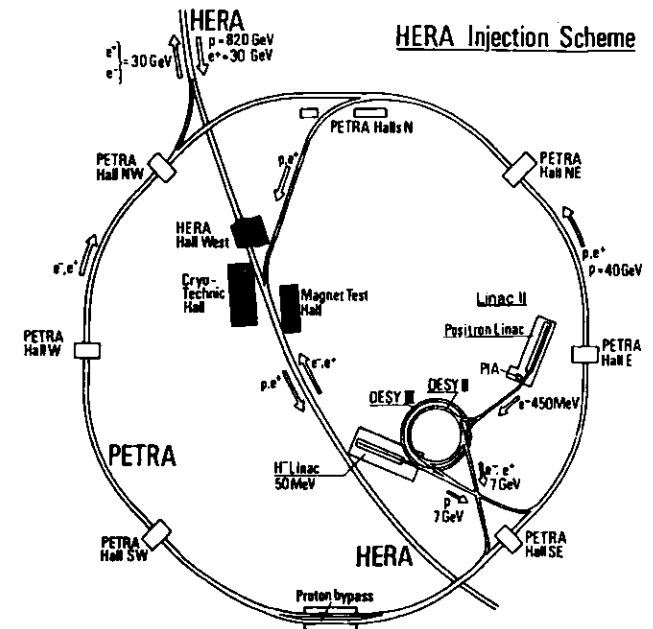
Figure 3-2 The HERA injection system

HERA parameter	Proton Beam		Electron Beam	
	Design	1993 run	Design	1993 run
Tunnel circumference (m)	6336			
Crossing angle (mrad)	0			
Time between crossings (ns)	96			
Luminosity (cm^{-2}s^{-1})	1.5×10^{30} (max)		1.5×10^{31}	
Injection energy (GeV)	40		14	
Beam energy (GeV)	820	820	30	26.7
Number of bunches	210	92	210	96
Typical total current (mA)	160	11	58	8
Current per bunch (mA)	0.78	0.12	0.28	0.08
Beam size x (mm)	0.27		0.26	
Beam size y (mm)	0.08		0.07	
Beam size z (mm)	110		8	

Table 3-1 Design and running parameters of the HERA ep collider

luminosity (instantaneous luminosity integrated over time) delivered by the HERA machine reached 1 pb^{-1}, during the '93 running period. Of this the ZEUS detector was active, and collecting data for ~600 nb^{-1}, yielding a collection efficiency of just under 60%.

3.3 Experiments at HERA

Presently there are two large multi purpose detectors installed and running at two of the interaction points at HERA — the H1 detector situated in the North Hall, and the ZEUS detector in the South Hall. In contrast to other collider detectors (e.g., LEP and TEVATRON experiments) both of these detectors are asymmetric with respect to the interaction point. This, of course, reflects the fact that the HERA beams have different energies, resulting in the center of mass frame of the colliding particles being strongly boosted in the forward (proton) direction, hence requiring detection of higher energy particles in this region.

"Thinking is more interesting than knowing, but less interesting than looking."

Goethe

4 The ZEUS detector

ZEUS is one of the two large, multi purpose detectors installed at HERA. The ZEUS collaboration consists of around 450 physicists, from 49 institutes and 12 countries. Even some of the subcomponents (e.g., the calorimeter) are a joint effort of large multinational groups. The detector and the data acquisition system (DAQ), as well as the trigger, are described here in some detail, with emphasis on the components used in the analysis presented in the later chapters. The full description of all the components can be found in [36].

4.1 Overall description

The basic design of ZEUS parallels that of many typical collider detectors. As seen in the longitudinal cut view of the experiment in Figure 4-1, the Interaction Point (IP) is surrounded by the Inner Tracking Detectors, most of which sit in the 1.4 T strong axial magnetic field, provided by the thin superconducting solenoid magnet with radius 0.95 m. The hermetic uranium Calorimeter (CAL) envelopes the coil and the inner detectors. Surrounding CAL is the iron yoke, which is instrumented with limited streamer tubes as the Backing Calorimeter (BAC). The iron yoke is magnetized with conducting coils providing a toroidal field for muon momentum measurement. Muons are measured in the Forward, Barrel and Rear Muon Chambers (F/B/RMU), a set of drift chambers (only FMU) and limited streamer tubes, installed on either side of the iron yoke, thus enabling momentum measurement for the particles penetrating the main detector.

There are also several components used for detection of leading particles leaving the IP at small angles. The Leading Proton Spectrometer (LPS) is a set of six silicon diode detector stations very close to the proton beam (10 σ from the beam center) located between 24 and 90 m and used for tagging the leading proton in elastic and diffractive events. The Luminosity Detector (LUMI) and the test Forward Neutron Calorimeter (FNC) will be described in more detail in the next sections. Finally, the Prototype Beam Pipe Calorimeter (BPC), a small tungsten silicon calorimeter located next to the beampipe behind the Rear Calorimeter in the downstream electron direction, extends the Q^2 region in which the scattered electron is detectable (~0.2-0.7 GeV^2).

Other components, mainly for background detection and rates monitoring include: the C5 counter, a set of scintillation counters also used for beam timing studies, surrounding the beampipe

Overview of the ZEUS Detector
(longitudinal cut)
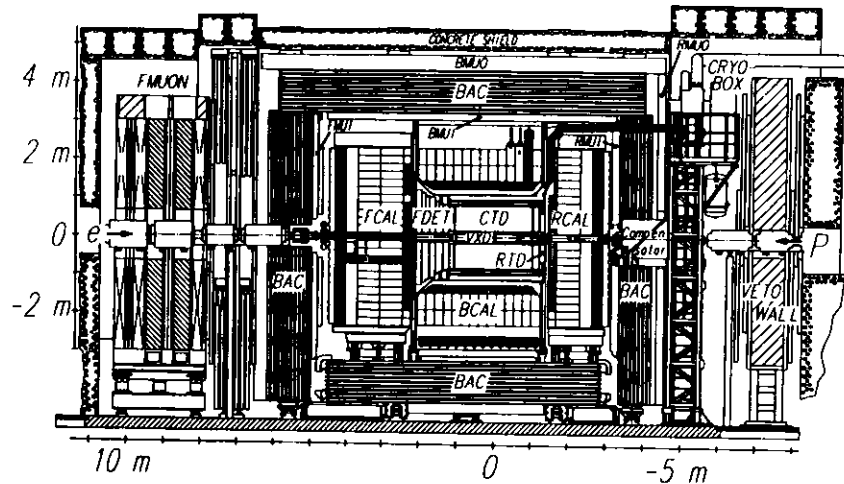
Figure 4-1 The longitudinal Cross Section of the ZEUS detector

The along-the-beam-line (z) cross section of the ZEUS detector. The components shown are: the inner tracking detectors (FDET, CTD, VXD and RTD), the high resolution depleted uranium calorimeter (F/B/RCAL), the backing calorimeter (BAC), the muon chambers (F/B/RMUI and F/B/RMUO) and the veto wall. The superconducting solenoid coil is located between the CTD and BCAL (for details see Figure 4-2). Its cryogenic system is seen behind RCAL. Components not shown/labeled include the far away components (LUMI, LPS, and FNC) as well as the C5 counter and the prototype beampipe calorimeter located immediately behind RCAL.

Note the definition of the ZEUS coordinate system: +z in the proton direction, +y upwards, and hence +x towards the middle of the storage rings.

in the vicinity of the BPC, and the Veto Wall located upstream in the proton direction, used to detect and veto halo particles coming with the proton beam, as well as beam-gas interactions from well upstream.

4.2 Main detector components used in the analysis

This section describes in more detail the components of the ZEUS detector relevant for the analysis presented in the later chapters, as well as the trigger used in the '93 running period. In particular, the ZEUS high precision calorimeter is described in more detail, beginning with a brief overview of calorimetry in general. This overview is also relevant for the later description of the FNC prototype, which is also a calorimetric device. Next, the LUMI detector is described, followed by an overview of the Central Tracking Detector and finally the Data Acquisition (DAQ) system and the ZEUS trigger system.

4.2.1 General calorimetry

Calorimeters are devices used to measure the energy of particles, by recording the amount of energy deposited in the active part of the detector. The fraction and shape of the active part can vary. For homogeneous calorimeters (e.g., lead glass calorimeters) the entire detector is simultaneously absorber and active material. For sampling calorimeters, on the other hand, energy is collected ("visible") from only part of the detector volume, and this measurement is then related to the incident energy of the particle, through a constant referred to as the sampling fraction. It is defined as the ratio of the energy deposited in the active part of the calorimeter to the total energy deposited in the calorimeter:

$$f_s = \frac{E_{vis}}{E_{tot}}.$$ (4-1)

The fact that not all the deposited energy is directly observed leads to an important source of uncertainty in the energy measurement called sampling fluctuations. These are one of the largest contributors to the resolution of sampling calorimeters. This is discussed in more detail in Section 4.2.1.3.

Both CAL and FNC are sampling calorimeters, and moreover, they are both sandwich calorimeters consisting of multiple layers of dense material as absorber and scintillation tiles as active material. Hence in the rest of this section only such devices will be considered.

What happens to a particle upon entry into a dense medium depends greatly on the type of particle. Based on this calorimeters can be divided into electromagnetic (intended for detection of mainly electromagnetically interacting particles, such as electrons and photons), and hadronic (for detection of strongly interacting particles — hadrons). Detailed discussions of calorimetry can be found in the reviews such as [37][38][39]. In the rest of this section a summary of the important processes and quantities in calorimetry is presented.

4.2.1.1 Electromagnetic calorimeters

Electrons, positrons and photons lose energy predominantly by particle production (photon radiation for the first two, and pair production for the last) down to energies small compared to the incident energies at HERA, of the order of 10-100 MeV. Once a particle reaches this critical energy the rest of its energy is dissipated through scattering and ionization. This type of behaviour leads to development of electromagnetic showers whose dimensions can be approximated by the depth and radius in which a certain fraction of the deposited energy is found. Material dependence of the containment depth can be included in a parameter called the radiation length (X_0). It is defined as

the distance after which, on average, the energy of an incident electron falls to 1/e of its incoming energy. It is approximately given by

$$X_0 \approx 180A/Z^2 \ (\text{cm/g}^2), \tag{4-2}$$

where A and Z are the atomic mass and the atomic number respectively. Longitudinal containment of electromagnetic showers is found to be independent of material if distance is measured in X_0, and to scale logarithmically with energy. Up to the highest electron energies expected at HERA (order of 100 GeV) 98% of the electron's energy is contained in 25 radiation lengths, which coincides with the depth of the EMC sections of the CAL (see Section 4.2.2). Laterally electromagnetic showers are contained at the 95% level within a cylinder of radius $2\rho_m$ where:

$$\rho_m \approx 7A/Z \ (\text{g/cm}^2) \tag{4-3}$$

is the Molière radius. In the CAL this is ~ 2 cm. This is small compared to the horizontal segmentation of the RCAL (20 cm) allowing position determination in that direction from the difference in the signals at the two sides. The vertical size (10 cm) was picked so that there is enough signal in the neighboring cells, allowing vertical position determination from signal division between all the cells surrounding a large energy deposit.

4.2.1.2 Hadronic calorimeters

For strongly interacting particles (i.e., hadrons) the significant energy loss mechanisms are more varied. Due to their high masses, compared to that of the electron, their electromagnetic particle producing interaction cross sections are highly suppressed. Even for the lightest hadrons, pions, the suppression factor is $(m_\pi/m_e)^2 = 78400$. Hence the strong interaction processes play a determining role in high energy hadronic shower development. Upon entering a dense medium a high energy hadron loses energy by ionization (dE/dx), until it interacts with an atomic nucleus. Such a collision often results in an intranuclear cascade, yielding a variety of secondary particles (spallation), including more charged and neutral hadrons, photons, electrons, muons, as well as neutrinos. The remaining nucleus can be highly excited, and its deexcitation can produce even more secondary particles (evaporation). All these particles further interact and can contribute differently to the energy observed in the active material of the calorimeter.

The secondary hadrons themselves can interact and deposit energy in different ways. The produced π^0's and η's decay into photons and hence contribute to the electromagnetic part of the shower. For low energy charged hadrons (e.g., p, $\pi^\pm$) dE/dx losses by ionization dominate, while neutrons lose their energy through elastic scattering with nuclei (resulting in more ionization energy deposition from the moving charged ions), as well as further nuclear interactions, similar to the primary one. Neutron capture, and in the case of uranium absorber, fission are also ways of energy transfer in hadronic showers.

The photons and electrons produced initiate electromagnetic showers within the hadronic cascade. At not too high an energy the muons deposit energy only by ionization and are almost perfect "minimum ionizing particles" (mip). They penetrate the calorimeter and leave it, while depositing only a small fraction of their energy. Other ways of energy escaping detection are through the production of neutrinos, which can also penetrate large thickness of material without interacting (since they only interact weakly), and the loss to nuclear binding energy in the process of freeing nucleons from the nuclear potential.

Since the nuclear interactions are mainly responsible for the formation of the hadronic showers the distance scales related to these nuclear interactions govern the typical sizes of hadronic showers. The longitudinal containment is found experimentally to scale with the nuclear interaction length λ_{int}, and to depend logarithmically on the incident energy. At the highest HERA energies (~ 800 GeV) a hadronic shower is contained at the 95% level in 8 λ_{int}, while at 400 GeV the corresponding containment depth is 7 λ_{int}. These dimensions are closely related to the sizes of the FNC and FCAL respectively. The lateral profile of hadronic showers is characterized by a double exponential shape, with a thin core (typically 0.1-0.5 λ_{int} in diameter) containing most of the energy, accompanied by a wider tail carrying a small fraction of the energy, such that typically 95% of the energy in the hadronic shower is deposited within a cylinder of radius 1 λ_{int}.

4.2.1.3 Resolution considerations

The energy resolution of calorimeters depends on many factors, but can generally be written as a sum of two terms:

$$\frac{\sigma}{E} = \frac{\sigma_{stat}}{E} \oplus \frac{\sigma_{other}}{E} = \frac{a}{\sqrt{E}} \oplus b, \tag{4-4}$$

where a and b are constants depending on the materials, sampling fractions, thicknesses of active and passive layers etc. The first term is due to the statistical nature of the measurement process. The second term, called the "constant term", comes from other contributions such as degree of energy leakage from a finite size calorimeter, compensation (discussed below), calibration accuracy and noise in the readout process.

The statistical term can be further subdivided into more specific contributions:

$$\sigma_{stat} = \sigma_{int} \oplus \sigma_{sam} \oplus \sigma_{etc}, \tag{4-5}$$

each of which depends on the counting of some statistically fluctuating quantity which is proportional to the energy. The first term is the intrinsic resolution, coming from fluctuations in the shower formation process. In the electromagnetic calorimeters it is equivalent to measuring the total

"track" length of minimum ionizing particles L_{mip}, which is proportional to the energy of the incoming particle. The resolution term due to this is then:

$$\frac{\sigma_{int}}{E} \propto \frac{1}{\sqrt{L_{mip}}} \propto \frac{1}{\sqrt{E}}.$$ (4-6)

In hadronic calorimeters the intrinsic resolution has additional complexity stemming from the various processes contributing to the energy deposition and is in general larger than an equivalent electromagnetic resolution.

The second term in Eqn. (4-5) is specific to sampling calorimeters and is due to sampling fluctuations. Since only part of the energy deposited in the calorimeter is actually observed the size of the observed energy fluctuates statistically from shower to shower yielding a resolution term proportional to the square root of the number of ionizing particle crossings of the active medium, which is again proportional to the incoming energy, but also depends strongly on the sampling fraction and the material composition of the device.

The third term is present to account for any other processes contributing to the resolution in a statistical manner (e.g., photoelectron production in the case of photomultiplier readout).

In a hadronic shower a great variety of particles can be produced, depending on the exact processes contributing to its development. Since the measured energy depends on the type of particles involved, the measured energy varies from shower to shower making the resolution of hadronic calorimeters in general worse than that of electromagnetic calorimeters. For example, the fraction of undetected energy due to escaped particles and breaking nuclear bonds can vary considerably from shower to shower. Another greatly fluctuating component is the fraction of energy deposited by electromagnetic shower formation (as described in Section 4.2.1.1). This component of the hadronic shower consists of prompt gammas released in the nuclear interactions, decays and deexcitations, as well as from the gammas produced in the decays of mainly π^0 's (and η's). If the average response to the purely hadronic part of the shower is not the same as the response to electrons and photons, clearly the measured energy will depend on the proportion of the total energy carried by the electromagnetic part of the shower.

This latter aspect of hadron calorimetry is characterized by the ratio of the response to electromagnetic particles to the response to hadronic particles (e/h). Optimal energy resolution is obtained when $e/h = 1$. Traditionally this problem was viewed as a need to compensate the energy lost in the strong interactions, hence the name compensating calorimeter is used for a device with equal response to hadrons and electrons. There are several processes that can be used to achieve compensation:

- in radioactive absorbers, such as uranium, some of the lost energy is regained from the fission process, through the emitted photons and neutrons;

- since a large fraction of the visible energy in the electromagnetic showers is deposited by the low energy, short range photons and electrons, the thickness and type of the absorber and active media influence greatly the response to these particles. By choosing high Z absorbers and low Z active material (e.g., scintillator, which is mostly hydrogen) as well as choosing a larger absorber thickness, so that the short range particles in the tail of the shower never reach the active layers, the electromagnetic component of hadronic showers can be suppressed, in comparison to the hadronic part governed by a much larger distance scale;

- a large fraction of the hadronic part of the shower consists of low energy neutrons which leave their energy primarily by elastic scattering off the atomic nuclei, which then deposit it by ionization. This process depends greatly on the cross section for neutron-nucleus scattering, and the efficiency of energy transfer in such collisions. The neutrons lose their energy more readily to the lighter nuclei, so that in case of a hydrogen based active material (e.g., scintillator) the neutrons preferentially yield visible signal, while the low energy charged particles lose their energy more equally in the absorber and active material layers. Hence by changing the relative thicknesses of these layers the relative contribution of the neutrons to the visible energy can be controlled.

Combination of these effects is a powerful tool in controlling the e/h ratio of hadronic calorimeters. It has been shown by several experiments as well as by Monte Carlo simulations [40] that many different sandwich calorimeter combinations can be made compensating by choosing the appropriate thicknesses of the absorbing and active materials. Both the structures chosen for the ZEUS main calorimeter and the FNC have the e/h ratio close to 1.0.

4.2.1.4 Albedo

Another interesting characteristic of high energy particle showers in calorimeters is the presence of backscattered particles, the so called albedo. When a high energy hadron enters a dense medium, such as the absorber of a calorimeter, even though most of the secondary particles continue in the direction close to the incoming direction, some of the lower energy ones are backscattered and exit back through the face of the calorimeter. A detailed study was done in a cosmic ray experiment [41], with an iron scintillator calorimeter, with hadrons in the energy range between ~100-2000 GeV.

This component of the shower, although very small and therefore not important for the calorimetric energy measurement, becomes very important when scintillation counters are to be used

to determine whether the incoming hadron was a charged or a neutral particle. This application will be discussed in more detail in the context of the FNC in Section 5.4.

There are many components to the albedo flux. Many of the backscattered particles have low energy. The low energy neutrons from nuclear interactions are more likely to escape the bulk of the calorimeter and deposit energy in the scintillation counters positioned immediately in front of it. They deposit the energy mainly through collisions with the light hydrogen nuclei which then lose the gained energy through ionization. Even though these low energy ions are more highly ionizing, they can still deposit energy equivalent to a fraction of a mip if their energy is low enough and they do not traverse the full width of the counter. Another characteristic of these low energy backscattered particles is that they are slow, hence causing a delay in the time measurement of the signal.

4.2.2 The ZEUS calorimeter

The ZEUS main calorimeter is a central part of the ZEUS detector. It is a sandwich calorimeter made of depleted uranium and scintillator layers, segmented into an electromagnetic section followed by one or two hadronic sections. It has a total of 11834 readout channels, corresponding to 5917 cells read out on both sides. The energy resolution for electromagnetic showers is:

$$\frac{\sigma_E}{E} = \frac{18\%}{\sqrt{E}}, \qquad (4\text{-}7)$$

and for hadronic showers it is:

$$\frac{\sigma_E}{E} = \frac{35\%}{\sqrt{E}}. \qquad (4\text{-}8)$$

Since the calorimeter is hermetic and compensating the constant term depends mainly on calibration, and with the uranium radioactivity providing a constant monitoring signal for calibration the constant term is kept to a fraction of a percent for the electromagnetic, and under two percent for the hadronic resolution.

This section describes the calorimeter, including its physical characteristics, electronic readout, and calibration techniques.

4.2.2.1 Detector description

The ZEUS calorimeter was designed to be both hermetic and compensating. It completely surrounds the interaction point, except for the two 20x20 cm^2 holes for the beam pipe. This results in 99.6% solid angle coverage. Mechanically it consists of three subcomponents: forward, rear, and

barrel calorimeters (F/R/BCAL respectively). Figure 4-2 shows their spatial coverage and layout. FCAL and RCAL each consist of 23 modules of varying length, with the middle one, surrounding the beam pipe, being split into top and bottom halves. The module width of 20 cm defines the segmentation in the horizontal direction (i.e., in x in ZEUS coordinates). Longitudinally (i.e., in z) the modules are divided into a 25 X_0 (~ 1 λ_{int}) section acting as an electromagnetic calorimeter (EMC), followed by hadronic sections of ~3 λ_{int} each (HAC). FCAL and BCAL have two HAC sections, making them 7.1 λ_{int} and 5.3 λ_{int} deep respectively. Due to the strongly forward boosted nature of the HERA collider, in the rear direction 4 λ_{int} is sufficient for 95% containment; therefore there is only one HAC section in the RCAL. HAC sections are read out in 20 cm strips in the vertical direction (i.e., in y), while EMC sections are segmented more finely — 5 cm in FCAL and 10 cm in RCAL — except for the areas shaded by BCAL, which are considered as hadronic sections and have 20 cm high readout.

BCAL has 32 wedge shaped modules arranged in a cylinder with inner radius 1.2 m, and axis along the beam direction (z axis). They are skewed by 2.5° in ϕ, so as to make the readout between adjacent modules non-projective. Granularity is similar to FCAL: module width in ϕ, 20 cm along z in HAC, and 5 cm along z in EMC sections. Moreover, EMC cells are projective in θ, that is they point towards the nominal interaction point (See Figure 4-2).

The physical parameters of the ZEUS calorimeter are summarized in Table 4-1.

One of the FCAL 20x20 cm^2 towers can be taken as a representative of the substructure of the entire calorimeter, since the rest of the towers are of the same construction. Figure 4-3 shows a partial cross section of one of the FCAL modules. Each section consists of 3.3 mm thick depleted uranium (DU) plates as the absorbing material, and 2.6 mm thick scintillator tiles as the active material. The DU plates are clad in stainless steel to contain the radioactive uranium. The thickness of the cladding was selected to limit the noise signal from the natural radioactivity to a level where it can still be used for calibration, while not introducing a significant noise compared to the expected real signals. It is 0.2 mm thick in the EMC and 0.4 mm thick in the HAC sections. The difference is due to the different cell sizes in each. The quality control on the thickness of the plates was very strict (about 5% tolerance), ensuring uniform sampling of the showers in the calorimeter.

The scintillator used was SCSN-38, cut into appropriate size tiles. Each tile was wrapped in white, Tyvek paper highly reflective in the UV range of the spectrum. This enhanced the light yield, by reflecting some of the light which has escaped the scintillator back into it. A black pattern was printed on the paper to make the light yield more uniform, by correcting for the geometric effect of enhancement of the signal due to the energy deposits close to the edge of the scintillator tile. The light produced in the scintillator was collected along the edges at the sides of the modules, by Wave Length Shifter (WLS) bars. These were made out of PMMA plastic doped with a dye called Y7. As shown in Figure 4-4, the absorption spectrum of this material overlaps well with the emis-

DIMENSIONS:
6m x 6m

HAC 2 HAC 1
EMC
SOLENOID
CENTRAL TRACKING
REAR TRACKING

e⁻

p

FCAL (7λ)
HAC 1,2 : 3.1λ
DEPTH: 1.52 m

BCAL(5λ)
HAC 1,2 : 2.1λ
DEPTH: 1.08 m

RCAL(4λ)
HAC: 3.1λ
DEPTH: 0.9 m
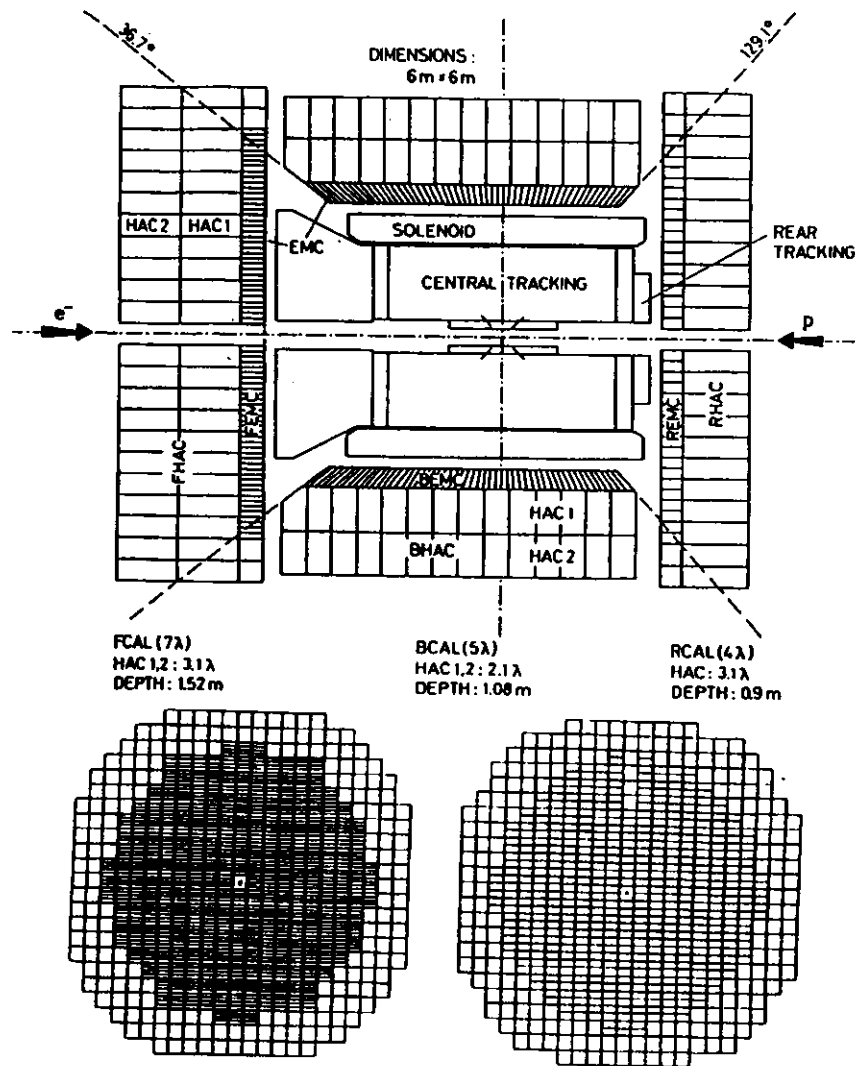
Figure 4-2 The segmentation and dimensions of the ZEUS calorimeter
The top diagram shows the relative positions and coverage of the three CAL parts. It also shows the segmentation of each of the calorimeters into towers, as well as into longitudinal EMC and HAC sections. The bottom diagrams show the segmentation of the FCAL and RCAL into EMC cells. Note the finer segmentation of FCAL, as well as the coarser segmentation (equivalent to HAC) around the edges of F/RCAL, which lie in the shadow of BCAL.
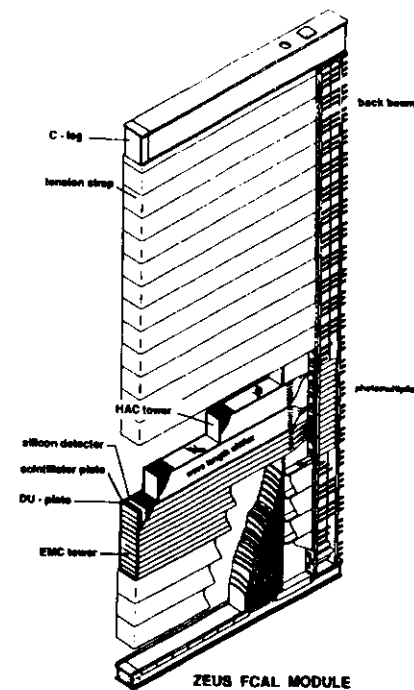
ZEUS FCAL MODULE

Figure 4-3 Schematic diagram of an FCAL module
This partial cross section shows the inner composition of an FCAL module, which is typical for all of the ZEUS calorimeter. Steel clad depleted uranium plates and layers of scintillator tiles alternate within the mechanical support frame (C-legs and back beam) and are held together with stainless steel tension straps. The wave length shifter bars, located between the layered structure and the straps, transmit the signal light to the photomultiplier tubes mounted on the back beam.

sion spectrum of SCSN-38, while its own emission spectrum matches well the response spectrum of the photo multiplier tubes (PMTs) used. To correct for the effects of the attenuation in the WLS the backreflectors had a black pattern printed on them, absorbing the appropriate fraction of the light coming from the scintillator tiles closer to the PMTs. This was possible because the WLS bars were only 2 mm thick, allowing a fraction of the scintillator light to pass through. A uniformity of better than 3% was achieved in this manner. The PMTs used were Phillips XP1911 for FCAL EMCs and Hamamatsu R580 tubes for the HACs, and RCAL EMCs. All the tubes had Cockcroft-Walton active bases generating the high voltage on the dynodes.
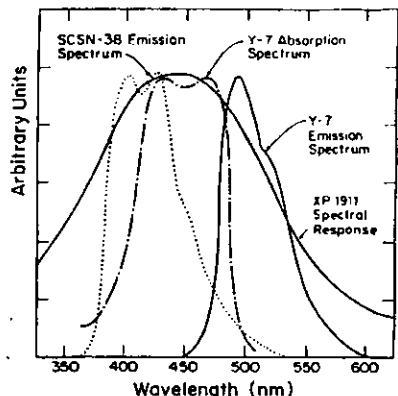
Figure 4-4 The absorption and emission spectra of materials used in the CAL optical readout

	FCAL	BCAL	RCAL	total
weights (tons):				
DU	182	230	105	517
steel boxes	18	24	10	52
SCI	8	10	5	23
total including structure	240	310	157	707
parts:				
DU plates	4200	3808	2440	10448
SCI tiles EMC	27456	40704	13286	81446
SCI tiles HAC0	5096	—	4940	10036
SCI tiles HAC1	36800	21952	35200	93952
SCI tiles HAC2	33280	21952	—	55232
SCI tiles total HAC	75176	43904	40140	159220
channels:				
EMC	2112	3392	1022	6526
HAC	2232	1792	1284	5308
total	4344	5182	2306	11834

Table 4-1 Summary of calorimeter parameters (from [36])

4.2.2.2 The calorimeter readout

Several constraints are imposed on the calorimeter readout by the high crossing frequency of the HERA machine. Firstly, since the digitization of the PMT signals is the slow part of the readout process, the dead time is greatly reduced by only digitizing the signals for the events that have

passed the first level trigger (FLT) decision. This, however, means that the analogue data must somehow be kept for about 5 μs, the time required to make the FLT decision. This is achieved with custom designed switching capacitor pipeline chips [42], located on the Front End Cards (FEC) mounted on the back of each calorimeter module. The signals from the PMTs are directly connected to the inputs of the FECs, a schematic of which is shown in Figure 4-5. Upon arrival the signal
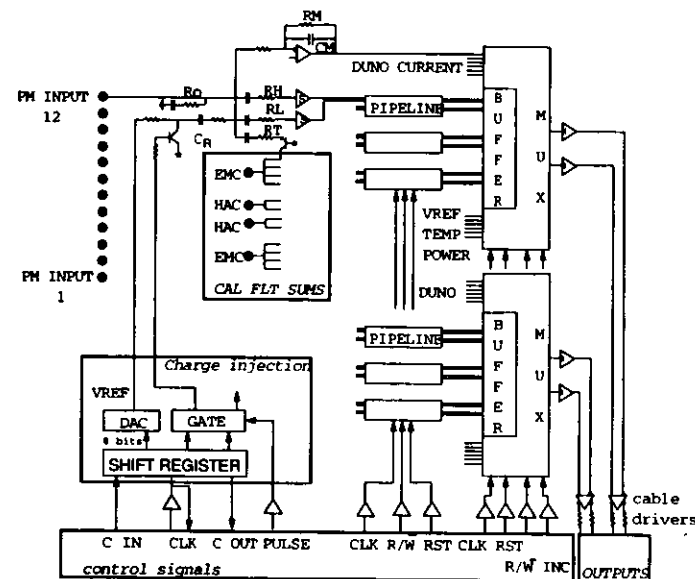
Figure 4-5 The schematic diagram of a front end card (FEC) for the CAL readout
The inputs (on the left), coming either from the PMTs or the charge injection DAC, are split into high and low gain channels. A small part of the signal goes into the trigger sums determination. There is also an integrating channel for the UNO signal for calibration (at the top). After the pipelines and the buffers (see text for discussion) the output is multiplexed to the digital cards (bottom right).

is modified by a shaping circuit, so that it covers several bunch crossings. This enables sampling of the signal at the HERA frequency and storing these charge samples in the switching capacitor pipeline. Since the frequency of a signal in a single calorimeter cell is much lower then the sampling frequency, poor reconstruction due to pulses arriving too close to each other (pile-up) is minimal. When a positive trigger decision arrives, the clocking of the pipeline is stopped and the cells corresponding to the triggered crossing are read out into an analogue buffer chip. The pipeline is restarted while the data from the buffer is multiplexed to the Digital Card (DC), for digitization at the rate of 1.7 μs per sample. The dead time is determined by the time needed for the transfer of

information from the pipelines into the buffers (~1.5 μs per sample for a total of about 12 μs), compared to the time between the triggered events. Thus for the maximum design rate of the first level trigger of 1 kHz the dead time due to the CAL readout is just over 1%.

Once digitized the event information is passed to the Digital Signal Processor (DSP), a simple processor that performs early data reduction and reconstruction (one per DC). It corrects the samples for cell to cell variation in pipeline and buffer pedestals and gains and reconstructs the energies and times for each PMT. This energy and time information is included in the event record if the event is selected by the trigger.

The sampled pulse, after the shaper, is shown in Figure 4-6. Also shown and labeled are six of the eight samples that are digitized and used to reconstruct the charge and the time of arrival of the pulse with respect to the HERA clock. The electronics are timed in so that for time zero the fourth and fifth samples are equal. These same samples are also used to reconstruct the charge of the pulse, and hence the corresponding energy deposited in the calorimeter. The charge and time are calculated from the samples as:

$$H' = (h_4 - h_2) + 1.8 \cdot (h_5 - h_2) \qquad (4\text{-}9)$$

$$T = \frac{(h_5 - h_2) - (h_4 - h_2)}{H'}, \qquad (4\text{-}10)$$

where the samples h_i are as defined in Figure 4-6. The baseline sample, h_2 (not shown in the figure), is subtracted to eliminate the low-frequency noise, which produces a shift in the baseline [42]. The factor of 1.8 reflects the different slopes of the pulse shape at the two sampling times used for the reconstruction. The method used assumes a triangular pulse shape, and is only valid at $t = 0$ (i.e., when $h_4 = h_5$). This is corrected using a polynomial as a function of time for both H and T:

$$H = H' \left(1 + \sum_{n=1}^{4} c_n T^n \right), \text{ and} \qquad (4\text{-}11)$$

$$T = \sum_{n=1}^{3} d_n T^n \qquad (4\text{-}12)$$

where the constants c_n and d_n are the coefficients of the correction polynomials determined separately for each type of event (e.g., laser, charge injection, beam), by special time scan runs. Furthermore, the range of the measured time is restricted to -64 ns to 64 ns, forcing the values outside these limits to ± 64 ns. This is done to enable packing the time information in one computer word (8bits), to reduce the total size of the data.

The charge in the pulse is linearly related to the reconstructed amplitude H. The determination of the proportionality constant is discussed in Section 4.2.2.3.
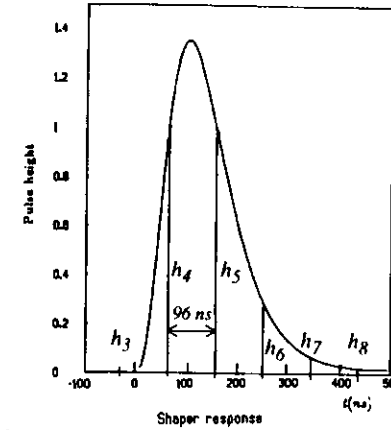
Figure 4-6 Pulse shape after the shaper circuit
The diagram shows the shape of the PMT pulse after the shaper circuit. A few of the points at which the sampling occurs are also indicated. The samples h_4 and h_5 are the main samples used in the energy and time reconstruction.

The signals are also split into high and low gain shapers, to provide the required dynamic range coverage of 17 bits (2^{17}). The lower bound of this range is defined by the uranium noise signal, used for calibration (~100 MeV equivalent) which needs to be measured with percent accuracy. The upper bound is defined by the energies reachable in the HERA collisions (~400 GeV in the forward direction). For reconstructing the energies the high gain is used, unless any of the high gain samples is saturated, in which case the low gain information is used. At the DSP level only the samples used for the reconstruction are corrected for pipeline and buffer pedestals and gains, to save on the processing time.

4.2.2.3 Calibration

There are several aspects to the calibration of the ZEUS calorimeter. First of all the front end electronics need several hundred constants per channel, including, for example, the gains and pedestals for each of the 56 pipeline cells. These constants are obtained independently of the PMT signals, by taking pedestal and charge injection runs, in which a known charge is injected into the shaper circuit. By stepping through the individual capacitors and buffer registers and reconstructing the injected charge, the calibration constants are determined for each channel. The next level of calibration constants, the transition to energy in the calorimeter from the reconstructed charge, was determined in extensive beam tests at CERN and FNAL [43]. The modules were tested in electron, muon and hadron beams between 10 and 110 GeV. It was found that the response is linear within ±2% and that the uniformity in response of different modules is better than 1%. The energy resolution for electrons was measured to be $17.6\% / \sqrt{E}$ in FCAL, $17.4\% / \sqrt{E}$ in RCAL and

$19\% / \sqrt{E}$ in BCAL modules, and for hadrons $34\% / \sqrt{E}$. Furthermore, the calibration can be monitored and maintained at an excellent level of 1% through the use of the natural radioactivity signal from the uranium plates (UNO) which is also measured by a special integrating channel of the readout electronics. Finally, almost all the modules were subjected to cosmic ray tests, the observation of the muon peak being yet another way of cross checking the calibration. There are also optical fibers leading to each PMT, enabling a controlled light emission onto the photocathodes from laser and LED systems. This enabled the check of the readout electronics at signals equivalent to energies higher than those available in testbeams.

4.2.3 The Luminosity Monitor (LUMI)

The luminosity detector consists of a pair of calorimetric detectors located downstream in the electron direction (negative z in the ZEUS coordinates), after the bending magnets which separate the electron beam out of the single beam pipe in the interaction region. The first one (LUMIE) detects scattered electrons. The second one (LUMIG) is on the zero degree line and detects radiative photons from the interaction region.

The arrangement of the luminosity detector within the HERA tunnel is shown in Figure 4-7. At $z \sim -20$ m a set of dipole magnets separate the electron beam from the common beampipe surrounding the interaction point into a separate electron beampipe. The electrons which have lost some of their energy in the interaction region are bent away from the nominal orbit. An exit window is installed for these electrons and the LUMIE detector is positioned at -35 m to catch these lower energy electrons.

The photons produced collinear with the incident beam (be they from bremsstrahlung, $ep \rightarrow ep\gamma$, or from a radiative process, $ep \rightarrow e\gamma X$) can exit the beampipe through the window at $z = -92$ m and are detected in the LUMIG detector placed at $z = -106$ m. In front of this detector there is a carbon filter shielding it from the synchrotron radiation from the electron beam

Both LUMI detectors are also sampling calorimeters, made of 5 7 mm lead plates for the absorber and 2.8 mm SCSN38 scintillator (same type as in the CAL) for the active layers. LUMIE is 250x250 mm^2 in cross section and 24 X_0 deep, while LUMIG is 180x180 mm^2 with a depth of 22 X_0. The calorimeters are read out through wave length shifter bars on both sides, the light from which is collected by phototubes attached to their ends. The energy resolution of both detectors, as determined from beam tests at CERN is $18\% / \sqrt{E}$.

The luminosity is measured by counting the bremsstrahlung photons in the LUMIG detector. The cross section for this process is accurately calculated from QED. Thus by counting the rate of such events, corrected for background and the acceptance of the LUMIG detector, the luminosity is measured.
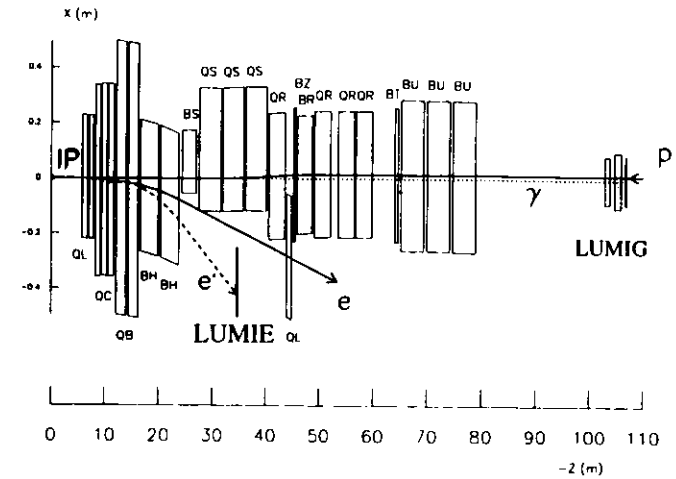
Figure 4-7 The setup of the luminosity detector (LUMI)
The HERA layout upstream in the electron direction (-z) is shown here, including the bending magnets separating the electron from the proton beam (up to ~15 m) and the bending magnets that bring the proton beam into the level of the electron beam orbit for the head-on collisions. The LUMIE detector (~35 m) catches electrons that lose energy and bend away from the nominal trajectory, while the LUMIG detector catches the photons coming straight from the interaction point.

This technique yields the luminosity with an error of ~ 2.5% [44].

In the analysis presented in this thesis the LUMIE detector is used for event selection, and the LUMIG detector is used for background substraction (see Section 6.2.1).

4.2.4 The Central Tracking Detector (CTD)

The Central Tracking Detector (CTD) in the ZEUS detector is a cylindrical drift chamber for the measurement of charged particle trajectories. Its inner radius is 16 cm and its outer radius is 82 cm. The wires are arranged into cells containing 8 sense wires each. The cells are grouped into nine concentric superlayers, of which three (1, 3 and 5) have z by timing readout. Axial (parallel to the chamber axis) and stereo ($\pm 5°$ from the chamber axis direction) layers alternate (starting with axial) to provide polar angle information. The stereo angle was chosen to achieve similar resolution in polar and azimuthal angles. A typical octant of the CTD wires layout is shown in Figure 4-8. The coverage of the CTD in the polar angle extends from 15° to 164°.

Tracks of charged particles can be reconstructed from the wire signals and the transverse momentum p_T, of the particles is measured from the curvature of these tracks due to the solenoidal

Figure 4-8 The layout of a typical octant of the CTD
The CTD has nine superlayers with eight sense wires each. The stereo angles enabling polar angle determination are also indicated beside each superlayer.

field. The momentum resolution is $\Delta p_T/p_T = 0.005 p_T + 0.016$ (p_T in GeV/c), and the hit position resolution is about 250 μm. The reconstructed tracks from the CTD are also used to determine the event vertex position with an accuracy of 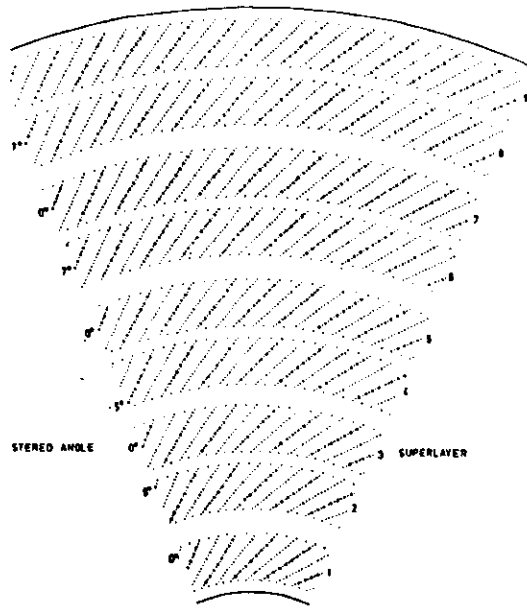about 2 cm in z, which is one of the criteria used for background recognition. Furthermore, matching of tracks with clusters of energy deposits in the calorimeter provides a means of distinguishing calorimeter deposits due to charged and neutral particles.

4.3   Trigger and DAQ

At HERA the 10 MHz bunch crossing frequency makes the selection of interesting physics from the huge background a non-trivial challenge for the triggering systems of the experiments. The main background, denoted beam-gas, comes from the collisions of the beam protons with residual gas molecules in the beampipe vacuum. Further background comes from cosmic rays passing through the detector, halo particles accompanying the proton beam, and electron-gas collisions. As well, there are detector effects such as calorimeter "sparks", occasional electrical discharges in the PMT housings producing huge signals in a single PMT tube of the calorimeter.

The ZEUS trigger is a three stage operation, reducing the rate to a final manageable level of about 5 Hz, which is saved on mass storage. This section describes briefly the different parts of the ZEUS trigger and data acquisition system (DAQ).

4.3.1   The First Level Trigger (FLT)

At this early level the time constraint is extremely important. The decision of whether to keep an event or not must be made within 46 beam crossings, or 4.4 μs. During this time the data is kept in analogue or digital pipelines. Detector components used in the first level trigger decision produce their own FLT signal. The quantities used at this level are mostly simple threshold decisions on energies and sums of energies. Some very primitive pattern recognition is also done at this level, such as the isolated muon and isolated electron flags in the calorimeter and the track triggers in the CTD. All the component FLT signals are passed to the Global First Level Trigger (GFLT), a programmable logic array that makes a decision based on all the component information. When a positive decision is sent back to the components the data is read out, digitized and passed on to the component second level triggers.

The calorimeter first level trigger (CFLT) makes fast sums of the channels in calorimeter towers and certain combinations of them available to the GFLT. The CFLT quantities used in the analysis presented in the later chapters are the REMC, the BEMC and the REMCTH. During the '93 running period the REMC was the total energy in the RCAL excluding the ring of cells immediately next to the beampipe. The sum was made only for the towers in which the total energy exceeded 464 MeV[1]. The BEMC was the equivalent quantity for BCAL. The REMCTH was a sum of the threshold bits for all the RCAL towers (including the ones surrounding the beampipe). The threshold bits were set for each tower depending on the energy deposited in that tower. For a more detailed description see [45].

The FLT is designed for an output rate of 1 kHz.

4.3.2   The Second Level Trigger (SLT)

At the second level the digitized data are available to the individual component processors. The component SLTs are based on networks of simple processors called transputers. More complex algorithms are implemented at this level, such as cluster and track finding, spark recognition and rejection, timing cuts, and even some level of cosmic ray rejection. Once again, the component decisions are collected by the Global Second Level Trigger (GSLT) and combined into the final decision. On the arrival of the positive GSLT decision the data is passed by all the components to the Event Builder for the formation of the event structure.

_____

1. at the FLT level 1 bit = 464 MeV

The SLT is designed to reduce an input rate of 1 kHz to an output rate of 100 Hz.

4.3.3 The Event Builder

The Event Builder collects the data from all the components, as well as from the first two levels of the trigger and combines it into the event records, in the same format that they are written out if they pass the final trigger level. Since it is the first component to receive the data from all the components it is also a convenient point for simple monitoring of the experiment. After formatting the event into ADAMO [46] tables the Event Builder crates distribute the events to the third level of the trigger.

4.3.4 The Third Level Trigger (TLT)

At this level for the first time the complete event is available to the trigger processors. The TLT consists of a farm of 36 Silicon Graphics (SGI) workstations running in parallel, in six branches. The manager machine of each branch accepts events from the Event Builder and distributes them to the analyzer nodes, which run a simplified version of the ZEUS off-line reconstruction, including tracking, electron and muon finding algorithms. The decision is based on the selection criteria developed by the ZEUS physics groups in order to ensure high efficiency for the interesting physics, and a high degree of rejection for the backgrounds. The events are passed on to the IBM link if any of these physics filters accepts them.

The TLT is designed to reduce the 100 Hz input rate to an output rate of 5-10 Hz.

The IBM link passes the data onto the DESY IBM for mass storage over an optical connection. The rate of the TLT output is limited by the speed at which the data can be transferred over this link to the DESY IBM and written out on the cartridge tapes that are used for data storage.

"I pass with relief from the tossing sea of Cause and Theory
to the firm ground of Result and Fact."

Churchill

5 The Forward Neutron Calorimeter (FNC)

This chapter describes the setup of the test Forward Neutron Calorimeter within the framework of the ZEUS experiment. The physical description is followed by the description of the in situ tests and calibration, including the ^{60}Co source scan for uniformity checks and the measurement of the pp $\rightarrow$ nX process between HERA protons and residual gas in the beam pipe for determination of the absolute energy scale. Also described are the different simulations used to model the detector and the determination of the acceptance of the FNC. Finally, a study of the scintillation counters, to determine their energy scale, with cosmic ray muons, is presented.

5.1 Detector position, design and setup

The FNC was installed in order to detect low angle leading neutrons originating at the interaction point (IP). This is made possible by the fact that the proton beam is bent out of the horizontal plane of the interaction, hence leaving room around the zero degree line for installation of a detector of limited extent. The device that was operated during the '93 running period and its position in the HERA tunnel are described in this section.

5.1.1 Position in the HERA tunnel

The most favourable position for the FNC was determined mainly by availability of space for its installation. First of all, in order to have the most vertical space it had to be positioned as far downstream in the proton direction as possible. On the other hand it had to be placed before the beginning of the cold section of the proton ring (120 m). Furthermore, horizontal space is also limited by the presence of the electron beam elements, such as RF cavities and magnets. Finally, it had to be placed at the position where there is no other instrumentation around the proton beam pipe itself, such as vacuum pumps and Leading Proton Spectrometer stations. At the position 102 m downstream in the proton direction the proton beam pipe axis is 17 cm above the neutral line, the electron machine RF cooling pipes are 40 cm away and there are no proton beam line elements for 3 m (between two vacuum pumps). This was the position chosen for the installation of the test FNC. A schematic diagram of the proton beam line elements between the FNC and the interaction point is shown in Figure 5-1.
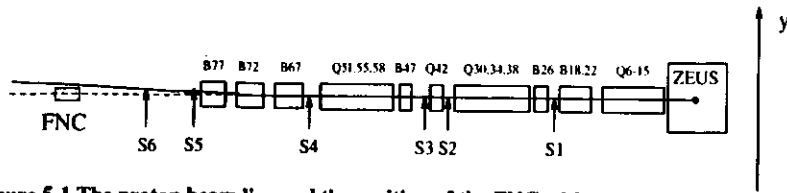
Figure 5-1 The proton beam line and the position of the FNC with respect to ZEUS
A schematic side view of the proton machine is shown here. Dipole bending magnets are labeled with B's, while the focusing quadrupoles are labeled with Q's. Both letters are followed by the distance of the element from the interaction point in meters. S1-S6 are the positions of the six LPS detector stations. The last three dipoles bend the beam upwards, allowing the placement of the FNC underneath the beamline on the zero degree line.

5.1.2 Detector setup

The above described size constraints, together with availability of materials and parts, were the deciding factors for the design and implementation of the prototype. The whole setup was placed on an aluminum table positioned under the proton beam such that the apparatus was centered on and aligned with the beam-line at the interaction point, which is also the z axis of the ZEUS coordinate system. The prototype consisted of the calorimeter and three scintillation counters used for triggering and data selection purposes. The layout of these detectors is shown schematically in Figure 5-2. Lead walls were constructed (using 5 cm lead bricks) along the two sides, as well as
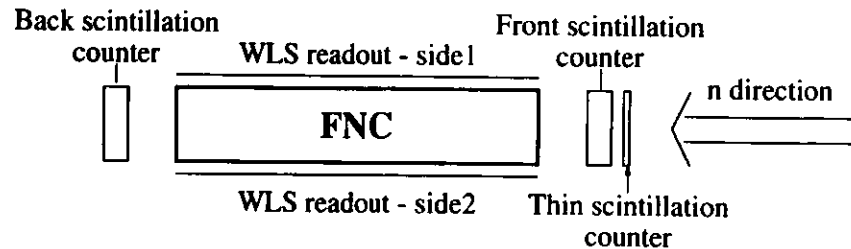

Figure 5-2 Setup of the subdetectors for the FNC prototype

behind, in order to shield the active detectors from synchrotron radiation and other low energy particles in the tunnel. Thin lead sheets (0.5 cm) were also placed as low energy photon filters immediately in front of both the front and the back scintillation counters. There was no shielding installed on either the bottom or the top side.

The calorimeter itself was a 20x20x170 cm^3 iron-scintillator sampling calorimeter, consisting of 15 cells each with 10 cm iron block followed by two 0.26 cm scintillation tiles. The light from the scintillation tiles was collected into wavelength shifter bars running down both sides of

the calorimeter, thus providing redundant readout of the single calorimeter channel, similar to the CAL solution described in Section 4.2.2. In fact, the scintillation tiles, WLS bars, and the PMTs are all of the same type as used in the CAL. One difference is that the backreflector pattern used in the CAL to make the response from different scintillator layers uniform was not available. Instead, absorption masks were positioned between the WLS and the edges of the scintillation tiles at each of the 15 layers. The masks were made from tevlar transparencies by printing a random distribution of black dots absorbing the percentage of light required to correct for the attenuation effects in the WLS material. These masks reduced the layer to layer deviation from the original 40% down to 20%.

According to [40] this combination of absorber and scintillation tile thicknesses is supposed to compensate (see Section 4.2.1.3), keeping the constant term in the resolution function down, although not at zero, since the leakage out the sides of the calorimeter, due to the limited transverse size, contributes to the constant term significantly. The longitudinal leakage is small ($< 5\%$), implying that the response should be quite linear with energy.

Each of the two thicker scintillation counters were 15x15x5 cm^3, with the PMT directly glued to one of its edges. Their position is shown in Figure 5-2. The thin counter had dimensions 18x18x0.25 cm^3 and was read out through a light guide leading to a PMT. The light guide was bent sharply through an angle of 90°, decreasing the light yield reaching the PMT. These scintillation counters are described in more detail in Section 5.4.

5.1.3 Readout

5.1.3.1 Modifications for the FNC

The readout was totally based on the ZEUS Calorimeter (CAL) readout which was described in Section 4.2.2.2. Only the modifications necessary to account for the remote location of the FNC are discussed here. The front end electronics for the FNC were located in the electronics hut (rucksack) in the experimental hall (as opposed to right next to the detector as in the case of the CAL). The general layout of the FNC readout is shown in Figure 5-3.

The CAL readout electronics require the control signals to the Front End Card (FEC) to be in time with the arrival of the phototube signals. Since the FNC phototube signals arrive at the FEC considerably later, the control signals for the FNC readout must be delayed accordingly. Figure 5-4 shows the different physical parts involved and their relationship. The relevant propagation times are also labeled in the diagram. If the CAL control signals are to arrive at the FNC FEC at the same
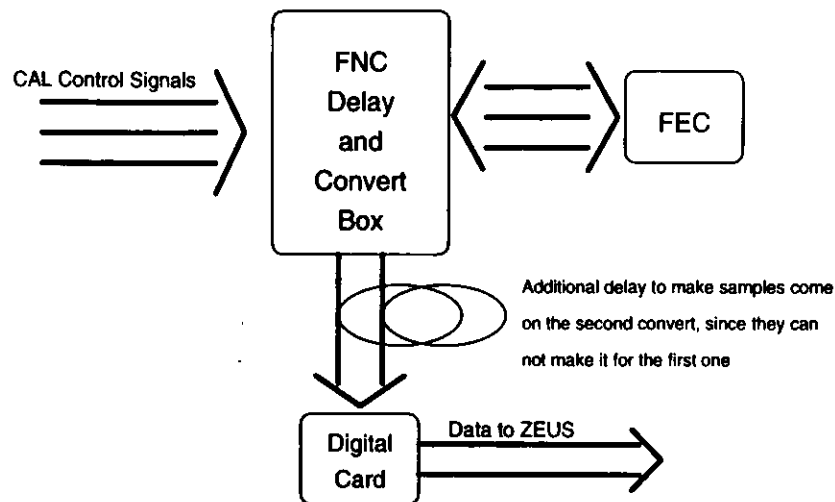
Figure 5-3 The layout for the FNC readout
Due to the remote location of the FNC and the position of the FEC with respect to the detector several delays had to be implemented in the readout in order to send the FNC data as a part of the CAL data stream.
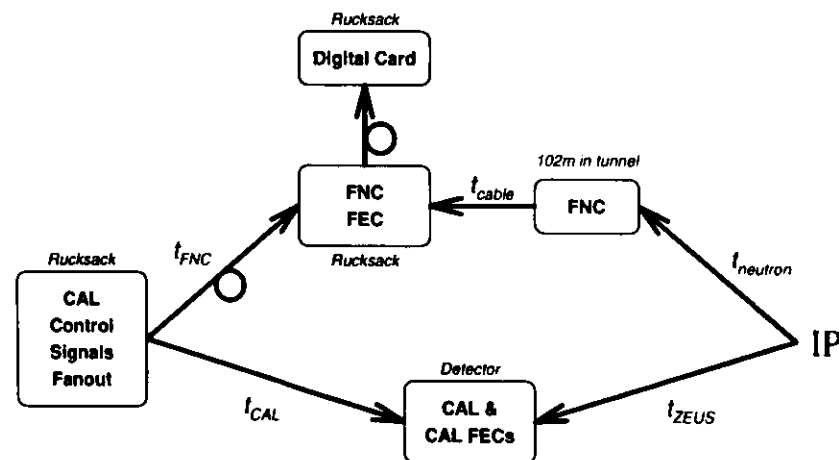

Figure 5-4 Timing of the FNC readout
The position of the FNC and its readout components compared to those of CAL are shown. The relevant propagation times are also labeled. The delays that had to be added for the FNC readout are shown as loops.

time with respect to the PM signals as they do to the CAL FECs then the following relation must hold:

$$(t_{CAL} - t_{ZEUS}) = (t_{FNC} - (t_{cable} + t_{neutron}))$$ (5-1)

Given that $t_{CAL} \approx 250$ ns, $t_{ZEUS} \approx 0$ ns, $t_{neutron} \approx 340$ ns, $t_{cable} \approx 820$ ns it follows that:

$$t_{FNC} \approx 1400 \text{ ns.}$$ (5-2)

Hence, the CAL control signals have to be delayed by approximately 1400 ns before driving the FNC FEC. This time scale is important for only six of the control signals, the others being states which are not sensitive to time shifts of this level. In addition, the pipeline clock must retain its phase and duty-cycle without significant electronically introduced jitter; hence it is delayed by cable located in the cable shaft of the rucksack. The buffer clock is also delayed by cable, due to the deficiency of the delay circuits used. The remaining four signals are delayed using adjustable delay-time circuits, which allow for easier timing in of the control signals.

5.1.3.2 The delay and interface box (DIB)

All the signals interfacing with the FEC are contained in the FNC Delay and Interface Box (DIB), which is a custom made module that plugs into a NIM crate for power. It receives the CAL control signals through a 25 pin flat cable and three pairs of LEMO connectors, converts them to ECL or TTL standards as needed, delays the ones that need to be delayed, and passes them on to the FEC. The design of the DIB follows the layout of the CAL fanout boxes located at each F/B/R-CAL module. A schematic of the DIB is shown in Figure 5-5.

For the adjustable delays two types of delay mechanisms were used depending on how the width of the input signals compares to the length of the delay itself. Figure 5-6 a) shows the circuit suitable for delaying pulses much longer then the delay time. Both read/write pulses and the charge injection pulse are delayed this way. The circuit used for the buffer increment signal, which is short compared to delay length, is shown in Figure 5-6 b).

5.1.3.3 The digital card readout

The output signals from the FEC are digitized by a CAL Digital Card (DC). The convert signals for the DC (specifying the time to start the digitization) could not be delayed. Consequently, the first sample convert is too early for the FNC signals. It was therefore decided to time in the arrival to the DC for the second convert signal, which is quite satisfactory, since the first sample is not used in the pulse reconstruction algorithm. The additional length of cable delay required between the FEC and the DC was determined by doing a time-scan run with the CAL stand-alone run control, changing the time of arrival of the convert pulses to the DC.
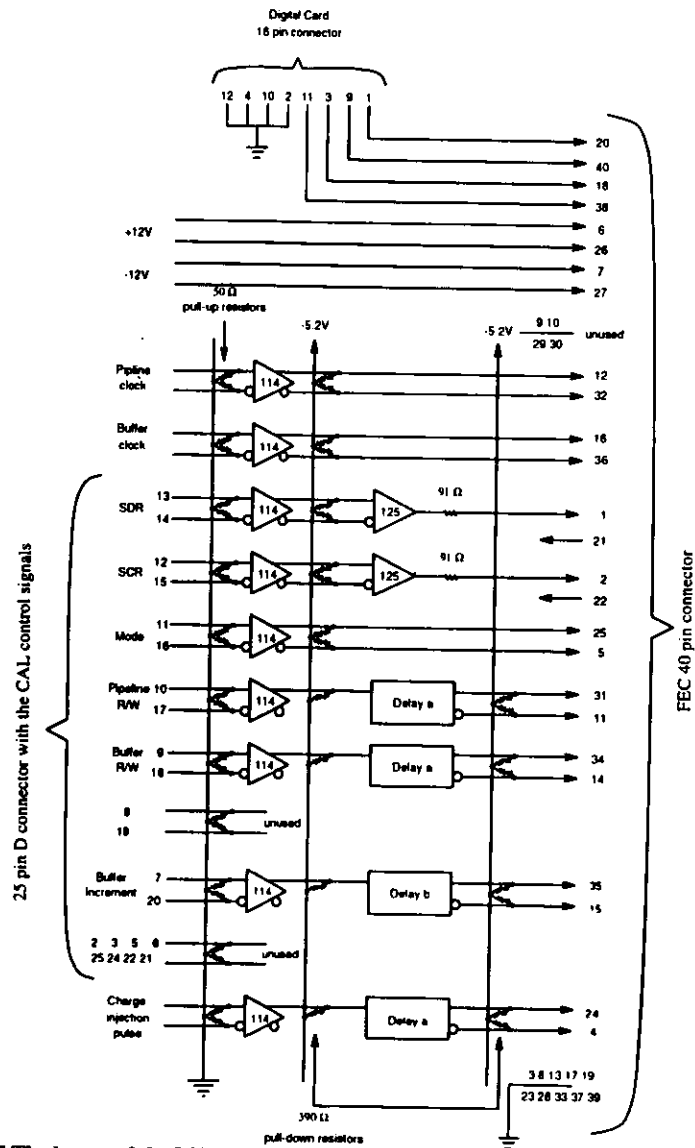
Figure 5-5 The layout of the DIB

NIM input signals arrive from the CAL control electronics (on the left). They are converted to ECL (first column of components), the serial clock (SCR) and the serial data (SDR) are converted to TTL while the read/write signals, the increment, and the charge injection pulse are delayed. All the control signals are passed on to the FEC (on the right), and the output of the FEC is passed on to the digital card (on the top).
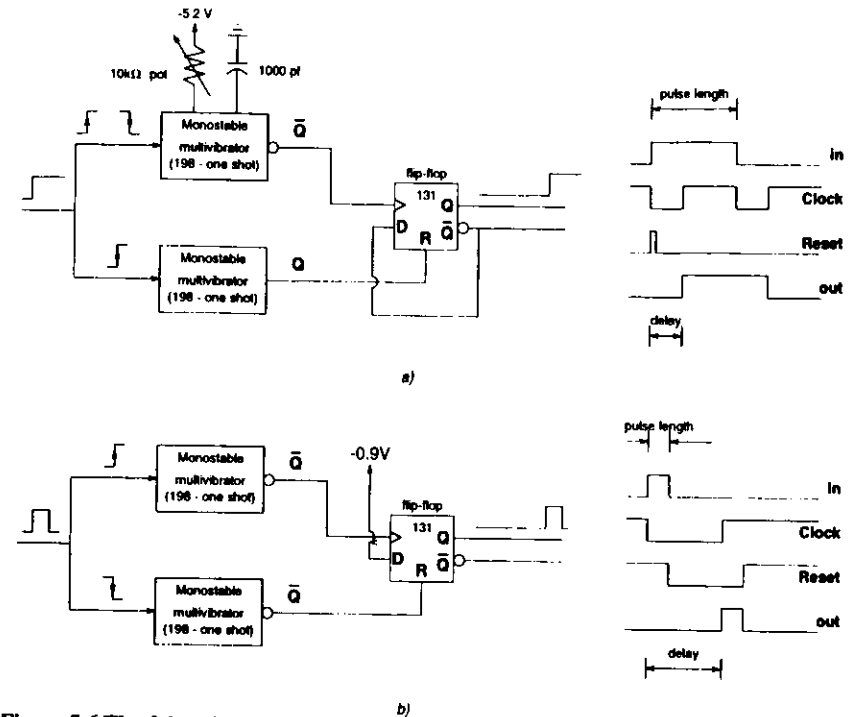
Figure 5-6 The delay circuits used in the DIB

The delay circuits are based on two multistable vibrators followed by a flip-flop. The logic level diagram for input, output and two intermediate stage signals are shown at the right. The setup in a) works for input pulses longer than the delay time, while the one in b) works for input pulses shorter than the delay time.

Since the amount of data is small for the FNC, the digitized samples from the DC are read out for all events, rather than just the reconstructed energies and times. The energy is reconstructed off line from the samples using the same reconstruction algorithm as that for the main calorimeter (described in Section 4.2.2).

5.1.4 The FNC trigger

Two trigger signals were sent to the GFLT (see Section 4.3.1) by the FNC. The neutron calibration trigger (FNC_calib_neutron) consisted of a coincidence of the two calorimeter channels each exceeding a threshold of about 100 GeV. The muon trigger was a coincidence of the front and back scintillation counters. They were implemented by splitting each of the PMT signals into two, one half going into the readout electronics, the other half into the trigger logic. The trigger logic consisted of NIM discriminators and coincidence units, with a NIM logic output pulse going directly to the GFLT.

Neither of the triggers was used in the decision making during the regular physics running. The energies in each of the five PMTs were recorded in the data stream regardless of the FNC trigger condition, for all the events that were saved to mass storage by ZEUS.

Special runs were taken with these triggers, for testing and calibration purposes.

5.2 Tests and Calibration

Since this prototype was built in the HERA tunnel and with a rather tight time schedule, there was no chance for use of test beam to test and calibrate it. Also the energies at which it was expected to perform (up to 820 GeV) are not easily available in test beam conditions. This lead to the in-situ calibration and test procedure described here.

5.2.1 ^{60}Co uniformity scans

A ^{60}Co source was used to scan the two sides of the calorimeter to check for any non-uniformities due to construction faults, as well as to check the effectiveness of the absorption masks described earlier. The scans were done using the CAL system with an external tube driver [47], with tubes taped to the middle of each calorimeter side. Figure 5-7 shows a sample scan down the
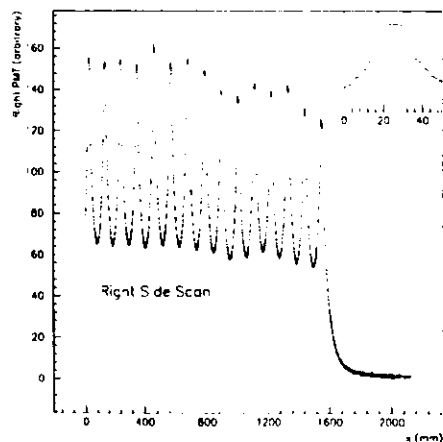
Figure 5-7 A ^{60}Co source scan along the right side of the calorimeter
Each of the peaks corresponds to the source passing by one of the scintillator layers. Note that there is still a dropping trend towards the front layers, indicating that the absorption masks did not work perfectly. Figure from [48].

right side of the calorimeter. Each peak corresponds to the source travelling by one of the scintillator layers. The 15 peaks are spaced by approximately 10 cm, the thickness of the iron absorber

blocks. The inset plot shows the expansion of the first peak (at the left). The width of the flat section reflects the width of the gap between the iron blocks (~ 1 cm). The plot also shows that the masks have not completely removed the attenuation effect in the WLS. There is still ~20% difference between the highest and the lowest peaks. This is significantly better than the 40% spread that was measured in a test setup without the masks. The remaining spread is mostly due to the imperfection of the mask patterns and was reduced to 5% for the next version of the FNC detector, by optimizing the pattern for the best uniformity. The ratio of the left and right PMT responses in the scans down the left and right sides yields a relative gain of the two FNC channels of 1.2. The data from the scan also indicate layer to layer uniformity of the relative gain to be within 4%. (For details see [48]).

5.2.2 Calibration of the FNC

To determine the energy scale calibration the neutron spectrum from the pp → nX reaction was measured and compared to the theoretical prediction obtained from the OPE model, using the pion flux given in Eqn. (2-24). A sample of 50,000 such Monte Carlo events after the simple Monte Carlo described in Section 5.3.1 are used for comparison throughout the next sections. Energy scaling is assumed: the same Monte Carlo sample, just scaled down to the appropriate energy, is used when spectra at lower incoming beam energies are shown. Since the pion flux is independent of the center of mass energy (see Eqn. (2-24)), this assumption is equivalent to assuming that the πp cross section is constant at these energies. The hadronic data indicates that this is a good approximation [49]. The vertex was assumed to be uniformly distributed in a 30 m interval around the interaction point, which corresponds to the region of worst vacuum, hence higher concentration of residual gas molecules and higher beam gas collision rate.

5.2.2.1 Calibration at 820 GeV

The coincidence trigger between the left and the right calorimeter channels was used to take five FNC neutron runs during the running period. A summary of these runs is shown in Table 5-1. Energy was calculated using the following formula:

$$E_{FNC} = (CAL1 + CAL2 \cdot G_{rel}) / G_{tot} \qquad (5\text{-}3)$$

where $CAL1$ and $CAL2$ are the reconstructed signals in the two calorimeter channels, G_{rel} and G_{tot} are the relative and overall gains respectively.

The relative gain was determined as the mean of the ratio of the two channels, and the overall gain by minimizing the chi squared of the fit between the high energy falling edge of the data neutron spectrum and the OPE prediction.

The obtained spectrum, combined over all five runs, is shown in Figure 5-8. The overall gains shown in Table 5-1, which represent the energy scale calibration, were determined by mini-
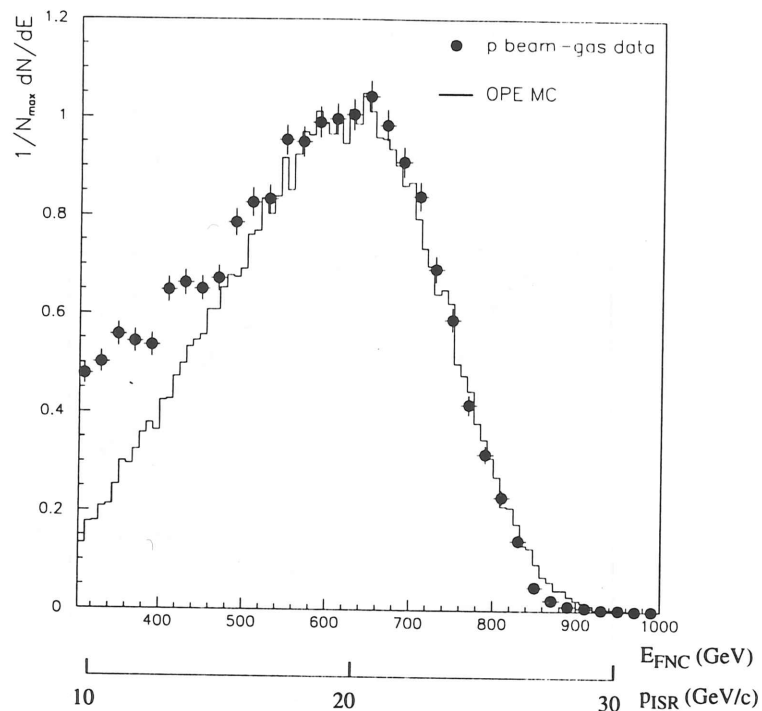
Figure 5-8 Neutron runs spectrum from pp → nX

The beam gas collisions data is well described by the OPE model. This agreement was used to determine the energy scale calibration of the FNC by minimizing the χ^2 between the data and the Monte Carlo on the falling edge of the distribution (above 625 GeV). Also shown is the equivalent momentum scale after the transformation to the ISR reference frame, for comparison with Figure 5-11.

Run number	Date	Number of events	Relative gain	Overall gain	Overall gain error from χ^2 fit
6392	Aug. 16	21694	0.95	1.19	± 0.021
6905	Sep. 14	17716	0.95	1.13	± 0.027
7120	Sep. 29	8169	0.94	1.15	± 0.040
7491	Oct. 26	20033	0.92	1.07	± 0.021
7559	Nov 5	16908	0.93	1.03	± 0.019

Table 5-1 The summary of calibration runs

mizing the χ^2 of the fit between the data and the Monte Carlo prediction (also shown in Figure 5-8 as the solid histogram). The fit was performed in the high energy region above the peak of the dis-

tribution. This was due to a disagreement in the low energy region explained by the contamination from centrally produced neutrons (see Section 2.5), as well as neutral deposits by preshowered neutrons (see Section 5.4). A typical χ^2 distribution (for run 7559) is shown in Figure 5-9. From this
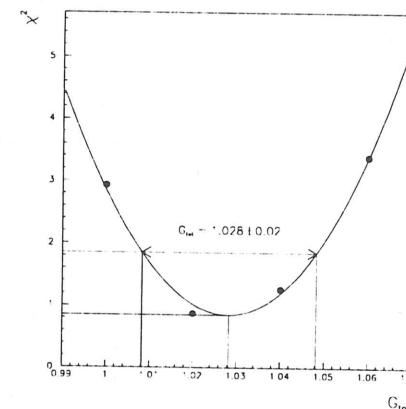
Figure 5-9 χ^2 distribution for run 7559
Typical distribution of the χ^2 between a neutron run data and the OPE Monte Carlo for varying the energy scale. The mean and the error are indicated on the graph.

distribution the statistical error on the absolute energy scale is estimated by the range in gain over which χ^2 increases by one. These errors are also shown in Table 5-1. The error on the energy scale was then taken to be the weighted average over these runs, and is 2.1 %. There is a comparable systematic error on the overall gain coming from the variation of the timing cuts used in data selection. The gain decreased over time, as seen in Figure 5-10. A similar decrease in gain was observed in the tests of these PMTs done for the main calorimeter (see [36]). The straight line fit shown in the same figure was used in calculating the energy in the FNC between the calibration runs.

5.2.2.2 Comparison to the ISR measurement

At the CERN ISR collider, Engler et al have measured the neutron spectrum at the angle of 20 mrad [32][50]. Previous to the ZEUS measurement presented here (Figure 5-8) these were the lowest angle measurements available. Their measurement at the center of mass energy of $\sqrt{s}$ = 53 GeV and at three different angle settings are shown in Figure 5-11. The measurement most comparable to the ZEUS FNC measurement is the one at the smallest angle of 20 mrad. Several important differences have to be taken into consideration when comparing the two measurements. The ZEUS measurement is done at $\sqrt{s}$ = 40.5 GeV, and it is not done in the center of mass system. It is a fixed target experiment with an 820 GeV proton beam colliding with stationary pro-

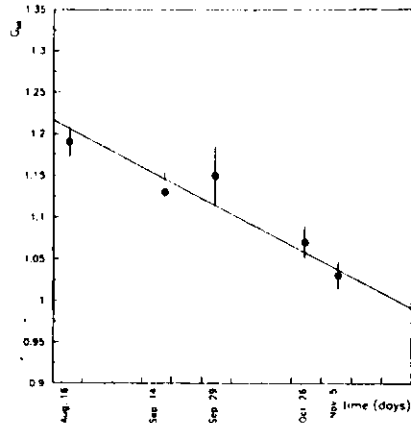**Figure 5-10 The time dependance of the gain**
The five points show the variation of the overall energy calibration of the FNC during the running period. They correspond to the five neutron runs taken (Table 5-1). The straight line fit shown was used as the calibration constant for the physics runs.
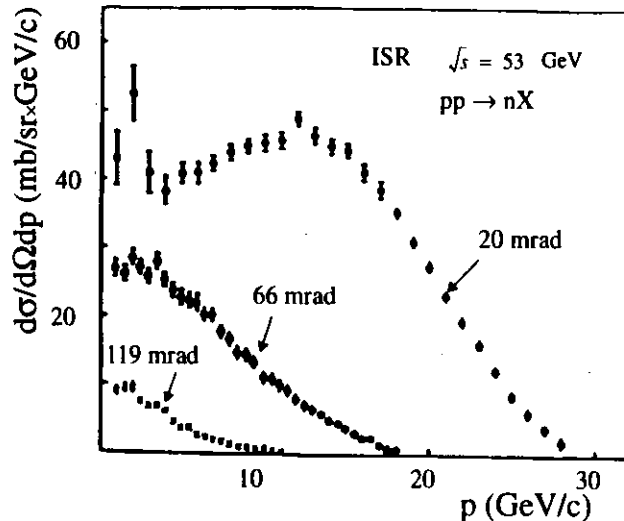

Figure 5-11 ISR neutron spectrum at 20 mrad (from [32])
This measurement of the neutron spectrum at the ISR is the closest measurement comparable to the ZEUS beam gas spectrum. Taking into account the experimental differences (see text for details) this spectrum agrees well with the FNC spectrum (Figure 5-8).

tons in the gas target. Also, even though the calorimeter was centered on the beam axis, the geo-

metric aperture within which there is a finite acceptance for neutrons is offset from this axis (see Figure 5-16 in Section 5.3) making this effectively a measurement centered around 0.4 mrad in the HERA lab frame. This is equivalent to an angle of 8 mrad in the center of mass frame. Therefore, the ISR measurement is made at about twice the angle of the ZEUS measurement. Furthermore, the aperture over which the FNC spectrum is integrated is non-uniform and has an irregular shape, with a radius of about 7 mrad in the center of mass system. Thus the FNC spectrum incorporates angles in the range of 2 - 14 mrad. The solid angle was much better defined at the ISR setup, resulting in the approximate range of 17.5 - 22.5 mrad. Even though the two spectra are measured in slightly different regions of phasespace there is a qualitative similarity between them. Both spectra exhibit a peak at a value lower than the beam energy and a falling edge extending up to the kinematic limit. The peak in the ISR data is at 13 GeV, while the ZEUS data peaks at the equivalent energy of 20 GeV (after transforming into center of mass system and rescaling to the ISR energy, assuming energy scaling). The difference in the peak position is attributed to the different angular coverage of the two detectors. This was checked by looking at the variation of the energy spectrum expected from the OPE mechanism in bins of the polar angle. It was found that the peak shifts towards lower energies as the mean polar angle is increased. In the approximate range of angles covered by the ISR experiment the OPE neutron spectrum peaks at 14.5 GeV, which is very close to the peak position in the data distribution.

We conclude that the new ZEUS data are consistent with the previous measurements made at the ISR.

5.2.2.3 The neutron spectrum at other energies

The HERA proton acceleration cycle consists of several steps. The protons are injected at 40 GeV, and a short pause is made during acceleration at 70, 300, 482 and 678 GeV to update the beam optics files. These stops have been used to collect data from pp (beam-gas) collisions at different energies, which allows a cross check of the linearity and calibration of the FNC. Measurements have been made at the 300 and 678 GeV points (plus at the full energy of 820 GeV), with full ZEUS readout used in this analysis. The obtained spectra are shown in Figure 5-12. The solid histogram in each figure is the OPE model, scaled to the beam energy. The spectrum at 678 GeV behaves the same as that at 820 GeV, and the gain calculated is 0.99, which is within the error of that obtained from the 820 GeV run taken on the same day, as expected if the calorimeter is linear. The spectrum at 300 GeV, although giving a reasonable fit for the gain on the falling edge of the spectrum, shows a large background below the theoretical peak and about 10 % lower gain. This data is, however, taken in the region where the switch between the low and high gain is made in the readout (see Section 4.2.2.2) and one of the FNC calorimeter channels showed a mismatch in gain at this point. The necessary correction implies an additional uncertainty in this lower energy spectrum. A study at all the energy points was carried out using the CAMAC stand alone DAQ
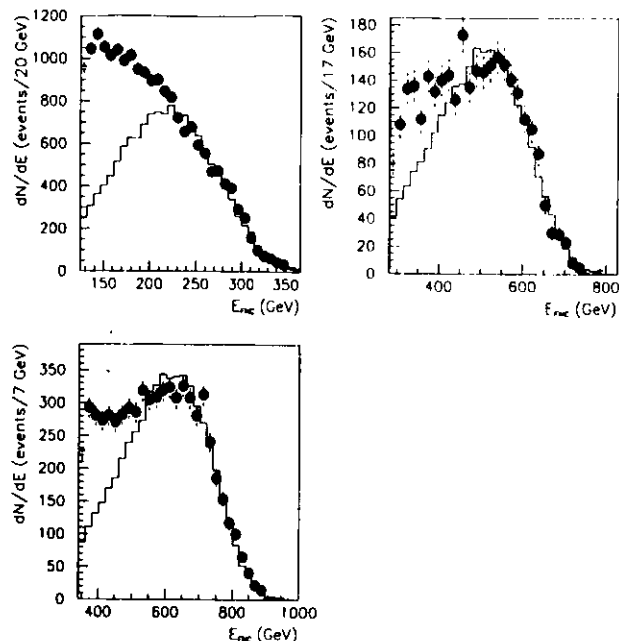
Figure 5-12 Neutron spectra at different energies
The FNC spectra at 300, 678, and 820 GeV were measured during the acceleration cycle of HERA. The data are overlaid on the OPE model prediction. The discrepancy at 300 GeV is discussed in the text.

system and is described in [48]. It shows that the calorimeter response is linear, as expected from the GEANT[1] [51] simulation.

5.3 Acceptance

The acceptance of the FNC was mainly determined by the aperture defined by the beam line elements. The view of the interaction point from the position of the FNC is obstructed, mainly by the dipole bending magnets located at 65 m. Two different simulations were used to study the effects of this aperture. The first is a simple model assuming an opaque aperture corresponding to the geometry of the magnets, followed by smearing the energy by the resolution function of the calorimeter. The second is a full GEANT simulation included in the ZEUS detector simulation program (MOZART). This section contains more description of these simulations, as well as some comparisons between them and the data from the neutron runs.

---

1. a program package used for detector description and simulation

5.3.1 The simple model

The simple Monte Carlo used consisted of selecting, at the generation level, only those events for which the neutron would not hit the beam line magnets, thus assuming that the neutron is lost if it does hit any of these magnets. The energy of the events that pass this simple geometrical aperture criterion was then smeared with the resolution function obtained from a GEANT simulation of the FNC calorimeter:

$$\frac{\delta E}{E} = \frac{173\%}{\sqrt{E}} \oplus 6\% .$$

(5-4)

The resolution was also measured from the pp → nX data. Assuming the $\delta E / E = a / \sqrt{E}$ variation of the resolution, the energy spectrum from the model was smeared for different values of the resolution parameter a. The resolution was determined by minimizing the χ^2 (as a function of a) between these expected distributions and the energy distribution from the neutron run data (Figure 5-8). The value obtained was: $a = (230 \pm 30) \%$. For details see [48]. Assuming a constant term of 6% this implies the sampling term of $(180 \pm 40)\%$ for $E = 600$ GeV. This uncertainty in the resolution results in the 1.5% uncertainty in the measured energy at the energies at which the device is used. The only effect of this uncertainty in the presented data is the change it causes in the shape of the predicted spectrum, which is negligible.

The shape of the aperture obtained from this simple model agrees well with the one from the full simulation, shown in Figure 5-16 b).

5.3.2 MOZART simulation

The full simulation contains a realistic description of the calorimeter and the storage ring magnets, as well as a simplified description of the beam line geometry near the FNC, shown in Figure 5-13. The iron flange at $z = 92$ m was introduced to simulate the dead material in front of
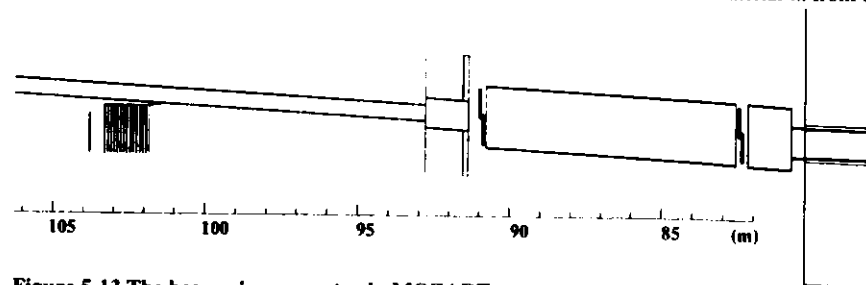

Figure 5-13 The beam pipe geometry in MOZART
The FNC setup in the ZEUS detector simulation package (MOZART), implemented in GEANT. Several different diameter beam pipes are shown as well as the flange (near the middle of the figure) simulating the passive material the neutrons must pass through before hitting the FNC.

the FNC, including the mechanical support of the S6 station of the LPS and the vacuum pumps for the proton beam line. The thickness of this flange was determined by generating neutrons from the IP and comparing the spectrum in the FNC without scintillation counter cuts to that from beam gas runs for different thicknesses of the flange. The comparison is shown in Figure 5-14. Minimizing
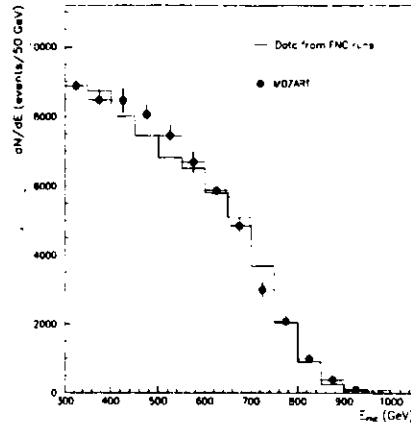

Figure 5-14 MOZART comparison to data before cuts
The comparison of the raw energy spectrum from data to that predicted by the MOZART simulation. The discrepancy in the first bin is due to neutrons produced through processes other than OPE, since the MOZART spectrum is from the OPE model only.

the χ^2 difference between these two distributions as a function of the thickness of the iron flange yielded the optimal thickness of 18.5 cm. This thickness of about 1λ agrees with rough estimates of the material present, although the exact amount is hard to calculate due to irregular shapes of the objects present (e.g., vacuum pumps) and the averaging over the neutron beam spot (see Figure 5-16 b). The MOZART spectrum after the neutron cuts is shown in Figure 5-15. Also shown is the simple MC spectrum. The agreement between these spectra is reasonably good and allows further comparison of data to the simple MC, since the statistics for the events processed through MOZART are limited by the processing time.

The acceptance of the FNC was determined from a sample of 50,000 MOZART generated neutron events. The energy and angular distributions were taken from the OPE model. These distributions play a significant role in the acceptance, since the acceptance in theta is the most limiting factor. The acceptance as a function of energy and angle was determined from this MC sample as the ratio of accepted events to the number of generated events in bins of energy and angle. The accepted events were those that have the energy within the considered energy window (400-1000 GeV) and have a deposit in the front thick scintillation counter of less then one mip. The results are shown in Figure 5-16.
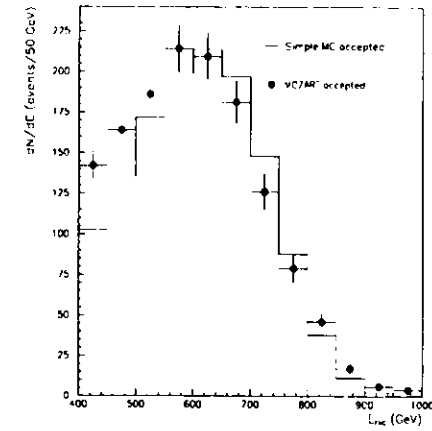
Figure 5-15 MOZART after cuts
The comparison of the MOZART and the simple Monte Carlo neutron spectra after the cuts to eliminate the background from the preshowering neutrons.
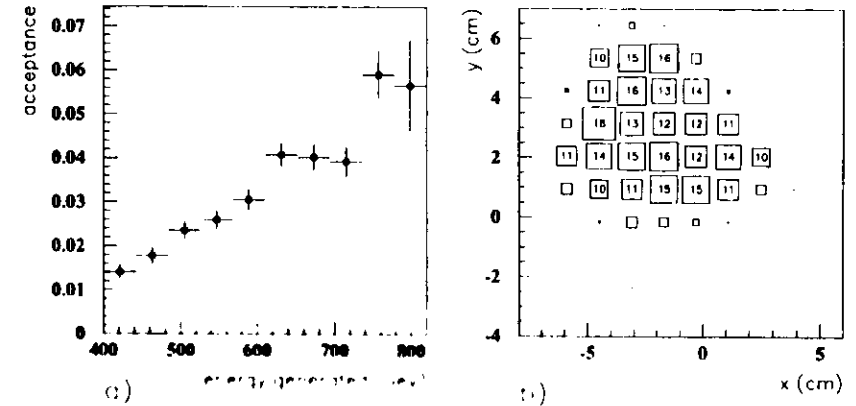
Figure 5-16 Acceptance of the FNC
The acceptance of the FNC is shown as a function of energy (a) and position at the face of the calorimeter which extends between -10 and 10 cm in both x and y directions (b). The acceptance rises with energy, while in position there is a clear aperture within which the acceptance is about 15%. The aperture is not centered on the z axis (i.e., at x = 0, y = 0).

The overall acceptance was determined as the weighted average of the above distributions, in other words as the ratio of total number of events accepted to the number generated. It was found to be:

$$A_{FNC} = (3.1 \pm 0.1 \pm 0.5)\%.$$ (5-5)

There are several contributions to the systematic error quoted:

1. uncertainty in the overall energy scale, determined by varying the energy scale and calculating the effect on the acceptance — a 2% change in overall scale (see Section 5.2.2) changes the acceptance by 2%;

2. determination of the amount of material introduced in the simulation: varying the thickness from 18.5 cm by 1.5 cm leads to a change in χ^2 of 1. Reevaluating the acceptance at the end points of this range yields an error of ~16%;

3. theoretical uncertainty due to model dependence: using the pion flux factor from [33], instead of the one from [31] changes the acceptance by 4%.

5.4 Scintillation counters

The signal in the scintillation counters is used in the analysis later to distinguish events in which the particle depositing energy in the FNC is not a single neutron, but rather one or more particles resulting from a shower produced by a particle that interacted with the inactive material upstream from the FNC. It is important to be able to make this distinction, for both the neutron spectrum and the number of events (i.e., cross section) depend on how this choice is made. The principle is to remove any events with charged particles entering the FNC.

In this section some of the features of the spectrum in the front thick scintillation counter are explained, first in a stand-alone cosmic run test and then in a typical neutron run, taken with the FNC neutron trigger.

5.4.1 Cosmic ray test

A cosmic ray run was taken with the scintillation counters used for triggering and data selection in order to determine their efficiency and energy scale. The setup for this special run is shown in Figure 5-17. Counter T is a 2.5 cm thick scintillation counter that was used for triggering only. Data was collected through the ZEUS readout chain, using a coincidence of signals from paddles T and C above a 30 mV threshold. A NIM signal was sent to the GFLT as the FNC_calib_- neutron trigger. A cosmic run with 810 events was taken. The spectra observed in all four counters are shown in Figure 5-18. The one mip peak is clearly visible in all except for the thin counter (A). Landau fits are shown for these counters and they show good agreement with the data. In counter A the mip peak is merged with the pedestal, but a tail towards higher energies is evident. This counter can clearly not be used for vetoing of single ionizing particles. From the plots for counters T and C it is also clear that the trigger threshold was well below the muon peak.

The counter used for the event selection in the analysis presented later is counter B. For this counter the cosmic run showed the most probable value of 218 units and the width of 50 for the
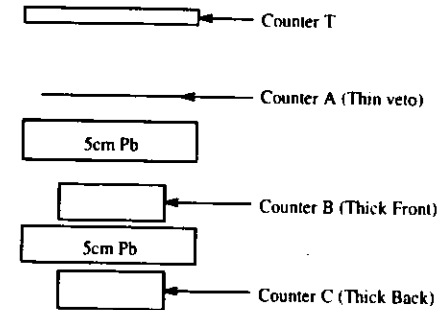
Figure 5-17 Cosmic ray run setup

In run 8005 cosmic ray signals in the scintillator counters were collected, triggering on paddles T and C in order to study efficiency and scale in counters A, B and C (the counters used in the analysis).
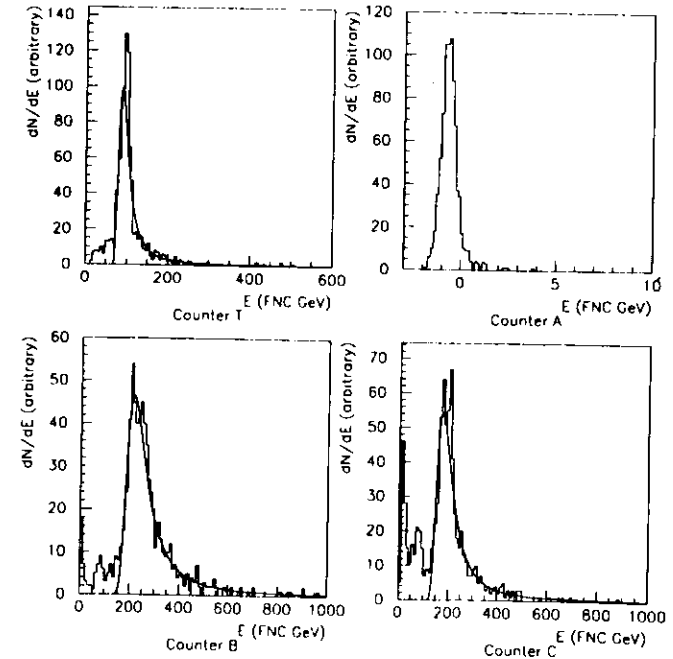
Figure 5-18 Cosmic ray spectra in the trigger counters

A clean minimum ionizing peak is seen in the three thicker counters, for which the fit to a landau distribution is also shown. In the thin counter the one mip signal is indistinguishable from the pedestal. The events below one mip in the thick counters are likely due to geometric edge effects where the cosmic muon does not pass through the entire thickness of the counter.

minimum ionizing peak. From the cosmic spectrum for counter B it can also be concluded that a cut at 150 units is well below the minimum ionizing peak. This is the value used for selection of neutrons in the pp and ep collision data.

5.4.2 The front counter in the neutron runs

Naively, one would expect that the scintillation counter positioned in front of the FNC should, in any given event, see one of two situations:

1. signal consistent with pedestal, in case there are no charged particles entering the calorimeter; these would be classified as neutrons which have not interacted before the FNC;

2. a number of relativistic charged particles, which should behave very closely to mips, traverse the counter. The spectrum expected in this case would be a convolution of a 1 mip peak, 2 mips peak, and so on with each one getting successively smaller, until they disappear in the sum of the tails of the previous ones.

This is exactly what is obtained from the MOZART simulation program shown in Figure 5-19. An

a)　　　E_f (arbitrary units)　　b)　　E_f (arbitrary units)

Figure 5-19 The front counter spectrum in MOZART for OPE neutrons
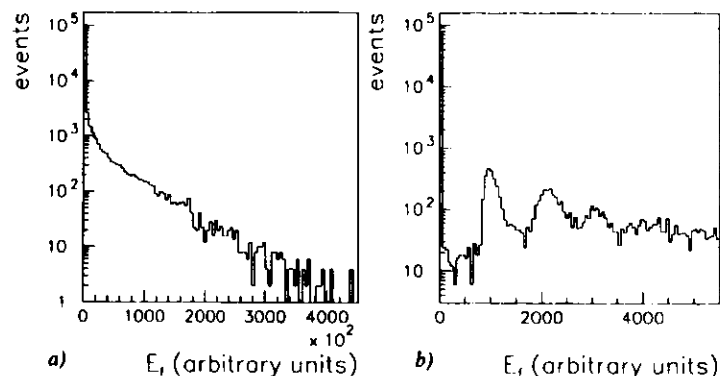*The overall spectrum (on the left) extends to several hundred mip equivalents. A closer look at the lower energy part of the spectrum, less than 5 mips (on the right), clearly shows the one mip, two mips and even the three mips peaks. (Note the logarithmic scale.)*

expanded view up to the 5 mips peak position is shown in Figure 5-19 b). From the plot in a) we see that the tail of the spectrum extends up to well over 100 mips equivalent. The events in this high energy tail correspond to showers with many charged particles hitting the FNC. The plot in b) shows a spike at zero, corresponding to no charged particles traversing the counter (it is exactly at zero since the pedestal is not simulated), followed by a clear 1 mip, 2 mips, and an indication of the 3 mips peak. The peaks corresponding to more than three mips are lost in the tails of the first three peaks.

What is not taken into account in this simple picture, as well as in the MOZART simulation is the backscattered particles from the hadronic cascade developing in the calorimeter (see Section 4.2.1.4 for a brief discussion of this phenomenon). The full effect of this contribution can be seen in the front thick scintillation counter spectrum from a typical neutron run, shown in Figure 5-20.
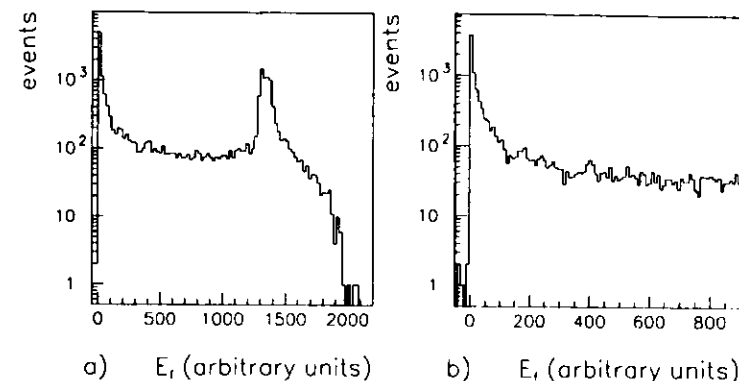

a)　　E_f (arbitrary units)　　　b)　　E_f (arbitrary units)

Figure 5-20 The front counter spectrum in a neutron run
The peak at the high end of the scale (~ 1500) is artificial, and is due to the saturation of the readout electronics channels. In the data the one mip peak cannot be seen in the expanded view (on the right). The deposits of fractions of mips are largely due to backscattered particles (see text).

The large peak at the end of the scale in Figure 5-20 a) is an artificial peak due to the saturation of the readout electronics. The lower part of the spectrum up to just below the position where 5 mips is expected (the scale being obtained from the cosmic run described in the previous section) is shown in Figure 5-20 b). There are no clear minimum ionizing peaks visible, instead there is a tail on the positive side of the pedestal extending up to and beyond the expected position of the single mip signal. These events with an energy deposit larger than pedestal, and smaller than a single minimum ionizing particle are due to the slow particles backscattered from the calorimeter. The plot of the timing versus energy in the counter supports this hypothesis (see Figure 5-21). The energy scale extends to the same position as in Figure 5-20 b). Apart from the well defined time for the high energy deposits (a flat band across the plot centered at -14 ns), there is a clear correlation that the small energy deposits arrive later (more positive time), which is expected for low energy albedo particles.

Another indication that the particles with signal in the front counter smaller than a single mip are predominantly clean neutron events comes from studying the neutron spectrum from the neutron runs in bins of energy deposits in the front counter (Figure 5-22). The first plot has the same shape as that in Figure 5-8 and is due to the "clean" neutrons (i.e., the ones that have not pre-showered in the material in front of the FNC). As the energy requirement in the front counter is
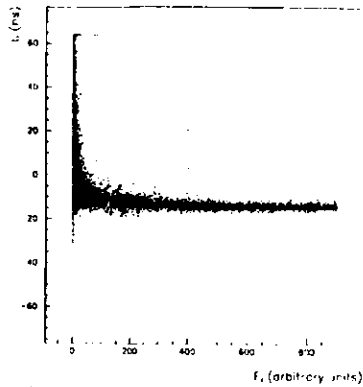
Figure 5-21 Time vs. energy in the front scintillation counter

The long tail towards positive time for the small energy deposits is an indication that these signals are due to the backscattered particles in the hadronic shower, rather than incoming charged particles.
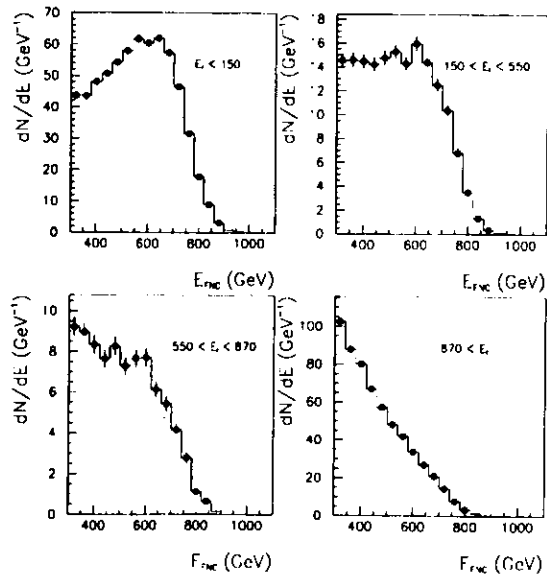
Figure 5-22 E_{FNC} in bins of E_f

The cuts on the energy in the front counter correspond to approximately 1, 3, 5 mips respectively. Note the evolution of the spectrum from the OPE like peak to the smoothly decreasing spectrum. The contribution from the "clean" neutrons decreases with the increasing energy in the front counter.

increased the contribution from preshowering neutrons increases and the peak superimposed on the

smoothly falling spectrum is less and less prominent. In the last plot when the energy in the front counter is required to be greater than about 5 mips, the enhancement from the "clean" neutrons is no longer visible.

6   Forward neutron physics at ZEUS

In this section some of the physics discussed in Section 2.5 is presented in the light of the new data collected at HERA with ZEUS, with the use of the FNC (see Chapter 5). First the data sample itself is described, including a brief description of the 1993 running period and the criteria used to select the sample presented. Next, leading neutron production in photoproduction is discussed, with emphasis on the shapes of the neutron spectra and the measurement of the $\gamma\pi$ total cross section. Some global event characteristics, such as energy flows are also presented.

6.1   Data sample

The data presented below were all collected during part of the '93 running period of HERA, during which the FNC was installed and integrated into ZEUS — from August 8th to November 5th. The plot of integrated luminosity during this period is shown in Figure 6-1. It is shown as a

Figure 6-1 Integrated luminosity collected by ZEUS, in the period of operational FNC
The integrated luminosity collected by the ZEUS detector is shown as a function of the ZEUS run number. The dashed curve shows all the good ep physics runs, while the solid line shows only the runs for which the rate in the FNC neutron trigger was known, and was under 1000 Hz. This is the sample that was used for the analysis presented here.

function of the ZEUS run number. During this period the total integrated luminosity collected by
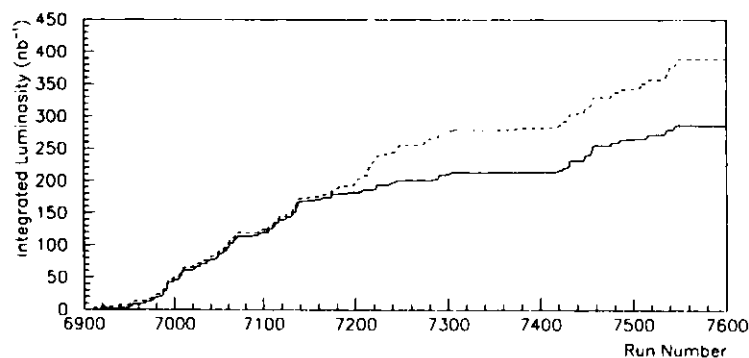
ZEUS (dashed line) was 389 nb[-1]. From this 293 nb[-1] was collected in the runs with good beam conditions (solid line) (see Section 6.1.1). Problems with the HERA beam conditions around the middle of this running period (starting about run 7200) are reflected in this plot in two ways. First, the two curves start diverging at this point, indicating the presence of more runs with an unacceptably high FNC rate (> 1000 Hz). Second, the presence of large flat sections in the curves, indicates a number of runs that have either failed or were not considered good luminosity runs by ZEUS for reasons other than the FNC rate. For the runs considered the mean number of events per μb^{-1} with an FNC energy greater than 100 GeV was 0.032. It was distributed normally with a sigma of 0.007 events/μb^{-1}.

The results presented in this thesis are based on the 293 nb[-1] data sample shown in the solid curve in Figure 6-1.

6.1.1   Rates — overall and accidental

The rate for the FNC trigger signal sent to the GFLT (see Section 5.1.2) was recorded in the data stream during the running period with the ZEUS detector. As can be seen in Figure 6-2 the rate varied greatly from run to run, reaching up to 0.3 MHz. These rate fluctuations are due to different beam conditions. In the same figure the rate distribution for the runs with good beam conditions, as defined by the FNC rate being under 1000 Hz, is shown. Approximately half the runs taken fall into this category, and these are the runs that were considered in this analysis. A clear peak is visible with the most probable value of 150 Hz, with an RMS of about 50 Hz. One possible reason for the high rate deviations is the insertion of other detectors close to the proton beam, such as the target wire for the HERA-B experiment as well as the ZEUS Leading Proton Spectrometer silicon strip detectors which are located close to the FNC and are inserted to within 10 σ of the proton beam.

The average proton beam current was not correlated with the FNC rate, and had a mean value of 11.4 mA with an RMS of 2.9 mA over the whole running period. Taking this, as well as the HERA bunch structure into account, the occupancy of the FNC signal greater that 100 GeV, at the rate of 150 Hz, is

$$\frac{N_{btot}}{N_{bocc}} \cdot \frac{R_{FNC}}{R_{HERA}} = 3.5 \cdot 10^{-5} \qquad (6\text{-}1)$$

where N_{btot} = total number of bunches

        N_{bocc} = number of occupied bunches

        R_{FNC} = rate of the FNC trigger

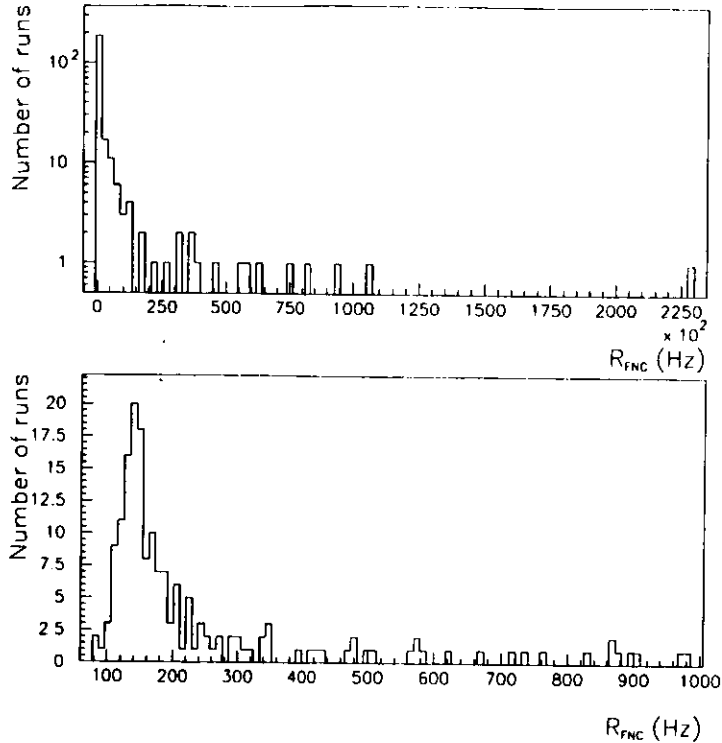 R_{HERA} = HERA crossing rate.

Figure 6-2 Rate of the FNC trigger for the physics runs in the '93 running period
The top plot shows the range of variation of the FNC rate. It went all the way up to 0.2 MHz in one of the runs. the bottom plot shows the FNC rate distribution for the runs with good beam conditions, where the rate was ~150 Hz with the onset of the high rate tail showing at higher frequencies.

This can be used to estimate the background to physics processes from random coincidence with observing a neutron from a beam gas interaction. The background to signal ratio is given by:

$$\frac{background}{signal} = \frac{3.5 \cdot 10^{-5} \cdot N_{all}}{N_{FNC}}, \qquad (6\text{-}2)$$

where N_{all} = total number of events in the desired physics sample and

N_{FNC} = number of the events of this physics type with an FNC signal above 100 GeV before the front counter cut is applied (see next section).

In the case of the tagged photoproduction sample (see Section 6.2.2) this yields the background to signal ratio of $2.8 \cdot 10^{-3}$. In other words one in every 350 events is due to a random coincidence of a leading neutron from a beam-gas event with a valid tagged photoproduction event.

6.1.2   Data selection criteria

The cuts applied to obtain a clean neutron sample are summarized in Table 6-1 and explained in more detail below.

Cuts applied to the data	Removes
400 GeV $< E_{FNC} <$ 1000 GeV [a]	56%
$|\Delta t - <\Delta t>| < 2.5$ ns [b] $|\Sigma t - <\Sigma t>| < 4.5$ ns	6%
$E_{front\ counter} < 150$ [b]	52%

Table 6-1 Selection cuts applied

a. The reduction is with respect to the $E_{FNC} > 100$ GeV
sample, in the selected runs.

b. Here $\Delta t = t_1 \cdot t_2$ and $\Sigma t = t_1 + t_2$, t_1 and t_2 being the times in
the two FNC calorimeter channels. The reduction is with
respect to the sample after the energy window cut is applied.

Figure 6-3 shows the correlation between the times measured in the two calorimeter channels of the FNC. A clear correlation between the two times can be seen as expected for the signal coming from real energy deposits in the calorimeter. Several features should be noticed from this plot. As discussed earlier (Section 4.2.2.2) the time is reconstructed within the window of -64 to 64 ns. This is visible as sharp cutoffs on all four sides of the plot. Also visible is a dense area
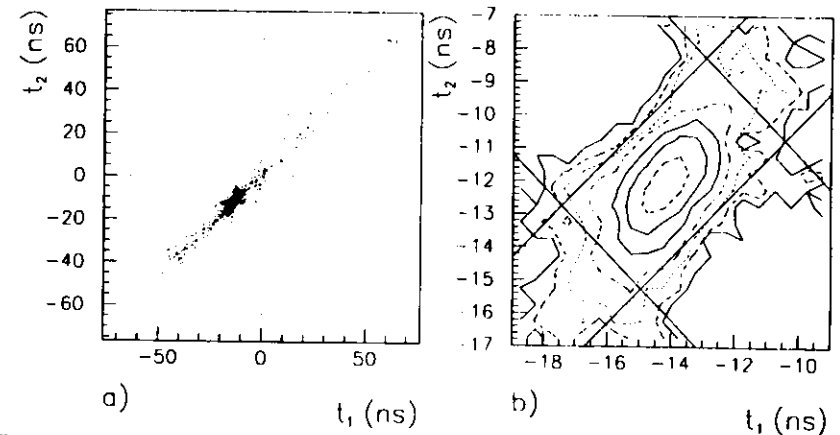
Figure 6-3 Timing distributions in the FNC calorimeter channels
The plot in a) shows that the times in the two FNC calorimeter channels are well correlated, meaning that most of the deposits are due to real energy depositions. The dense spot in the middle corresponds to the events that are in time with the HERA bunches as well. The plot in b) is a logarithmic contour plot of this dense area. The lines indicate the timing cuts used. The cuts are made at the 3σ level on the main peak, cutting out 6% of the events.

around -15 ns, corresponding to the events arriving in time with the HERA clock. The events outside of this area are due to coincidences of beam-gas events from protons in the tails of the beam bunches and the ZEUS trigger. Another source of these events can be pile-up, where two events happen in crossings close enough to each other that the samples from the two events overlap. This can influence the reconstruction of the event time as well as energy. Most of the out of time events are removed when the FNC rate is restricted to under 1000 Hz (as done in Figure 6-3). Before the high rate runs are removed 25% of the events fail these timing criteria. This number is reduced to 6% after only low rate runs and high energy deposits are considered.

To be accepted for the final sample events were required to have both the difference and the sum of the two times within certain windows of their respective means (see Figure 6-3 b). This effectively requires that the two channels fire both at the same time and in time with the beam. The distributions of the timing quantities used for event selection and their run to run variation is shown in Figure 6-4. The cut was made at the 3σ level on the central peak in each case. The position of

Figure 6-4 Variations in the timing of the FNC during the running period
Timing cut was applied to reduce the background from the beam gas events, as well as poorly reconstructed events.

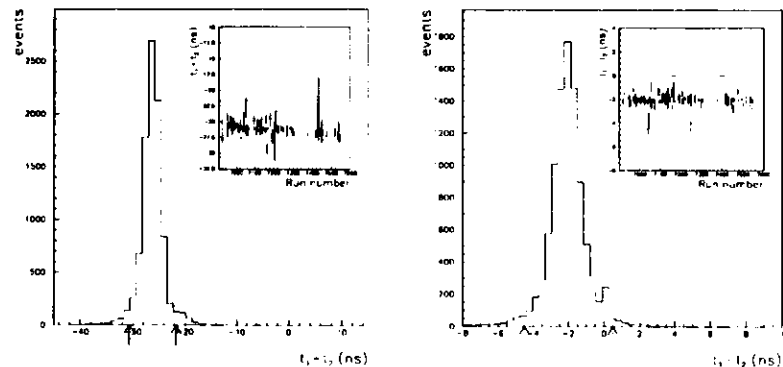the cuts is indicated in the figure by the arrows on the histogram and by the dashed lines in the inserted plots. The spike at $t_1 - t_2 = 0$ is due to events for which the time is reconstructed at ± 64 ns in both channels. These events are out of time by more then 30 ns and are removed by the cut on the sum of the times.

In addition, the energy recorded in the FNC was required to be between 400 GeV and 1000 GeV. This is the energy region in which both the acceptance is best understood and the readout is best behaved. In this region the acceptance rises steadily with energy and the energy is well above the point of the high to low gain switch in the readout (~240 GeV).

Finally, in order to ensure selection of neutral particles, as well as to eliminate preshowering neutrons a cut was made on the deposit in the scintillation counter positioned in front of the calorimeter. The cut was selected so that the signal is below a single minimum ionizing particle (as determined from the cosmic setup described in Section 5.4.1). For a more detailed explanation of this cut see Section 5.4. The cut was placed as close to the one mip peak as possible to increase the statistics in the distributions presented, but still low enough that the contamination from neutrons that interacted in front of the FNC is kept small.

6.1.3 Front counter effects

There are two effects concerning the use of the front counter signal for event selection: the effect of the clean neutrons with the albedo signal greater than one mip and the effect of neutrons which interacted, but have only neutral particles reaching the FNC.

Leading neutrons which reach the FNC without secondary interactions in the inactive material can still cause a signal larger than one mip equivalent in the front counter through backscatter. Such neutrons should be counted as clean neutrons, even though they are vetoed by the energy requirement in the front counter. The number of these events can be estimated by comparing the energy spectrum in the FNC from the neutron runs to the simulated energy spectrum from MOZART, requiring the energy deposit in the front counter to be between 1 and 4 mips. The processes that produce the low energy backscattered particles are not fully simulated in GEANT, and hence the MOZART spectrum in this region is due predominantly to neutrons interacting upstream of the FNC. It can be parametrized with a parabola, and then subtracted as background from the neutron run spectrum to obtain the number of additional events with clean neutrons. The proportions of the background and clean neutron signals was determined in two different ways, providing an estimate of the error on the correction. The first method was to fit the neutron run FNC energy spectrum[1] with a sum of the MOZART background parabola and the parametrization of the clean neutron spectrum. The latter was obtained by parametrizing the FNC spectrum for the events with less than 1 mip energy deposit in the front counter. A typical resulting fit is shown in Figure 6-5. The correction is then calculated as the percentage of the clean neutron events in this region out of the uncorrected event count (i.e., the clean neutron events counted with the 1 mip requirement on the front counter energy). The second method was to arbitrarily normalize the background histogram and find the normalization constant which minimizes the deviation of the correction factor for the five neutron runs. Table 6-2 gives a summary of the numbers obtained with the two methods and for the five neutron runs. The final correction factor is taken to be the average of the results of the fitting method, with the other method providing an estimate of the systematic error. The additive correction is then $(25 \pm 3)\%$.

---

1. in the 1 to 4 mips in the front counter region (i.e., $150 < E_{front\ counter} < 800$ units)
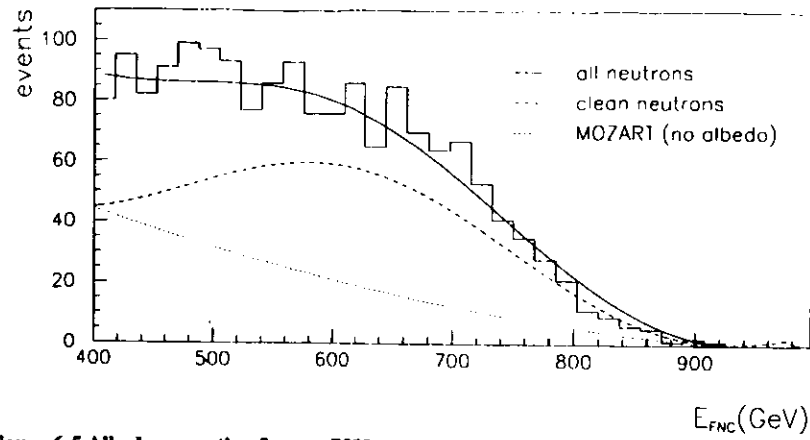
Figure 6-5 Albedo correction for run 7559
The fit to the spectrum (solid line) is a sum of the background from neutrons that interacted upstream (dotted line) and the clean neutron spectrum (dashed line). The dotted line is a parametrization of the equivalent MOZART spectrum, and the dashed line is a parametrization of the data with no signal in the front counter (i.e., tagged clean neutrons).

Run number	Number of Events	Normalized by height	Fitting technique
6392	21694	20.9 %	25.0 %
6905	17716	22.8 %	26.2 %
7120	·8169	23.3 %	24.9 %
7491	20033	22.1 %	25.4 %
7559	16908	22.5 %	24.3 %

Table 6-2 The summary of albedo correction

Some fraction of preshowered neutrons will result in only neutral particles reaching the FNC, and will leave no energy deposit in the front counter. The number of such events can be estimated from MOZART by fitting the ratio of the simulated measured energy to the true generated energy with a gaussian distribution and counting the number of events in the non-gaussian tail. The effect is about 10 % for $E_{FNC} > 200$ GeV, and is reduced to a fraction of a percent for $E_{FNC} > 400$ GeV. Thus, as can be expected such events are concentrated in the lower energy region. Since these events are selected as good events (as long as the energy deposited in the FNC is greater than 400 GeV) they enter the acceptance calculation in the numerator. Hence they are accounted for through the acceptance, and no explicit correction is needed.

6.1.4   The error in event counting

As another check of the correction method presented in the previous section the corrected number of events was obtained as a function of the value of the front counter cut. The sensitivity to this cut indicates the error associated with the counting method. This variation is shown in Figure 6-6. The spread in the corrected number of events is 1% over a 1/4 mip variation in the front
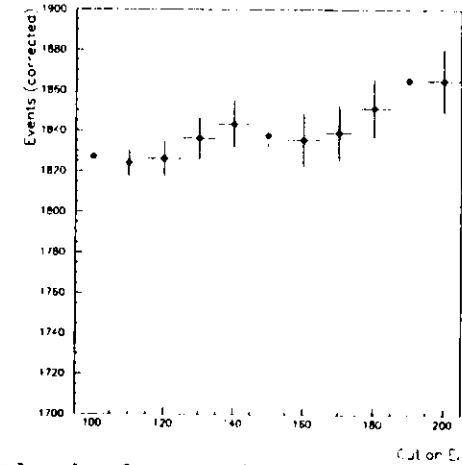
Figure 6-6 Corrected number of events as a function of the front counter cut
The error on the first point shows the statistical error on the counted number of events, scaled by the correction factor. The errors on the subsequent points show the statistical error on the number of events above the baseline defined by the first point. There is a slight rise in the corrected number of events. This spread of 1% is considered as a contribution to the systematic error on the corrected number of events.

counter cut.

The error associated with the albedo corrected number of events is due to a combination of several sources. Varying the timing cut by one sigma changes the number of selected events by ~3%. The albedo correction error is 3% (Section 6.1.3) and the corrected number of events changes by 1% when the cut in the front counter is varied over a reasonable range (between 100 and 200 units). The combined error due to the selection cuts and the albedo correction is taken to be the sum of these components in quadrature, since they should all be independent error sources. The overall error is 4%.

6.2 Neutrons in photoproduction

After the cuts described above a sample of events is left over in the tagged photoproduction sample, triggered by the coincidence of the signal above 5 GeV in the electron tagger of the luminosity detector and the rear calorimeter trigger:

$$(REMC \geq 464 \text{ MeV}) \text{ or } (REMCTH \geq 1250 \text{ MeV}). \qquad (6\text{-}3)$$

See Section 4.3.1 for the definition of these trigger quantities. This will be referred to as the total double tagged sample. In the following sections some of its characteristics are presented and discussed, and the first measurement of the total $\gamma\pi$ cross section is given.

6.2.1 Background

Two kinds of background were accounted for in the analysis of the photoproduction sample. They were both subtracted by statistical methods described in detail in [34]. The procedure is described here briefly.

The e-gas background events are produced when an electron scatters from a residual gas nucleon, with small momentum transfer, so that the scattered electron ends up in the LUMI electron detector, while the rest of the event deposits enough energy in the RCAL to trigger the event. The contribution of this background is estimated by counting the number of triggered events in the electron pilot bunches (see Section 3.2), where all the events must be from this source, since there is no proton beam in these bunches. The obtained number is scaled by the ratio of the total current in these pilot bunches to the total current in the ep bunches. This background source is particularly important in the diffractive subsample, since the gas particle remnant is always boosted in the rear direction, hence leaving a large rapidity gap in the detector, characteristic of the diffractive events (see Section 6.2.4.1). This background is, however, only important in the overall sample (~ 7%), since in the FNC tagged sample the e-gas events would have to be in coincidence with a neutron containing p-gas event, and the rate for that is small (see Section 6.1.1).

The other type of background considered is a random coincidence between a bremsstrahlung event with the electron hitting the LUMI electron tagger and any other type of event that deposits enough energy in RCAL to trigger the main calorimeter. The size of this background can be measured by counting bremsstrahlung events (recognized by a coincidence of LUMI electron and LUMI gamma signals whose energies add up to the incident electron beam energy) and scaling that number according to the information provided in the environmental records[1] by the LUMI detector, to account also for the bremsstrahlung events in which the radiated photon is not seen in the

---

1. In certain regular intervals these records are inserted into the data stream, containing the information that needs to be updated relatively frequently, yet not on an event by event basis. They contain, for example, beam currents, rates, luminosity information etc.

LUMI gamma catcher. The contribution from this background is about 6.5% in the overall sample and 3% in the double tagged sample.

All the distributions presented are corrected for the two types of backgrounds described above. The correction was done by negative weighting of the recognized background events (i.e., the electron pilot bunch events and the bremsstrahlung events tagged by both LUMIE and LUMIG) by the appropriate ratios in order to account for the unrecognized background events. It is assumed that all of the background has the same distribution as the recognized one. This assumption is valid since: i) the presence of the proton beam does not change the characteristics of the e-gas events, and ii) for the bremsstrahlung coincidence events all the distributions (except for those from the LUMI detectors themselves) are coming from a random selection of events, regardless of whether the radiated photon is observed or not.

6.2.2 Fraction of neutrons

The numbers of observed events with and without a leading neutron, with energy greater than 400 GeV, are shown in Table 6-3. The last column shows the fraction of leading neutron

Tagged Photoproduction sample	tagged γp $\times 10^5$	tagged γp with FNC	fraction
all events	4.07	1469	15 ± 3 %
events with $\eta_{max} > 2$	3.44	1279	15 ± 3 %
events with $\eta_{max} < 2$	0.626	190	12 ± 2 %

Table 6-3 Numbers of events with FNC signal in tagged photoproduction

The numbers shown are from the sample described in Section 6.1.2, before the albedo correction. The background subtraction is discussed in Section 6.2.1. The numbers for the tagged γp subsamples in different regions of η_{max} are discussed in the text. The fractions given in the final column are corrected for the FNC acceptance with the value given in Section 5.3 and also for the albedo correction discussed in Section 6.1.3.

events in photoproduction after correcting for the acceptance of the FNC and after background subtraction and the albedo correction. The sample is also divided into $\eta_{max} > 2$ and $\eta_{max} < 2$ subsamples (for explanation of η_{max} see Section 6.2.4.1).

The fraction of events with a leading neutron is around 15% in all three cases. The error on this fraction is mainly from the uncertainty in the number of events passing the data selection cuts of Table 6-1 combined with the albedo correction (4% from Section 6.1.4) and the error on the FNC acceptance (20% from Section 5.3). The prediction for the fraction of photoproduction events containing a leading neutron is given in [31] to be 15% and should be reduced by about 1.5% to

13.5% if only neutrons above 400 GeV are considered. This number is based on theory and results of previous experiments and assumes OPE dominance. It is in good agreement with the ZEUS measurement.

6.2.3 Inclusive neutron spectrum

The inclusive leading neutron energy spectrum for the tagged photoproduction sample, after the background subtraction, is shown in Figure 6-7. Also shown in this plot is the spectrum ex-
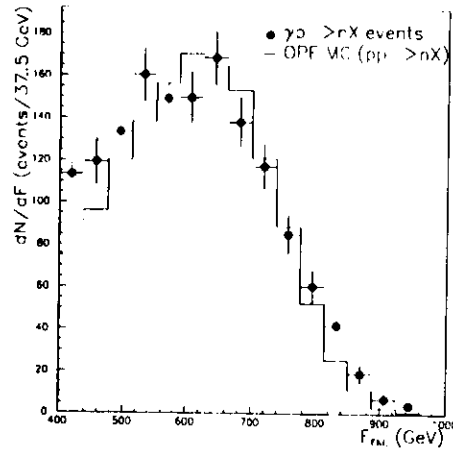

Figure 6-7 The inclusive neutron spectrum in photoproduction
The data points show the inclusive neutron spectrum in the double tagged events where both the leading electron and the leading neutron are observed. The data are not corrected for acceptance. The hadron-hadron OPE model (solid histogram) describes the data well, in support of factorization.

pected from the pp $\rightarrow$ nX reaction assuming the dominance of OPE. The agreement with the data is good. This model is expected to agree with the data if the photon behaves as a hadron and the $\gamma\pi$ cross section varies slowly with energy in the applicable range. In this case the shape of the spectrum is directly related to the pion flux factor in the proton $f_{\pi/p}$ (Eqn. (2-24)).

6.2.4 Event characteristics comparisons with and without leading neutrons

Once the sample of events with a leading neutron is selected its characteristic distributions can be studied and compared to those of the overall tagged photoproduction sample. Such comparisons for the calorimeter subcomponent energy flows, as well as the η_{max} distribution are shown in this section. The charged particle p_T spectrum is discussed in more detail in Chapter 7.

6.2.4.1 η_{max} distribution

In diffractive (i.e., Pomeron exchange) events a clear separation in rapidity[1] space is expected between the particles resulting from the diffracted photon and the leading baryon system. This results in a rapidity interval with no activity in the detector — the "rapidity gap". The size of this rapidity gap is uniformly distributed for diffractive events. In other words, the expected number of diffractive events with a given rapidity gap is independant of the size of the gap. In non-diffractive events the produced particles uniformly fill the rapidity space. The probability of observing a rapidity gap in such events is "exponentially suppressed", meaning that it drops off exponentially with the size of the rapidity gap. This leads to the conclusion that a majority of the events with a large rapidity gap are due to diffractive processes. Selecting events with a large rapidity gap can thus be used to obtain a sample of mostly diffractive events.

When diffractive processes are being considered one of the questions is how to observe and quantize this rapidity gap. For elastic and diffractive events the remnant of the proton is collimated enough so that it does not hit the main detector. In this case the pseudorapidity η_{max} of the most forward going cluster observed in the calorimeter[2] is a good representation of how far from the FCAL beampipe there is no activity in the detector, corresponding to no particle production. Thus η_{max} is related to the size of the rapidity gap between the proton remnant and the current jet and/or the photon remnant.

The η_{max} distribution shown in Figure 6-8 shows several features. The physical edges of the calorimeter are at $\eta = -3.4$ (RCAL) and $\eta = 3.8$ (FCAL). Due to these limits the η_{max} plot falls off rapidly at both ends. The values of $\eta_{max} < -3.4$ and $\eta_{max} > 3.8$ result when the energy is deposited around the F/RCAL beampipes and the clustering algorithm combines these deposits into a single object, whose position (calculated from the energy weighted cell positions) falls within the beampipe hole. Well away from the FCAL edge an exponential drop off is observed, as expected for the exponentially surpressed non-diffractive events. There is, however, another peak at low values of η_{max}, due to the diffractive like processes, indicating a flatly distributed rapidity gap. These events can be interpreted as arising from the Pomeron exchange process.

Another feature at the smallest values of η_{max} is the elastic peak, seen at $\eta_{max} \sim -3.1$. It is due to elastic and diffractive vector meson production where nothing is observed in the detector except for the decay products of the vector meson (most often the two pions from the ρ decay). These decay products are close to the RCAL beam hole, hence yielding a negative η_{max} close to -3.1.

---

1. for definition of rapidity see Section 2.3.1
2. the energy of the cluster is required to be greater than 400 MeV, to avoid contributions from the noise in the calorimeter
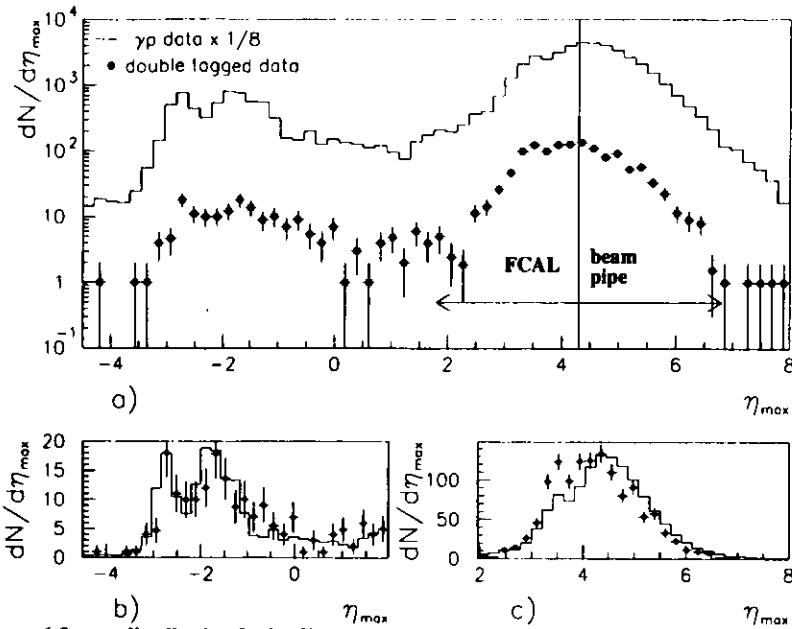
Figure 6-8 η_{max} **distribution for leading neutron events in photoproduction**
The data with an FNC tag ($\gamma p \to nX$) are compared to the photoproduction data ($\gamma p \to X$) in a).
The two regions, $\eta_{max} < 2$ and $\eta_{max} > 2$ are compared separately in b) and c) respectively, normalizing each by area. Note that the plots in b) and c) are on a linear scale, while the plot in a) is on a logarithmic scale.

It is interesting to compare the double tagged sample to the tagged photoproduction sample. There is a good agreement between them in the low η_{max} region (Figure 6-8 b), while on the non-diffractive peak (Figure 6-8 c) there is an indication of a difference, although more statistics are needed to make a definite statement. A possible reason for such behavior is that in the case of diffractive events (low η_{max}) the system seen in the main detector is the diffracted photon and if factorization holds, the characteristics of that system should be independent of the process at the baryon vertex. Therefore, regardless of whether a neutron is produced or not, the process is effectively a Pomeron photon collision. At higher η_{max} it is predominantly determined by the baryon system remnant, and hence is greatly influenced by the process at the baryon vertex itself. The distribution for the events where a neutron is produced (mostly through one pion exchange) can be expected to be different from the proton dissociating into any collection of hadrons.

The neutron spectrum is also shown for the $\eta_{max} < 2$ and $\eta_{max} > 2$ samples separately (Figure 6-9). The shapes of the spectra differ at the 90% confidence level, according to the Kol-

mogorov test, which is a test for distribution comparison sensitive to the shape of the distributions.
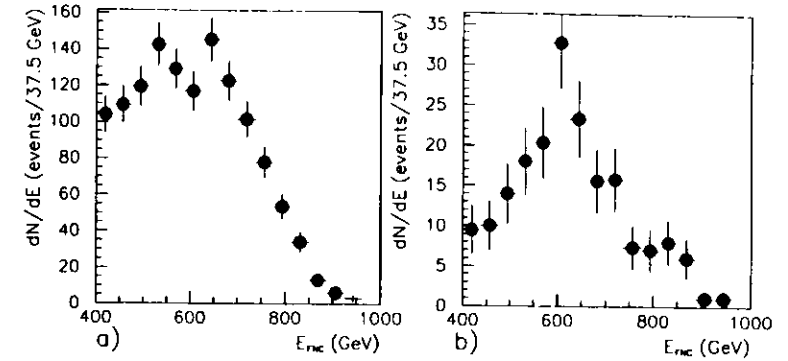

Figure 6-9 Neutron energy spectrum for the non-diffractive and the diffractive subsamples in photoproduction
The spectra in the two regions of η_{max} seem to have different shapes, possibly due to the different composition of the two subsamples. The fraction of directly produced neutrons is larger in the plot in a), leading to a distribution similar to the OPE spectrum. The larger fraction of the neutrons from the decay of the excited nucleons might be the reason for a more peaked spectrum in b).

This difference can be expected if the two samples are predominantly due to different processes. The $\eta_{max} > 2$ events are dominated by non-diffractive OPE, while some fraction of the $\eta_{max} < 2$ events are likely due to diffractive production of N^*s, where the leading neutron is one of its decay products. The kinematic difference of the production mechanisms can be responsible for the different neutron spectra observed in the two subsamples.

6.2.4.2 Energy distributions (F/RCAL)

Further comparison of the double tagged and overall photoproduction samples can be made by examining the energy spectra in the rear and forward calorimeters, which are presented in Figure 6-10. For the RCAL (Figure 6-10 a) and b)) the following observations can be made:

- The spectra for the double tagged and the overall samples exhibit a similar shape, except for the first two bins in the $\eta_{max} < 2$ sample where there seem to be significantly more double tagged events. This discrepancy is not understood.

- The energy distribution in RCAL has a similar shape for the $\eta_{max} > 2$ and the $\eta_{max} < 2$ samples.

This is expected from the factorization argument presented in the previous section.
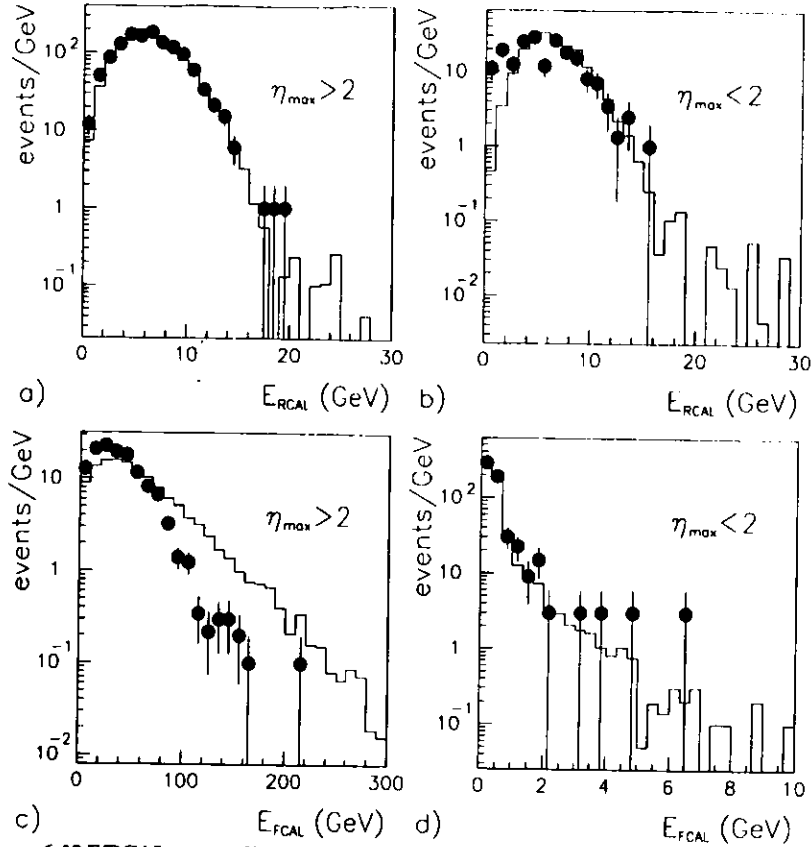
Figure 6-10 F/RCAL energy distributions for events with a leading neutron compared to all tagged photoproduction events

The plots on the left are for the $\eta_{max} > 2$ subsample, while the plots on the right are for the $\eta_{max} < 2$ events. In all plots the points show the double tagged data, while the histogram is all of photoproduction. In each plot the photoproduction data were normalized to the area of the neutron data.

On the other hand the following observations can be made about the FCAL energy distributions (Figure 6-10 c) and d)):

* they are different for $\eta_{max} > 2$ and $\eta_{max} < 2$ for both the double tagged and the overall sample;

* for the $\eta_{max} < 2$ sample the distribution for the double tagged sample has the same shape as that for the overall tagged photoproduction, while the shapes differ for the $\eta_{max} > 2$ sample.

These characteristics can also be explained in terms of predominant contributing processes. The expected forward energy distribution depends greatly on the forward state produced. As mentioned earlier, in a diffractive collision the forward state will largely exit the detector through the beam-pipe opening, thus escaping detection. Hence the energy deposited in the FCAL in this case is from the forward moving fragments of the dissociated photon and is small (typically ≤ 1 GeV). In non-diffractive events, where parts of the proton remnant hit the detector the most probable energy in FCAL is non-zero, with the distribution having a high energy tail up to over 100 GeV. Thus the different features of the $\eta_{max} < 2$ (diffractive enriched) and $\eta_{max} > 2$ (predominantly non-diffractive) samples are expected in terms of the contributing processes.

Furthermore, factorization justifies the similarity of the $\eta_{max} < 2$ spectra for the double tagged sample and overall tagged photoproduction (Figure 6-10 d), since in both cases it is the dissociated photon that is observed. The difference in the $\eta_{max} > 2$ samples is due to the difference in the effective beam energy in the two cases. The events with neutrons can be viewed as $\gamma\pi$ collisions of a 200 GeV pion on a 10 GeV photon, compared with the 820 GeV proton on the same energy photon. Clearly the fragments of the latter will, typically, leave a larger energy deposit than the former. Therefore the FCAL spectrum for the neutron sample peaks at a lower value and the tail does not extend as far (Figure 6-10 c).

6.2.5   The $\gamma\pi$ scattering cross section

As explained in Section 2.5.1 $\sigma_{\gamma\pi}$ can be evaluated from the ep cross section for leading neutron production. The latter is measured directly by counting the number N of events double tagged by the LUMIE and the FNC, corrected for the detector and trigger acceptances:

$$\sigma_{ep \rightarrow enX} = \left(\frac{N}{A_{FNC} A_{LUMI} A_{CAL}}\right) \frac{1}{\mathcal{L}}. \qquad (6\text{-}4)$$

Here $\mathcal{L}$ is the corresponding integrated luminosity measured as described in Section 4.2.3. The acceptances of the three detectors involved (FNC, LUMI, and CAL) are assumed to be independent, so that the overall acceptance factorizes into a product of the three individual acceptances (A_{FNC}, A_{LUMI}, and A_{CAL}). Since only a narrow window of electron energies is considered, with negligible transverse momentum, the properties of the emitted photon do not change between collisions. A_{LUMI} then depends only on the detection of the electron scattered at a low angle, and not on the type of interaction that the photon undergoes with the proton. This implies that the acceptance of the LUMIE detector is uncorrelated with both the RCAL and the FNC acceptances. Furthermore, since the events were triggered on the RCAL energy, A_{CAL} and A_{FNC} are independent as long as the particle flow in the RCAL direction is independent of whether a leading neutron is produced or not. Figure 6-11 compares the energy and the polar angle distributions of particles produced in the
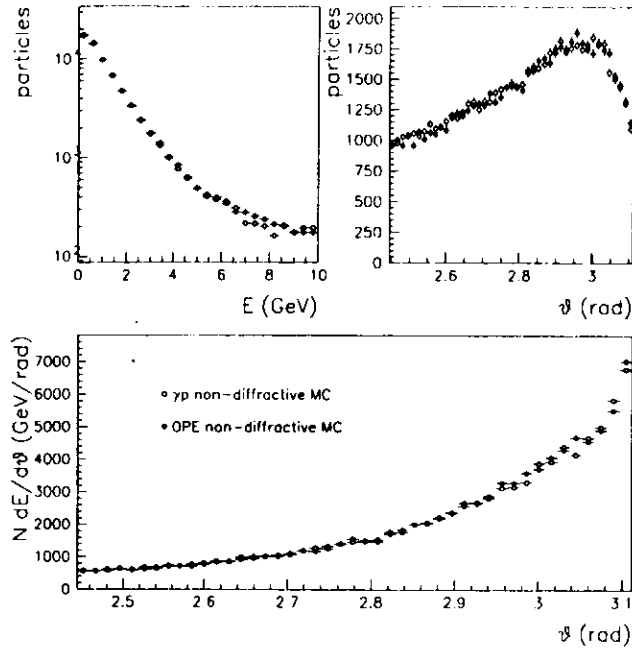
Figure 6-11 The rear direction particle flow in γp and OPE

Generator level distributions of energy (top left) and polar angle (top right) of particles in the rear direction for OPE events (full circles) and for γp interactions (open circles) are compared. The distributions are from non-diffractive Monte Carlo samples. The bottom plot shows the energy weighted polar angle distribution. The good agreement in all three cases indicates independence of the RCAL signal on the presence of a forward neutron, and hence warrants the factorization of the FNC and CAL acceptances.

RCAL direction for two Monte Carlo samples: non-diffractive γp events and non-diffractive OPE events. The good agreement not only confirms the independence of the CAL and the FNC acceptances, but also shows that the CAL acceptance calculated for γp interactions can also be used for determination of $\sigma_{\gamma\pi}$.

Since this measurement relies on the assumption that the neutron events are due predominantly to OPE the acceptance of the FNC to be used is exactly the one evaluated in Section 5.3: $A_{FNC} = 0.031 \pm 0.001 \pm 0.005$. The LUMI acceptance is the same as the one evaluated for the γp analysis [52]: $A_{LUMI} = 0.75 \pm 0.02$. The CAL acceptance was also obtained from the γp analysis and is taken to be $A_{CAL} = 0.76 \pm 0.08$ (also from [52]), where the error was increased to 10% from ~5% to account for possible differences (e.g., slight variations in the fractions of elastic, diffractive

and non-diffractive events can change the acceptance accordingly). The errors on the LUMI acceptance, the CAL acceptance and the luminosity measurement are all systematic errors only.

Smaller corrections, such as trigger inefficiency and radiative corrections are ignored in this estimate, since they are much smaller than some of the other errors involved. From [52] it can be seen that in the case of photoproduction these corrections are smaller than 10%.

The only remaining number to be determined is the number of double tagged events within the LUMI energy window, $15.2 < E_{LUMIE} < 18.2$ GeV (corresponding to $<E_\gamma> = 10$ GeV) and with clean neutrons with $E_{FNC} > 400$ GeV (corresponding to $<E_\pi> = 205$ GeV). Counting the accepted events in the data sample described in Section 6.1, including the corrections for the coincidence background (see Section 6.2.1) and the albedo correction (see Section 6.1.3) the number is $N = 642 \pm 25 \pm 26$ events. The first error is statistical, the second is systematic (see Section 6.1.4). The only difference between this number and the number in the first row of Table 6-3 is the LUMIE energy requirement.

There is one more correction to be considered: the background from the diffractive processes. The question here is: how big is the contribution from Pomeron exchange to the leading neutron production. This can be estimated by considering the $\eta_{max} < 2$ sample. There are two contributions to these events: the events with secondary neutrons coming from the decay of diffractively produced excited baryons and the diffractive OPE events, where the Pomeron is exchanged between the γ and the π. The first class is what needs to be subtracted for the cross section measurement, while the second class should be counted in the signal. Furthermore, there is a contribution from the first class of event to the $\eta_{max} > 2$ region as well, which should also be subtracted out. There is no theoretical prediction of what the fractions of the two processes should be. As a rough estimate it can be arbitrarily assumed that half the $\eta_{max} < 2$ events are due to γp diffraction and the other half are due to γπ diffraction. Further assuming a flat η_{max} distribution for diffractive events, and noting that the η_{max} intervals covered by ZEUS are approximately equal in the $\eta_{max} < 2$ and $\eta_{max} > 2$ regions the diffractive background can be estimated to be 14 ± 10 % including the $\eta_{max} > 2$ region. The larger error takes into account the assumption of the arbitrary fractional contributions of the two processes.

The final number of events used for the cross section measurement is then:

$$N = (642 \pm 25 \pm 26) - (90 \pm 9 \pm 64) = 552 \pm 23 \pm 69 \qquad (6\text{-}5)$$

Substituting the final numbers in Eqn. (6-4) gives:

$$\sigma_{ep \to enX} = \left(\frac{552 \pm 23 \pm 69}{(0.75 \pm 0.02) \cdot (0.031 \pm 0.001 \pm 0.005) \cdot (0.76 \pm 0.08)} \right) \frac{1}{(293 \pm 15)} \text{ nb} \qquad (6\text{-}6)$$

$$\Rightarrow \quad \sigma_{ep \to enX} = (107 \pm 6 \pm 25) \text{ nb}. \qquad (6\text{-}7)$$

The flux factors are obtained by integrating the fluxes as indicated in Eqn. (2-30) for the photon and the pion fluxes respectively. The integration is performed over the experimentally determined range. The photon flux is the same as for the ep analysis [52] and uses: Q^2_{min} as given in Eqn. (2-28), $Q^2_{max} = 0.02$ GeV^2 and y_{min} and y_{max} as determined from the W range of 167 to 194 GeV selected by the cut on the LUMIE energy, yielding $F_{\gamma e} = 0.005818$. For the pion flux the flux factor was integrated numerically using: $t < 1$ GeV^2 and $z > 0.51$, yielding $F_{\pi/p} = 0.2 \pm 0.04$. The large error on the second flux comes from the uncertainty in the exact t cutoff, due to the irregular geometric acceptance of the FNC, as well as the theoretical flux uncertainty. The value of $G^2_{n\pi p}/4\pi = 30$ was used for the coupling constant, as determined from low energy data [53]. The error on this coupling constant is less than 5%.

The $\gamma\pi$ cross section at the center of mass energy of 90 GeV is then:

$$\sigma_{\gamma\pi} = \frac{107}{0.005818 \cdot 0.2} \approx (92 \pm 5 \pm 28) \ \mu b. \tag{6-8}$$

An interpolation between $\sigma_{\gamma p}$ measurement at HERA ($<W> = 180$ GeV) [52] and at the fixed target experiments ($<W> \approx 18$ GeV) [11] gives $\sigma_{\gamma p}$ (90 GeV) $\approx 145 \pm 15$ μb. From the simple argument based on the number of available valence quarks in the proton (three) and the pion (two) one may expect the $\gamma\pi$ cross section to be of the order of 2/3 of the γp cross section. This does hold in the case of high energy πp and pp collisions: $\sigma_{\pi p} \approx 23$ mb is approximately 2/3 of $\sigma_{pp} \approx 40$ mb at $p_{beam} = 100$ GeV [49]. The ZEUS result is certainly consistent with this simple hypothesis. A stronger conclusion is unwarranted given the large errors.

6.2.6 Diffractive background to elastic ρ production

The FNC tagged events can also be used to make an estimate of the diffractive contribution to the observed elastic production of ρ mesons in untagged photoproduction. Clearly, the ρ events that have a neutron in the FNC are non-elastic events. Hence, by counting such events one obtains a lower limit on the non-elastic contribution to the "elastic looking" events (i e , events with just the two tracks from the ρ decay observed in the main detector) The cuts used were the standard cuts used in the ZEUS ρ analysis [54]:

* -40 cm $< z_{vtx} <$ 40 cm – eliminates beam gas events originating too far away from the interaction point;

* two opposite charge tracks — ensures the required event topology;

* $E_{FCAL} < 2$ GeV — eliminates non-elastic events in which the proton remnant deposits energy in the FCAL close to the beampipe and outside the CTD acceptance;

* $E_{CAL} - E_{CTD} < 3$ GeV — ensures that there are no additional neutral particles in the event (e.g., γ's or π_0's).

In the above z_{vtx} is the z position of the event vertex, E_{FCAL} is the energy in the forward calorimeter, E_{CAL} is the total calorimeter energy, and E_{CTD} is the sum of the momenta of the tracks reconstructed in the CTD.

Figure 6-12 shows the plot of the invariant mass of the two tracks for the events with and
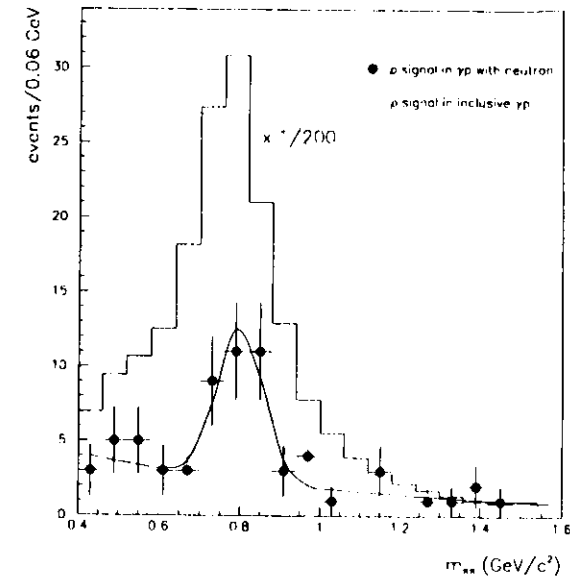

Figure 6-12 Rhos with and without the FNC
The invariant mass distribution of the two observed pions for the elastic ρ events, in which all that is seen in the main detector are these two pions. The points are the events that have a large energy deposited in the FNC, while the solid histogram is for all the photoproduction events. Note that the solid histogram has been scaled down by 200.

without a leading neutron. The simple fit to a gaussian with an exponential background gives the number of events observed in the '93 running period to be 29 ± 11 (after the albedo correction). The error is statistical only.

The FNC acceptance for the ρ events was calculated using a diffractive ρ Monte Carlo sample at the generator level to obtain the energy distribution of the leading neutrons produced in such events. The energy spectra for both leading neutrons and leading protons are shown in Figure 6-13. The OPE events (Section 5.3.2) were used to produce a two dimensional acceptance as a function of energy and angle. This plot was then used to reweight the diffractive ρ Monte Carlo sample. By counting the number of events that would be accepted by the FNC and dividing by the total number of generated events an overall acceptance for the ρ events was found to be $(0.4 \pm 0.06 \pm 0.07)\%$. The first error is from the Monte Carlo statistics and the second is the systematic error, assuming
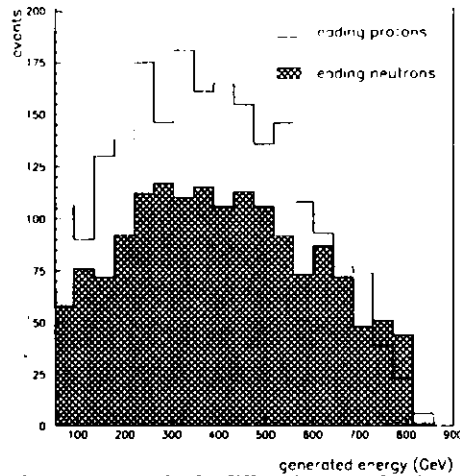
Figure 6-13 The leading baryon spectra in the diffractive ρ production
The proton and neutron spectra before acceptance correction are shown separately. The neutron spectrum above 400 GeV is different from the OPE spectrum. The peak in the spectrum lies below 400 GeV, leaving a monotonically decreasing spectrum in the high energy region. The acceptance was reweighted to this neutron spectrum.

it is the same as for the OPE events. This correction takes into account the events in which no leading neutron is produced, as well as the events with leading neutrons with energy lower than 400 GeV.

The diffractive contribution to the elastic ρ sample is then estimated as the fraction of events with a leading neutron divided by the above correction out of the full sample of elastic ρ events. This comes out to be $(26 \pm 11 \pm 5)\%$ which is in rough agreement with the estimate given in the ZEUS paper on ρ production of $(11 \pm 1 \pm 6)\%$ [54]. This latter value was obtained by fitting the observed FCAL spectrum for the ρ sample with a mixture of two Monte Carlo event samples simulating elastic and proton diffractive ρ production.

7 Inclusive p_T distributions

The inclusive p_T distributions of charged particles in photoproduction are presented in this chapter. Three different event samples are considered: the non-diffractive sample ($\eta_{max} > 2$) and the diffractive sample ($-2 < \eta_{max} < 2$) within two ranges of the diffractive mass M_x (see Section 2.2.1 for definition) with $<M_x> = 5$ GeV and $<M_x> = 10$ GeV. The distribution is also shown for the non-diffractive events that have a leading neutron with energy greater than 400 GeV.

First the trigger and data selection criteria are described, followed by an explanation of the method used to obtain the correction functions from the reconstructed tracks observed in the detector to the true distribution for the charged particles. Finally the results are presented and discussed.

7.1 Data selection

Tagged photoproduction data from the '93 running period are used, triggered by the coincidence of the signal in the LUMIE detector being above 5 GeV and some energy being deposited in the main calorimeter. More specifically, the CAL requirement was:

$$(REMC \geq 464 \text{ MeV}) \text{ or } (REMCTH \geq 1250 \text{ MeV}) \text{ or } (BEMC \geq 3400 \text{ MeV}), \qquad (7\text{-}1)$$

where $REMC$, $REMCTH$ and $BEMC$ are trigger quantities described in Section 4.3.1. The first two CAL conditions were implemented at the GFLT in coincidence with the LUMIE trigger, producing the nominal tagged soft photoproduction sample used in the analysis presented in the previous chapter. Events satisfying the last condition were recovered from the high E_T LUMIE trigger branch. It was checked in the Monte Carlo sample that such events have high acceptance through the high E_T filter as well. For most (over 99%) of the events passing this $BEMC$ cut the E_T in the Monte Carlo was well above the trigger cut of 8 GeV.

To restrict the measurement to a narrow range of the γp center of mass energy W a window on the tagged electron energy, $15.2 < E_{LUMIE} < 18.2$ GeV, was imposed. This also selects the region where the acceptance of the LUMIE detector is most uniform. Equivalently, this measurement is made for $<W> = 180$ GeV. Background reducing cuts used were:

- the vertex position cut: $-35 < z_{vtx} < 25$ cm, assuring that the vertex is within 3σ of the nominal position;

- transverse momentum balance cut: $p_T / \sqrt{E_T} < 2$ GeV$^{1/2}$, removing a lot of the cosmic ray background.

The three different samples were selected based on the cut on η_{max} (see Section 6.2.4.1 for definition) and M_x, as calculated by the empirical formula[1] given below:

$$M_x = \sqrt{(\sum E_i + \sum p_{z_i}) \cdot 2.9 \cdot (26.7 - E_{LUMIE})} + 1 \; (GeV), \qquad (7\text{-}2)$$

where the sum is over the energy deposits in the calorimeter (as defined by a clustering algorithm) with energy above 160 MeV. For the non-diffractive bin all events with $\eta_{max} > 2$ are considered, leaving a contamination from diffractive events of about 5%. For the diffractive subsamples, apart from the mass range cut, $-2 < \eta_{max} < 2$ is also required. The upper bound restricts the sample to elastic or photon diffractive events (from Monte Carlo studies ~96% of events with $\eta_{max} < 2$ are due to these processes), while the lower bound reduces the contribution from elastic vector meson production, thus leaving a relatively pure sample of photon diffractive events. These are considered in two different diffractive mass ranges, namely $4 < M_x < 7$ GeV, and $8 < M_x < 13$ GeV.

For each selected event only tracks passing the following quality cuts enter the distribution:

- only the tracks used in the determination of the event vertex are used;

- the momentum of each track is required to be greater than 0.3 GeV, since otherwise the track may spiral within the CTD, leaving hits which possibly give rise to more than one reconstructed track;

- tracks are required to have reached at least the 5th superlayer of the CTD, thus selecting reliably long tracks; and

- only tracks within the η bin of $-1.2 < \eta < 1.4$, where the CTD acceptance is well away from the non-uniform edge regions, are used. The asymmetry in this region is due to the displacement of the vertex from $z = 0$ to $z = -5$cm.

7.2 Correction function calculation

The distribution of reconstructed tracks must be corrected to give the actual distribution for the charged particles produced. For this a correction function was calculated from the Monte Carlo generated events simulating the event sample being considered. A mixture of generators was used to cover the range of processes contributing to the data sample. Table 7-1 shows the list of generators, the corresponding physics process, and the percentage assigned to each process. The percentages were chosen to correspond to the cross sections published by ZEUS [55]. The Monte Carlo generated events were passed through the detector simulation and event reconstruction programs.

---

1. obtained by optimizing M_x reconstruction in the required region for the Monte Carlo events

Monte Carlo Program	Process	Percentage
PYTHIA	elastic	12%
NikZak	photon diffractive	9%
HERWIG	hard resolved	10%
HERWIG	hard direct	3%
PYTHIA	proton diffractive	9%
PYTHIA	double diffractive	4%
PYTHIA	non-diffractive	51%

Table 7-1 Monte Carlo generators used for simulation of tagged photoproduction data

The correction function is determined as the ratio of two distributions: i) the true charged particle distribution resulting from the physics generator quantities for each Monte Carlo sample, and ii) the Monte Carlo equivalent of the raw data distribution obtained after passing the events through the detector simulation and event reconstruction. Since the Monte Carlo sample used reproduces the data reasonably well (see Figure 7-1), multiplying the track distribution from the data
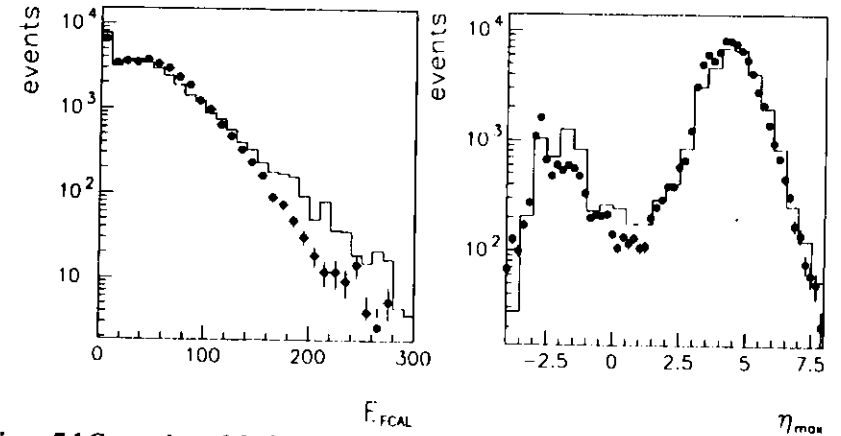

Figure 7-1 Comparison of the Monte Carlo sample and data
The solid histograms are the photoproduction data and the filled circles are the mixture of the Monte Carlo samples described in the text. For the FCAL energy and the η_{max} distributions, shown here, the Monte Carlo describes the data reasonably well.

by this correction factor should yield the true number of charged particles produced in the observed ep interactions.

Care has to be taken in computing the correction factor, when combining the Monte Carlo samples for different processes, since the number of events in each sample did not reflect the ratios of the contributions from the processes to the total cross section. Hence, all the samples were first

normalized and then combined using the contributing fractions according to cross sections for individual processes. Finally, the distributions had to be normalized to the "observed" number of events, corresponding to the sample size used. The final correction functions for the three bins are shown in Figure 7-2. The fact that the correction functions are reasonably flat and close to one
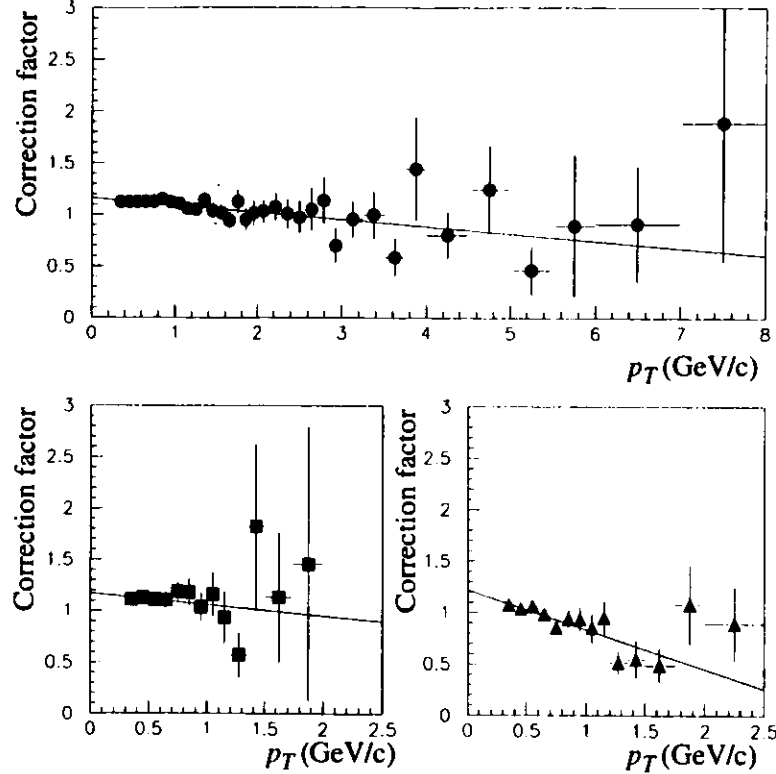

Figure 7-2 The correction functions for charged particle p_T distributions

The three plots correspond to the three subsamples considered. The top plot is for the non-diffractive events. The bottom plots are for the diffractive events: the left plot is for the $<M_X> = 5$ GeV, and the right one is for $<M_X> = 10$ GeV.

show that the reconstructed tracks indeed closely represent the charged particles produced in the interactions. Straight line fits (also shown) were used, in order to average the effect of poor MC statistics.

7.3 Systematic effects

Although not as a part of this thesis the systematic effects were evaluated resulting in the systematic uncertainties of 15% for the non-diffractive sample, 15% for the $<M_x> = 5$ GeV, and 9% for the $<M_x> = 10$ GeV sample, independent of p_T. The effects included in that study were tracking efficiency and reconstruction, trigger effects, and the dependance of the correction functions on the Monte Carlo models used and the fractions used in mixing the different processes. For details see [56].

7.4 p_T distributions and slopes

The ZEUS data, after background subtraction and application of the correction function, is shown in Figure 7-3. The distribution shown is the double differential cross section as a function of p_T, normalized to the total cross section σ_{tot}.

$$\frac{1}{\sigma_{tot}} \frac{d^2\sigma}{dp_T^2 d\eta}. \qquad (7\text{-}3)$$

In other words it shows the number of charged particles per event produced at a given p_T per unit of p_T^2 and per unit of pseudorapidity η. For the non-diffractive data the distribution is shown up to 8 GeV, while for the diffractive samples and the neutron sample they are shown only up to 2.5 GeV, due to the limited statistics at high p_T. The width of the bins varies with p_T to decrease the statistical errors in the higher bins, since the number of particles produced decreases rapidly as p_T increases.

All the spectra show an exponential fall off in the low p_T region, expected from the soft, longitudinal phase space interactions [18]. The non-diffractive sample shows a nonexponential tail, corresponding to hard interactions, from collisions of the photon or one of the virtual partons in the photon with individual parton constituents of the proton (see Section 2.2.1).

Also shown in the figure are exponential fits to the data in the low p_T region $(0.3 < p_T < 1.2$ GeV) to the function:

$$\frac{1}{\sigma_{tot}} \frac{d^2\sigma}{dp_T^2 d\eta} = A e^{-bp_T}. \qquad (7\text{-}4)$$

The parameter b for the different ZEUS samples is compared to the value from other experiments in Figure 7-4. The values of b for the diffractive events are entered at the value of $\sqrt{s}$ corresponding to the mean diffracting mass for that sample, since that is the center of mass energy of the photon-pomeron system. From this figure it can be seen that the ZEUS values agree well with the other hadronic values.
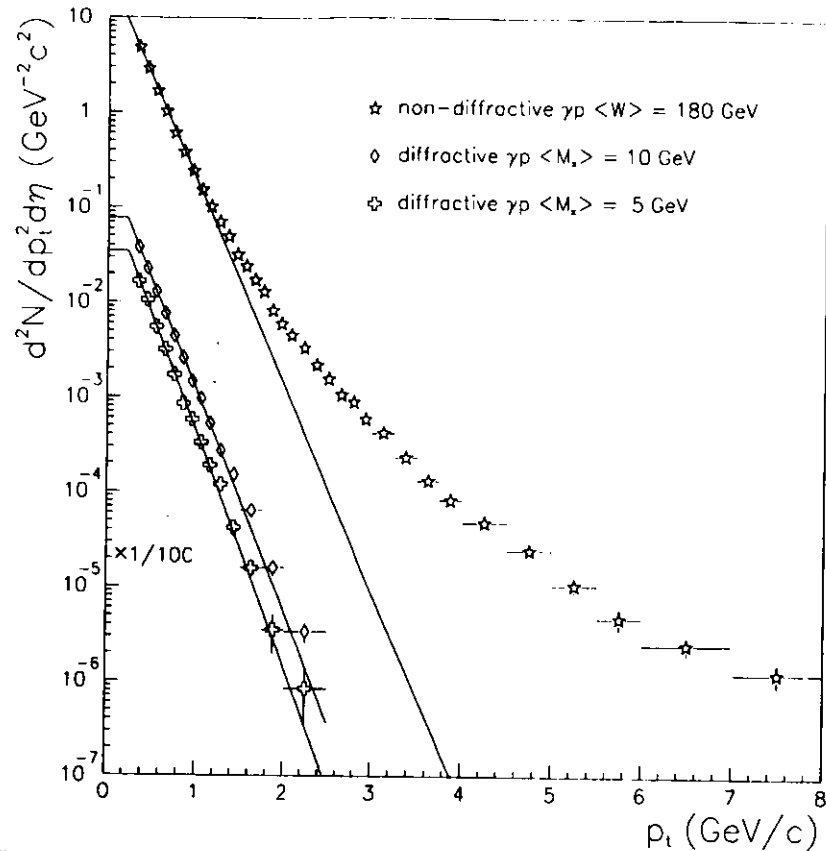
Figure 7-3 Inclusive charged particle p_T spectra in photoproduction

The data are presented for the pseudorapidity interval $-1.2 < \eta < 1.4$. The lines are exponential fits to the data in the low p_T region. The excess of events at high p_T in the non-diffractive sample indicates the presence of hard interactions in photon-proton scattering. Note that the spectra for the diffractive samples have been scaled down by 100.

It is interesting to compare the ZEUS non-diffractive spectrum to that from previous hadron-hadron and photoproduction experiments (Figure 7-5). The ZEUS spectrum is significantly harder than the $p\bar{p}$ spectrum at $\sqrt{s} = 200$ GeV, from the UA1 collaboration [58], which is the one closest to the ZEUS center of mass energy. The ZEUS spectrum is comparable to the UA1 $p\bar{p}$ spectrum at $\sqrt{s} = 900$ GeV. This indicates that there are more hard, partonic collisions in γp than in $p\bar{p}$ collisions. This is expected since the photon can interact directly with a parton from the proton. These direct interactions are an additional component to the hard scattering. There are no such direct interactions in the case of hadron-hadron scattering. Evidence for this effect was already ob-
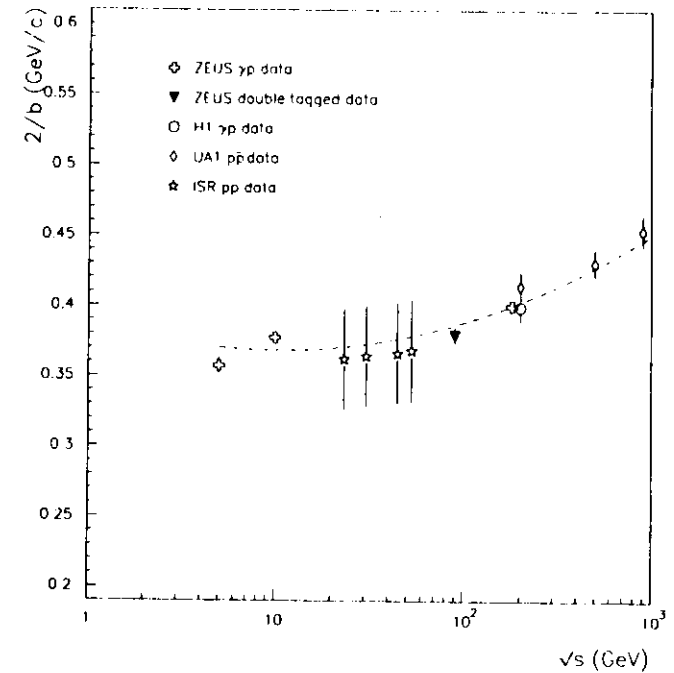

Figure 7-4 Exponential fit slopes to the p_T spectra in the low p_T region

The ZEUS results are shown, in comparison with other photoproduction and hadronic measurements. The curve drawn is to guide the eye. Only statistical errors are shown on the ZEUS points. (The non-ZEUS results are from: H1 [57], UA1 [58], and ISR [59]).

served by the much lower energy photoproduction experiments (e.g., WA69 experiment [11]) by comparing the photoproduction to the hadroproduction p_T spectra of charged particles with the same experimental setup. At HERA the direct process events were separated for the first time [13]. The data from the H1 experiment at HERA [57] agrees well with the ZEUS results.

The charged particle p_T spectrum for tagged γp events which are also tagged by high energy leading neutrons can also be studied. This double tagged sample consists of all the non-diffractive events with energy in the FNC greater than 400 GeV. In order to increase the sample size no scintillation counter cut was applied. Thus there is an implicit assumption that only high energy neutrons can deposit such high energy in the FNC. The result, compared with the non-diffractive result is shown in Figure 7-6. It exhibits the same overall characteristics as the other spectra already described above.

As discussed in the previous chapter, these events can be attributed to the One Pion Exchange process. Since t (see Section 2.3.1 for definition) is small, the pion is almost real and these
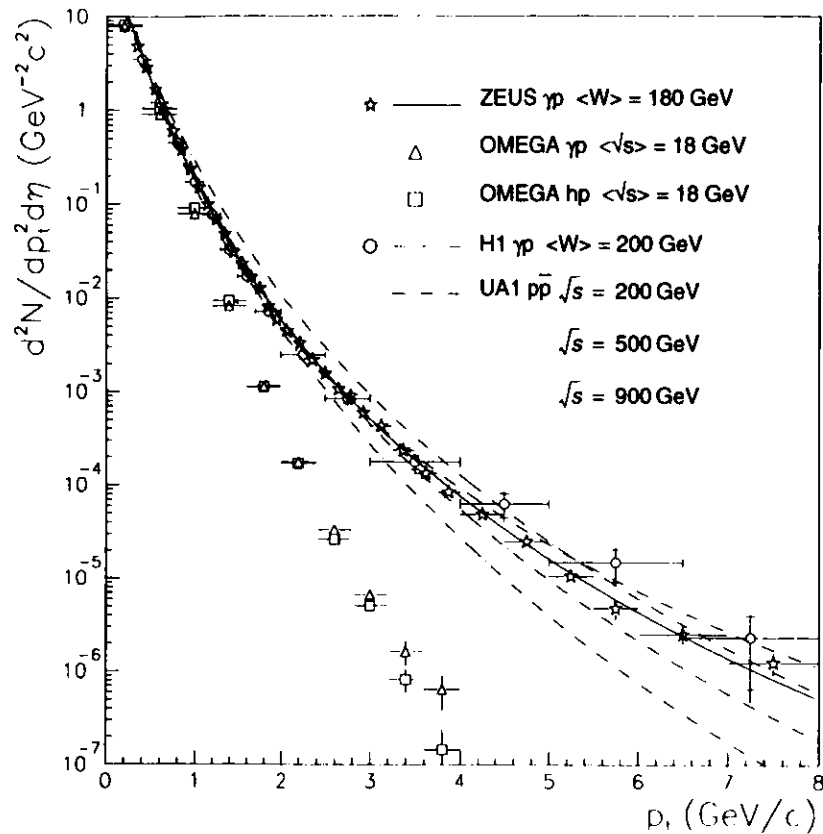
Figure 7-5 Comparison with other experiments

The ZEUS non-diffractive sample is compared to previous measurements. The ZEUS result is comparable to the UA1 result at $\sqrt{s} = 900$ GeV (The non-ZEUS results are from OMEGA [11], H1 [57], and UA1 [58]).

collisions can be treated as $\gamma\pi$ collisions with a varying center of mass energy with $<\sqrt{s}> = 90$ GeV (see Section 2.5.1). Thus it can be expected that the charged particle p_T spectrum is softer than the one for γp at $\sqrt{s} = 180$ GeV. The corresponding exponential slope fit parameter at low p_T is 0.379 ± 0.006 compared to 0.400 ± 0.001 for the ZEUS non-diffractive sample. The errors are statistical. In Figure 7-4 it can be seen that it is also consistent with the values from other experiments.

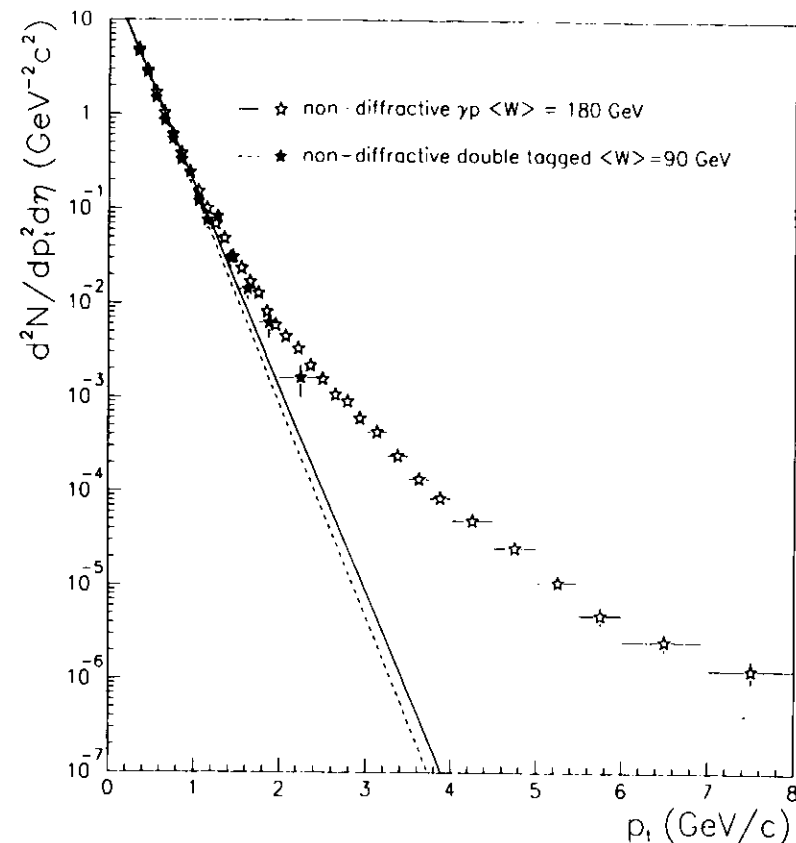**Figure 7-6 The p_T spectrum for the double tagged non-diffractive sample.**

Assuming OPE dominance the double tagged sample is interpreted as $\gamma\pi$ collisions at $<\sqrt{s}> = 90$ GeV. As expected, the spectrum appears to be somewhat softer than that for the tagged photoproduction sample, at twice the center of mass energy. A strong conclusion cannot be made due to the limited statistics.

"I would say what I have said."

Lohrmann

8   Conclusions

The test Forward Neutron Calorimeter has proven to be a great success. The simple device has not only shown that the observation and study of leading neutrons in ep collisions is possible at HERA, but has also had a rich physics yield which is presented in this thesis.

Already the calibration process itself contained physics results. The measurement of the inclusive neutron spectrum in beam-gas collisions is the smallest angle measurement of neutron production in the reaction pp → nX. Its consistency with the previous measurements at the ISR, as well as with the One Pion Exchange (OPE) model predictions has indicated good understanding of the detector and provided confidence for looking at the ep data.

The inclusive neutron spectrum in photoproduction for neutron energy greater than 400 GeV has been measured. The OPE model for hadron-hadron interactions describes the neutron spectrum well. This is expected if the photon behaves like a hadron in these high energy collisions, as is indicated by previous experiments. Assuming that the leading neutron production is dominated by OPE, detecting a leading neutron in the γp → nX reaction is equivalent to tagging an almost real pion, and hence measuring the γπ → X reaction. This has enabled the first measurement of the total photon-pion cross section. It was measured at $\sqrt{s} = 90$ GeV to be $\sigma_{\gamma\pi} = (92 \pm 5 \pm 28)$ μb.

Furthermore, by counting the ρ meson production with a leading neutron in photoproduction the diffractive contribution to the elastic ρ sample was estimated to be $(26 \pm 11 \pm 5)\%$. This provided a consistent cross-check for the measurement of the elastic ρ cross section, where this contribution has to be subtracted.

Finally, the inclusive p_T spectra of charged particles in tagged photoproduction have been measured. The data for the non-diffractive sample and for diffractive events in two bins of diffractive mass ($<M_x> = 5$ GeV and $<M_x> = 10$ GeV) are presented. Also the double tagged non-diffractive data (with both FNC and LUMIE tags) are also shown. All four samples show expected exponential dropoffs with p_T in the low p_T region, and the fits to the exponential slopes are consistent with previous measurements. The non-diffractive samples show an excess of events in the high p_T region, expected from the contribution from hard interactions. This tail is larger in the ZEUS data than in the corresponding hadron-hadron data at the same center of mass energy. The

double tagged sample is slightly softer than the photoproduction data, as expected if it is due to γπ interactions at half the center of mass energy.

The physics topics discussed in this thesis are a small sample of all the physics made available by a much better final detector that has replaced the test device, and is presently running at HERA. The new detector is a much larger device ($70\text{x}70\text{x}220$ cm^3), and its segmentation will also allow position measurement of the incoming particle. It also has a much better energy resolution ($65\% / \sqrt{E}$) and has been calibrated in the test beam at CERN. This detector upgrade, combined with the improvements in the HERA beams and luminosity should vastly increase the potential for studying the pion physics at HERA. Not only will the points that remain unclear in this thesis due to low statistics be resolved, but also new topics, such as measurement of the t distribution and pion structure function, will become available for study. Also, combined with the Leading Proton Spectrometer and the Proton Tagger (now also installed at ZEUS) the FNC should be of great help in diffractive studies, aiming at clarifying the nature of the Pomeron.

References

[1] F. Halzen and A. D. Martin, *Quarks & Leptons: An introductory Course in Modern Particle Physics*. John Wiley & Sons, Inc, Toronto (1984).

[2] R. P. Feynman, *Quantum Electrodynamics*. Benjamin, Inc, New York (1961).

[3] F. Wilczek, *Annu. Rev. Nucl. Sci.* **32** (1982) 177.

[4] D. H. Coward et al., *Phys.Rev.Lett.* **20** (1968) 292.

[5] G. Wolf, DESY 94-022 (1994).

[6] ZEUS Collab., M. Derrick et al., *Phys. Lett.* **B316** (1993) 412.

[7] ZEUS Collab., M. Derrick et al., *Phys. Lett.* **B345** (1995) 576.

[8] ZEUS Collab., M. Derrick et al., *Phys. Lett.* **B315** (1993) 481.

[9] ZEUS Collab., M. Derrick et al., Z. Phys. **C59** (1993) 231.

[10] G. A. Schuler and T.Sjöstrand, *Nucl. Phys.* **B407** (1993) 539.

[11] OMEGA Photon Collab., R. J. Apsimon et al., Z. *Phys.* **C43** (1989) 63.

[12] NA14 Collab., E. Auge et al., *Phys. Lett.* **B168** (1986) 163.
NA14 Collab., R. Barate et al., *Phys. Lett.* **B174** (1986) 458.

[13] ZEUS Colab., M. Derrick et al., *Phys. Lett.* **B322** (1994) 287.

[14] T. H. Bauer et al., *Rev. Mod. Phys.* **50** (1978) 261.
J. J. Sakurai, *Phys. Rev. Lett.* **22** (1969) 981.

[15] ZEUS Collab., M. Derrick et al., *Phys. Lett.*, **B297** (1992) 404.
See also references 5-8 in the above.

[16] H. Pilkuhn, *Interactions of Hadrons*. North-Holland Publishing Company, Amsterdam (1967).

[17] U. Amaldi, M. Jacob, and G. Matthiae, *Ann.Rev.Nucl.Sci.* **26** (1976) 385.

[18] M. L. Perl, *High Energy Hadron Physics*. John Wiley & Sons, Toronto (1974).

[19] R. Omnès and M. Froissart, *Mandelstam Theory and Regge Poles*. W.A. Benjamin, Inc., New York (1963).

[20] P. D. B. Collins, *An Introduction to Regge Theory and High Energy Physics*. Cambridge University Press, Cambridge (1977).

[21] R. Omnès, *Introduction to Particle Physics*. John Wiley & Sons, Toronto (1970).

[22] G. F. Chew and S. C. Frautschi, *Phys. Rev. Lett.* **7** (1961) 394.

[23] I. Ya. Pomeranchuk, *Sov. Phys. JETP.* **7** (1958) 499.

[24] G. Ingelman and P. Schlein, *Phys. Lett.* **B152** (1985) 256.

[25] A. H. Mueller, *Phys. Rev.* **D2** (1970) 2963.

[26] R. G. Roberts, "Phenomenology of Inclusive Reactions", in *Phenomenology of Particles at High Energies - Proceedings of the 14th Scottish Universities Summer School in Physics 1973*. Academic Press, London (1974).

[27] M. Bishari, *Phys. Lett.* **B38** (1972) 510.

[28] C. Göbel, *Phys. Rev. Lett.* **1** (1958) 337.

[29] F. Bonsignori and F. Selleri, *Nuovo Cim.* **15** (1960) 465.

[30] S. D. Drell, *Phys. Rev Lett.* **5** (1960) 278 and 342.
F. Salzman and G. Salzman, *Phys. Rev. Lett.* **5** (1960) 377.
F. Salzman and G. Salzman, *Phys Rev.* **120** (1960) 599.
S. D. Drell, *Rev. Mod. Phys.* **33** (1961) 458.
F. Salzman and G. Salzman, *Phys. Rev.* **121** (1961)1541.
G. E. Wolf, *Phys.Rev.* **182** (1969) 1538.

[31] G. Levman and K. Furutani, "Virtual Pion Scattering at HERA". ZEUS Note 92-107 (1992). Revised version DESY 95-142 (1995).

[32] J. Engler et al., *Nucl. Phys.* **B84** (1975) 70.

[33] H. Holtmann et al., *Phys. Lett.* **B338** (1994) 363.

[34] B. D. Burow, *A measurement of the Total Photon-Proton Cross Section in the Center of Mass Energy Range 167 to 194 GeV*, Ph. D. thesis, University of Toronto (1994).

[35] D. H. Perkins, *Introduction to High Energy Physics*. Addison-Wesley Publishing Company, Inc, Don Mills, Ontario (1987) Chapter 8 and references therein.

[36] The ZEUS Detector, Status Report 1993, ed. U. Holm (1993).

[37] C. Fabjan, "Calorimetery in High Energy Physics", CERN-EP/85-54, (1985)

[38] R. Wigmans, *Annu. Rev. Nucl. Sci.* **41** (1991) 133.

[39] J. Krüger, *The Uranium Scintillator Calorimeter for the ZEUS Detector at the Electron-Proton Collired HERA*, Habilitationsschrift, Universität Hamburg (1992), DESY F35-92-02.

[40] R. Wigmans, *Nucl. Instr. and Meth.* **A259** (1987) 389.

[41] R.W. Ellsworth et al, *Nucl. Instr. and Meth.* **A203** (1982) 167.

[42] L. Hervás, *The Pipelined Readout for the ZEUS Calorimeter*, Ph. D. thesis, Universidad Autónoma de Madrid (1990), DESY F35D-91-01.

[43] ZEUS Calorimeter Group, A. Anderseen et al., *Nucl. Instr. and Meth.* **A309** (1991) 101.
ZEUS Barrel Calorimeter Group, M. Derrick et al., *Nucl. Instr. and Meth.* **A309** (1991) 77.

[44] K. Piotrzkowski and M. Zachara, "Determination of the ZEUS Luminosity in '93". ZEUS Note 94-167 (1994).

[45] W. Smith, K. Tokushuku, and L. Wiggers, "First Level Trigger for 1993 Running". ZEUS Note 93-10 (1993).

[46] S. M. Fisher, P. Palazzi, *The ADAMO Data System Version 3.2*, (1992)

[47] U. Behrens et al., *Nucl. Instr. and Meth.* **A323** (1992) 611.

[48] S. Bhadra et al., *Nucl. Instr. and Meth.* **A354** (1992) 479.

[49] Review of Particle Properties, *Phys. Rev.* **D50** (1994) 1336-8.

[50] J. Engler et al., *Nucl. Instr. and Meth.* **106** (1973) 189.

[51] R. Brun et al., *GEANT3*, CERN DD/EE/84-1 (1987).

[52] J. Mainusch, *Measurement of the Total Photon-Proton Cross-Section at HERA Energies*, Ph. D. thesis in preparation, Universität Hamburg (1995).
C. Sampson, *Measurement of the Total Photon-Proton Cross Section at HERA*, Ph. D. thesis in preparation, University of Toronto (1996).

[53] T.E.O. Ericson, *Comm. Nuc. Part. Phys.* **13** (1984) 157.

[54] ZEUS Collab., M. Derrick et al., DESY-95-143 (1995).

[55] ZEUS Collab., M. Derrick et al., *Z. Phys.* **C63** (1994) 391.

[56] ZEUS Collab., M. Derrick et al., *Z. Phys.* **C67** (1995) 227.
M. Kasprzak, *Inclusive cross sections in photoproduction at HERA*, Ph. D. thesis in preparation, Warsaw University (1996).

[57] H1 Collab., I. Abt et al., *Phys. Lett.* **B328** (1994) 176.

[58] UA1 Collab., C. Albajar et al., *Nucl. Phys.* **B335** (1990) 261.

[59] A. M. Rossi et al., *Nucl. Phys.* **B84** (1975) 269.